

1-1-2006

Design and optimization of joints to mitigate shock in military vehicles under blast and impact loading

Umakanth Sakaray
University of Nevada, Las Vegas

Follow this and additional works at: <https://digitalscholarship.unlv.edu/rtds>

Repository Citation

Sakaray, Umakanth, "Design and optimization of joints to mitigate shock in military vehicles under blast and impact loading" (2006). *UNLV Retrospective Theses & Dissertations*. 2036.
<http://dx.doi.org/10.25669/t9jx-kzv1>

This Thesis is protected by copyright and/or related rights. It has been brought to you by Digital Scholarship@UNLV with permission from the rights-holder(s). You are free to use this Thesis in any way that is permitted by the copyright and related rights legislation that applies to your use. For other uses you need to obtain permission from the rights-holder(s) directly, unless additional rights are indicated by a Creative Commons license in the record and/or on the work itself.

This Thesis has been accepted for inclusion in UNLV Retrospective Theses & Dissertations by an authorized administrator of Digital Scholarship@UNLV. For more information, please contact digitalscholarship@unlv.edu.

DESIGN AND OPTIMIZATION OF JOINTS TO MITIGATE SHOCK IN MILITARY
VEHICLES UNDER BLAST AND IMPACT LOADING

by

Umakanth Sakaray

Bachelor of Science in Mechanical Engineering
Osmania University, India
June 2004

A thesis submitted in partial fulfillment
of the requirements for the

Master of Science Degree in Mechanical Engineering
Department of Mechanical Engineering
Howard R. Hughes College of Engineering

Graduate College
University of Nevada, Las Vegas
August 2006

UMI Number: 1439987

INFORMATION TO USERS

The quality of this reproduction is dependent upon the quality of the copy submitted. Broken or indistinct print, colored or poor quality illustrations and photographs, print bleed-through, substandard margins, and improper alignment can adversely affect reproduction.

In the unlikely event that the author did not send a complete manuscript and there are missing pages, these will be noted. Also, if unauthorized copyright material had to be removed, a note will indicate the deletion.

UMI[®]

UMI Microform 1439987

Copyright 2007 by ProQuest Information and Learning Company.

All rights reserved. This microform edition is protected against unauthorized copying under Title 17, United States Code.

ProQuest Information and Learning Company
300 North Zeeb Road
P.O. Box 1346
Ann Arbor, MI 48106-1346



Thesis Approval
The Graduate College
University of Nevada, Las Vegas

08 / 07, 2006

The Thesis prepared by

UMAKANTH SAKARAY

Entitled

**DESIGN AND OPTIMIZATION OF JOINTS TO MITIGATE SHOCK IN
MILITARY VEHICLES UNDER BLAST AND IMPACT LOADING**

is approved in partial fulfillment of the requirements for the degree of

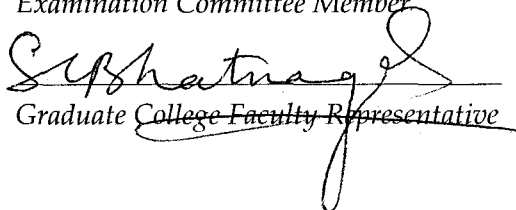
MASTER OF SCIENCE IN MECHANICAL ENGINEERING


Examination Committee Chair


Dean of the Graduate College


Examination Committee Member


Examination Committee Member


Graduate College Faculty Representative

ABSTRACT

Design and Optimization of Joints to Mitigate Shock in Military Vehicles under Blast and Impact Loading

by

Umakanth Sakaray

Dr. Mohamed B. Trabia, Examination Committee Chair
Professor and Chairperson of Mechanical Engineering
University of Nevada, Las Vegas

And

Dr. Brendan J. O'Toole, Examination Committee Chair
Associate Professor of Mechanical Engineering
University of Nevada, Las Vegas

Shock from a blast loading may risk the lives of the occupants of a military vehicle and damage the sensitive electronic components within it. The objective of this work is to develop an approach to mitigate shocks due to mine blast loading and impact loading by proper design of joint(s) in the military vehicles. Two types of vehicle configurations are studied for this purpose. The first vehicle is studied to examine ways to mitigate shock due to mine blast while the second vehicle is studied to mitigate shock due to projectile impact load. The proposed research includes design of joints in a way to disrupt/reflect/absorb the incident shock loading due to these transient events. The overall purpose of the study is to determine optimal types and configurations of joints that dissipate energy and incorporate the advantageous joint designs.

TABLE OF CONTENTS

ABSTRACT	iii
TABLE OF CONTENTS.....	iv
LIST OF FIGURES.....	vii
LIST OF TABLES.....	x
ACKNOWLEDGEMENTS.....	xi
CHAPTER 1 INTRODUCTION.....	1
1.1 Background.....	1
1.2 Blast and Shock Wave Theory	2
1.2.2.1 Normal Reflection	7
1.2.2.2 Regular Reflection.....	8
1.2.2.3 Mach Stem Formation	9
1.3 Modeling Blasts.....	12
1.4 Literature Review	15
1.5 Objective of the Research.....	23
CHAPTER 2 DESCRIPTION OF MODELS	25
2.1 General Aspects of Armored Vehicles	25
2.1.1 Suspension System	26
2.1.2 Turret	26
2.1.3 Main gun.....	26
2.1.4 Commander's station	27
2.2 Projectiles	27
2.2.1 Kinetic Energy Projectiles	27
2.2.1.1 Ball.....	27
2.2.1.2 Antipersonnel (APERS)	27
2.2.1.3 Armor piercing (AP).....	28
2.2.1.4 Armor piercing discarding sabot (APDS)	28
2.2.1.5 Armor piercing, fin-stabilized discarding sabot (APFSDS).....	28
2.3 Chemical energy	28
2.3.1 High explosive (HE).....	29
2.3.2 High explosive anti-tank (HEAT)	29
2.3.2.1 Impact	30
2.3.2.2 Ignition.....	30

2.3.2.3 Penetration	31
2.3.2.4 After-armor effects (spalling)	31
2.3.4 Flame Weapons	31
2.4 Armor Protection	32
2.4.1 Improved Armor technology	33
2.4.1.1 Reactive Armor	33
2.4.1.2 Laminated Armor	33
2.4.1.3 Composite Armor	34
2.4.1.4 Applique Armor	34
2.5 Latest Developments	34
2.6 The APC M113	35
2.6.1 APC M113 A1 Armored Personnel Carrier	36
2.6.2 APC M113A3 Armored Personnel Carrier	38
2.7 Model 1	43
2.7.1 Critical Locations on the Vehicle	47
2.8 Model 2	47
2.8.1 Details of Model 2	48
CHAPTER 3 DETAILS OF FINITE ELEMENT MODELS	56
3.1 Units	56
3.2 Model 1	56
3.2.1 Steps for Finite Element Analysis	56
3.2.2 Modeling	58
3.2.3 Meshing	59
3.2.4 Boundary conditions	60
3.2.4.1 Effect of ground surface	60
3.2.4.2 Effect of gravity	61
3.2.5 Loading conditions	62
3.2.6 LS-DYNA cards	64
3.2.6.1 Control Card	64
3.2.6.2 Database Card	65
3.2.6.3 Nodout Card	66
3.2.6.4 Material Card	66
3.2.6.5 Loading cards	68
3.2.7 Results	69
3.3 Model 2	80
3.3.1 Steps for Finite Element Analysis	80
3.3.3 Meshing	82
3.3.3.1 Modeling 3D Beam Elements	84
3.3.4 Defining 3D Beam Elements in LS-DYNA	86
3.3.4 Contact Definitions	88
3.3.5 Boundary Conditions	92
3.3.6 Loading Conditions	93
3.3.7 LS-DYNA cards	97
3.3.7.1 Control Card	97

3.3.7.2 Database Card.....	97
3.3.7.3 Nodout Card	97
3.3.7.4 Material Card.....	98
3.4 Results	98
3.4.1 Results for Load Case #1	98
3.4.2 Results for Load Case # 2.....	101
3.4.3 Effect of Joint Stiffness	105
3.4.3.1 Results and Discussion	105
CHAPTER 4 BOTTOM JOINT DESIGN AND OPTIMIZATION- MODEL 1	116
4.1 Joint Design for Shock Mitigation.....	116
4.2 Parametric Finite Element Analysis	114
4.2.1 Fixed Code.....	114
4.2.2 Variable Code.....	115
4.2.2.1 Modeling Procedure	116
4.2.2.2 Meshing	123
4.2.3 Parameters for LS-DYNA Analysis	130
4.2.3.1 Contact Surfaces	130
4.2.3.2 Blast Load Definition	133
4.2.3.4 LS-DYNA Input Cards.....	133
4.3 Joint Design Optimization.....	133
4.3.1 Design Variables.....	133
4.3.2 Objective Function	134
4.3.4 Optimization Technique	136
4.4 Results	139
CHAPTER 5 OPTIMIZATION- MODEL 2.....	111
5.1 Joint Design Characteristics	111
5.2 Parametric Finite Element Analysis	111
5.2.1 Fixed Code.....	115
5.2.2 Variable Code.....	117
5.2.3 Modeling Case 1	118
5.2.4 Modeling Case 2.....	119
5.2.4.1 Modeling and Meshing of part 1	120
5.2.4.2 Modeling part 2	129
5.5 Optimization Technique	130
5.5.1 SHQA Algorithm:.....	131
5.6 Results	133
5.6.1 Case 1	133
5.6.2 Case 2	137
5.6.3 Single Variable Optimization.....	138
CHAPTER 6 CONCLUSION	141
6.1 Results for Model 1	141
6.2 Results for Model 2	148
6.3 Conclusions	150

6.4 Scope for Future work	151
REFERENCES	154
VITA.....	159

LIST OF FIGURES

Figure 1: Simplified APC M113 Model.....	59
Figure 3.2 Meshed APC M113 Model	60
Figure 3.3 Rigid Wall Boundary Condition	61
Figure 3.4 ConWep Illustration.....	62
Figure 3.5 Load Location	64
Figure 3.6 Typical and Simplified (Bilinear Material Model)	67
Stress-Strain Curves	67
Figure 3.7 Acceleration Curves for Commander Location	71
Figure 3.8 Acceleration Curves for Driver Location.....	72
Figure 3.9 Acceleration Curves for Panel Location	73
Figure 3.10 Pressure Contours for Model 1 at 30 ms.....	76
Figure 3.11 von Mises Stress Contours for Model 1 at 30 ms	77
Figure 3.12 Displacement Contours for Model 1 at 30 ms	78
Figure 3.13 Plastic Strain Contours for Model 1.....	80
Figure 3.14: AX-1 Model	81
Figure 3.15: Frame of AX-1 Model	82
Figure 3.16: Meshed AX-1 Model	83
Figure 3.17: Mesh of the Space Frame in AX-1 Model.....	83
Figure 3.18: Defining the Beam Element.....	85
Figure 3.19: Example for Generating Beam Elements with Single Orientation Node	86
Figure 3.20: AX-1 Model from ARL	90
Figure 3.21: Zoom Window Details of FE Model in Figure 3.17.....	91
Figure 3.22: FE Model of AX-1	92
Figure 3.23: FE Model with Boundary Conditions	93
Figure 3.24: Load Case #1.....	94
Figure 3.25: Load Case #2.....	95
Figure 3.26: Load Curve for Load Case #1	96
Figure 3.27: Load Curve for Load Case #2.....	96
Figure 3.28: Displacement Contours for Load Case #1 at 25ms.....	99
Figure 3.29: Displacement Contours of Frame for Load Case #1 at 25ms	100
Figure 3.30: von Mises Stress Contours for Load Case #1 at 25ms.....	100
Figure 3.31: Plastic Strain Contours for Frame with Load Case #1 at 25ms	101
Figure 3.32: Displacement Contours for Load Case #2 at 25ms.....	102
Figure 3.33: Displacement Contours of Frame for Load Case #2 at 25ms	103
Figure 3.34: von Mises Stress Contours for Load Case#2 at 25ms.....	103
Figure 3.35: Plastic Strain Contours with Load Case#2 at 25ms	104
Figure 3.36: Plastic Strain Contours for Frame with Load Case#2 at 25ms	104
Figure 3.37: Displacement Contour for Case # 1 with Load Case # 2 at 25ms	108

Figure 3.38: Displacement Contours of Frame for Case # 1 with Load Case # 2 at 25ms	109
Figure 3.39: Displacement Contour for Case # 2 with Load Case # 2 at 25ms	109
Figure 3.40: Displacement Contours of Frame for Case # 2 with Load Case # 2 at 25ms	110
Figure 3.41: Displacement Contours of for Case # 1 with Load Case # 1 at 25ms	111
Figure 3.42: Displacement Contours of Frame for Case # 1 with Load Case # 1 at 25ms	112
Figure 3.43: Displacement Contours of for Case # 2 with Load Case # 1 at 25ms	113
Figure 3.44: Displacement Contours of Frame for Case # 2 with Load Case # 1 at 25ms	114
Figure 4.1 Vehicle Model with Joint (Bottom portion is made transparent to view joint)	111
Figure 4.2 Typical Joint Configuration (Bottom portion of the vehicle including joint)	112
Figure 4.3 Sectional View of the Vehicle Model with Joint	113
Figure 4.4 Model Geometry – Fixed Part	115
Figure 4.6 Joint Design Variables	116
Figure 4.7 Top View Showing the Joint Areas A2-A5 and Outline of the Vehicle Bottom Section	118
Figure 4.8 Joint Areas A6-A9 and Outline of the Vehicle Bottom Section	120
Figure 4.9 Complete Joint Model (Areas A2-A9)	121
Figure 4.10 Different Areas of the Bottom Plate	122
Figure 4.11 Side View of the Joint Areas A2-A5	124
Figure 4.12 Meshed Joint - Areas A2, A3, A4, and A5	127
Figure 4.13 Meshed Joint - Areas A6, A7, A8, and A9	127
Figure 4.14 Complete Meshed Joint – Areas A2–A9	128
Figure 4.15 Meshed Vertical Plate - Areas A10-A14	129
Figure 4.16 Meshed Complete Vehicle Joint Model	130
Figure 4.17 APC M113 Hull Model with Keypoints that Define it	136
Figure 4.18 Flow Chart Showing the Procedure of the Optimization Program	139
Figure 4.19 Acceleration Curves of Commander Location for Results of Case #1	142
Figure 4.20 Acceleration Curves of Driver Location for Results of Case #1	144
Figure 4.21 Acceleration Curves of Panel Location for Results of Case #1	145
Figure 4.20 Von Mises Stress Contour Plot – Case #1 at 30 ms	147
Figure 5.1: Nodal Locations for Parametric Study	112
Figure 5.2: Numbering Scheme for Joint Branches	114
Figure 5.2: Fixed Portion of the Code	116
Figure 5.3: Mesh of Fixed Portion of the Code	116
Figure 5.4: Variables for Case 1 Parametric Modeling	119
Figure 5.5: Details of Joint 3 before Modeling	125
Figure 5.6: Range of Variable y	126
Figure 5.7: New Coordinates of Joint Location 3	127
Figure 5.8: Case 2 Modeling Example for Left Movement of Joint	128
Figure 5.9: Mesh Details for the Joint Movement towards the Positive X-axis	128
Figure 5.10: SHQA for a Two-Dimensional Problem	133

Figure 5.11: Maximum Plastic Strain Contours for Optimized Case at 25ms (Side Impact)	136
Figure 5.12: Maximum Plastic Strain Contours for Optimized Case at 25ms (Front Impact)	136
Figure 6.1 Acceleration Curves for Commander Location (No Joint)	142
Figure 6.2 Acceleration Curves for Driver Location (No Joint)	143
Figure 6.3 Acceleration Curves for Panel Location (No Joint)	144
Figure 6.4 Acceleration Curves of Commander Location for Results of Case #1 (with Joint)	146
Figure 6.5 Acceleration Curves of Driver Location for Results of Case #1 (with Joint)	147
Figure 6.6 Acceleration Curves of Panel Location for Results of Case #1 (with Joint)	148

LIST OF TABLES

Table 3.1 Results for Model 1	70
Table 3.2 Stiffness Variation Details for Model 2	105
Table 4.1 Relations for Computing the Coordinates' of Points 5 through 12.....	119
Table 4.2 Relations for Computing the Coordinates' of Points 13-16.....	120
Table 4.3 Relations for Computing the Coordinates' of Points 17 through 24.....	123
Table 4.4 Contact Pair Definitions	132
Table 4.6 Final Results of Optimization Searches	140
Table 4.7 Accelerations for the Results of Case #1.....	141
Table 4.8 Accelerations for the Results of Case #2.....	141
Table 4.9 Accelerations for the Results of Case #3.....	142
Table 5.1 Coordinates for Locations Associated with Joint 3.....	120
Table 5.2 Side Impact Results	134
Table 5.3 Front Impact Results	134
Table 5.4 Side Impact Results for Case 2.....	137
Table 5.5 Results for Movement of Joint at 3	139
Table 6.1: Acceleration results for the no-joint vehicle	145
Table 6.2: Initial guess and Final Design Parameters	145
Table 6.3: Optimized acceleration results for Final Design.....	145
Table 6.4 Side Impact Results	149
Table 6.5 Front Impact Results	150

ACKNOWLEDGEMENTS

I express my sincere gratitude to my thesis advisors Dr. Mohamed B Trabia and Dr. Brendan J O'Toole, for their continuous guidance, support and encouragement throughout this research activity.

I would like to thank Dr. Satish Bhatnagar, Dr. Ajit K Roy, and Dr. William Wells for their time in reviewing the prospectus, participation of defense as the committee members.

I would like to acknowledge the financial support rendered by the Army Research laboratory (ARL), under project BS4.

Finally, I would like to thank my parents, friends and colleagues without there continuous support and faith this work would not have been possible.

CHAPTER 1

INTRODUCTION

1.1 Background

In the modern world, light combat vehicles and armored vehicles are playing a key role in supporting the troops and other heavily armored combat vehicles. As such, during the real combat situations they are subjected to extreme loading scenarios. Fierce battlefield environments make these vehicles susceptible to damage and the survivability of the occupants becomes questionable. Appropriate design of these vehicle structures against severe on field conditions is vital to ensure occupant survivability and vehicular operational needs [1].

Several types of armored vehicles are used in modern wars. While heavily armored vehicles play a major role, medium and light vehicles usually help in consolidating positions. While all types of combat vehicles need to be designed keeping in view of their severe environments, light combat vehicles are at greater risks when subjected to shock loads. These shock loads primarily occur due to impacts from projectiles or blasts. An area of critical concern is the propagation of shocks within combat vehicles to the location of the driver and the other personnel in the crew compartment as well as attachment points for optical and electronic devices [2]. Failure of equipments due to shock and vibration may render the whole system ineffective

leading to life threatening situations. Detailed study of shock propagation can help reduce these effects by appropriate design of all the structural sub-assemblies.

1.2 Blast and Shock Wave Theory

1.2.1 Blast Waves

A shock wave resulting from an explosive detonation in free air is termed an air-blast shock wave, or simply a blast wave. The blast environment will differ depending on where the explosion takes place. In the case of an airburst, when blast wave hits the ground surface, it will be reflected. The reflected wave will coalesce the incident wave and a mach front is created as shown in the Figure 1.1. The point where the three shock fronts meet – incident wave, reflected wave and the mach front – is termed the triple point [3].

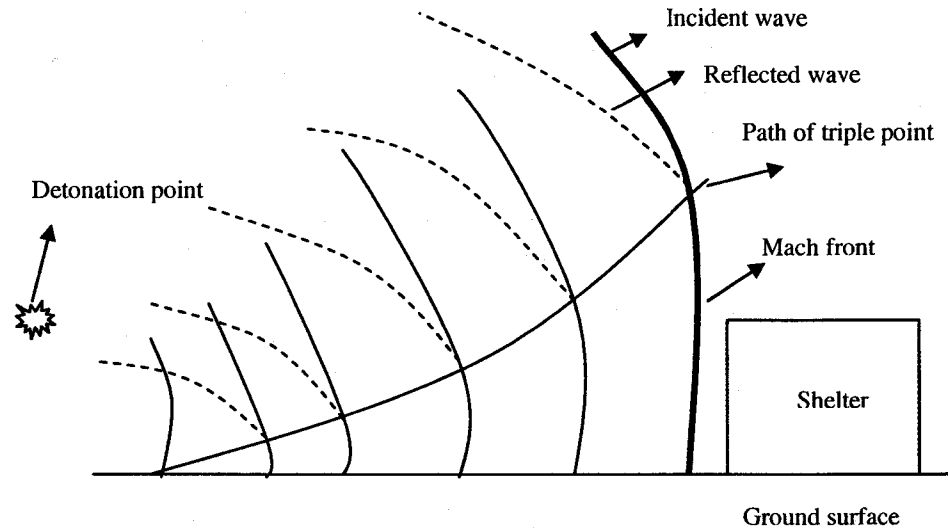


Figure1.1: Blast Environment From an Airburst

In the case of a surface burst, the reflection happens instantaneously against the ground surface and a shock wave is created; this is termed a global reflected wave, as shown in Figure 1.2. At a short distance from the burst, the wave front can be approximated by a plane wave.

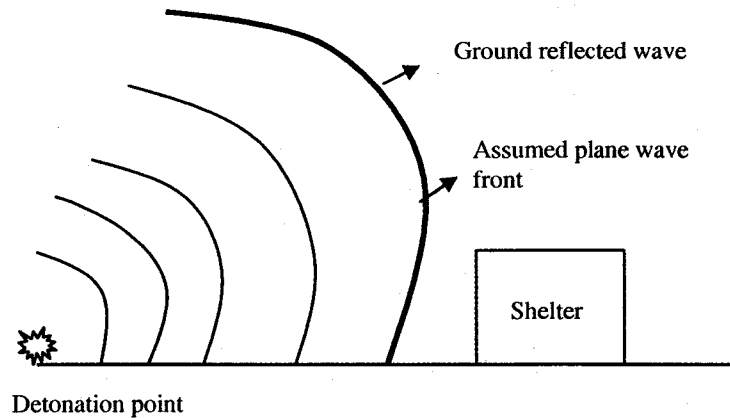


Figure 1.2: Surface Burst Blast Environment

The pressure-time history of a blast wave can be illustrated with a general shape as shown in Figure 1.3. The illustration is an idealization for an explosion in free air. The pressure-time history is divided into positive and negative phases. In the positive phase, maximum overpressure, P_s^+ , rises instantaneously and decays to atmospheric pressure, p_o , in time T^+ . The positive impulse, i^+ , is the area under the positive phase of the pressure-time curve. For the negative phase, the maximum negative pressure, P_s^- , has much lower amplitude than the maximum over pressure. The duration of the negative phase, T^- , is much longer compared to the positive duration. The negative impulse, i^- , is the area under the negative phase of the pressure-time curve.

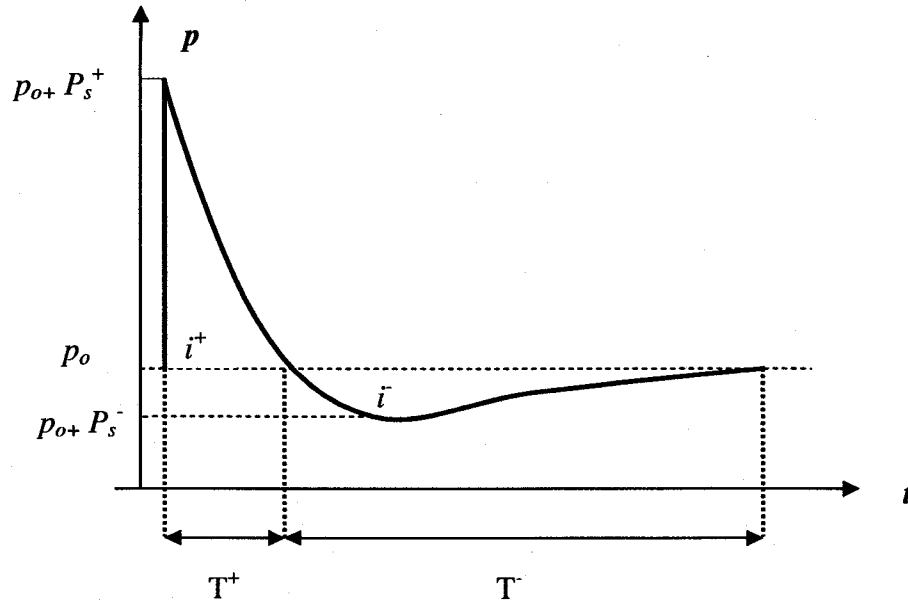


Figure 1.3: Pressure - Time History From a Blast

The pressure-time history in Figure 1.3 can be approximated by the following exponential form [3].

$$p(t) = p_0 + P_s^+ \left(1 - \frac{t}{T^+}\right) e^{-bt/T^+} \quad (1.1)$$

where $p(t)$ is the overpressure at time t , and T^+ (the positive duration) is the time for the pressure to return to atmospheric pressure, p_0 . By selecting a value for the constant b , various pressure-time histories can be described. The peak pressure, P_s^+ , is dependent on the distance from the charge and the weight of the explosives. In addition, if the peak pressure, the positive impulse and the positive time duration are known, the constant b can be calculated, and then the pressure-time history is known. Equation (1.1) is often simplified with a triangular pressure-time curve;

$$p(t) = p_0 + P_s^+ \left(1 - \frac{t}{T^+}\right) \quad (1.2)$$

Conventional high explosives tend to produce different magnitudes of peak pressure. As a result, the environments produced by these chemicals will be different from each other. In order to establish a basis for comparison, various explosives are compared to equivalent TNT values [4]. With the help of a scaling parameter Z , it is possible to calculate the effect of a detonated explosion, conventional or nuclear, as long as the equivalent weight of charge in TNT is known. The scaling parameter is represented as in equation (1.3).

$$Z = \frac{R}{W^{1/3}} \quad (1.3)$$

where R is the distance from the detonation and W is the equivalent weight of TNT.

The peak pressure, the positive duration time and the positive impulse are now functions of Z , and the pressure-time history in Figure 1.3 can be described as

$$P_s^+(Z), \frac{T^+}{\sqrt[3]{W}}(Z), \frac{i^+}{\sqrt[3]{W}}(Z) \quad (1.4)$$

1.2.2 Blast Wave Reflections

When a blast wave strikes a surface, which is not parallel to its direction of propagation, a reflection of the blast wave takes place. The reflection can be either normal reflection or an oblique reflection. There are two types of oblique reflection, either regular or Mach reflection; the type of reflection depends on the incident angle and shock strength.

1.2.2.1 Normal Reflection

A normal reflection takes place when the blast wave hits perpendicular to a surface, as shown in Figure 1.4. The medium has a particle velocity, U_x , before the incident shock wave, U_s , passes the medium; after passage the particle velocity increases

to U_p . Furthermore, the overpressure increases from p_x to p_y (p_x , refers usually to atmospheric overpressure), the temperature increase from T_x to T_y and the sonic speed increases from a_x to a_y (a_x is approximately 340 m/s in undisturbed air).

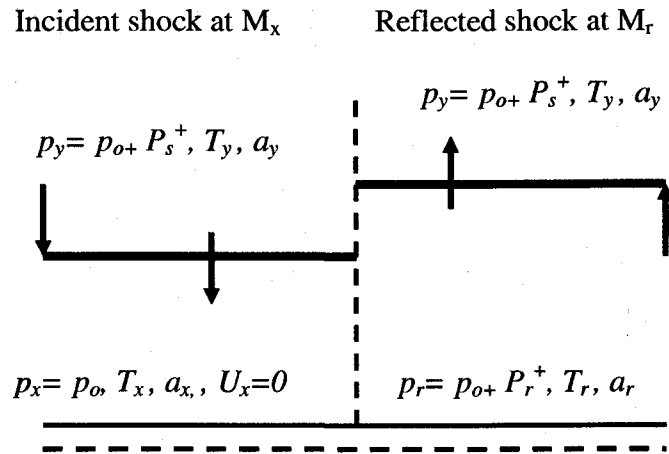


Figure 1.4: Normal Reflection From a Rigid Wall

When the blast wave hits a rigid surface, the direction will be shifted rapidly, and, as a consequence, the particles at the surface possess a velocity relative to those further from the surface that are still in motion. This relative velocity is equal in magnitude and opposite in direction to the original practical velocity and gives the effect of a new shock front moving back through the air; the reflected shock, U_r . However, since the air conditions have changed, the reflected shock will have different properties. The reflected overpressure increases to p_r , temperature increases to T_r and sonic speed will be a_r .

It is common to describe the velocity of shock waves in terms of Mach number, which is defined as the actual velocity (of the shock front) in the medium divided by the sonic speed of the undisturbed medium. For example, the shock front will have a velocity with a Mach number M_r into air that had a velocity with M_x at the incident shock.

The properties of the reflected blast wave can be described in terms of a reflection coefficient, defined as the ratio of reflected overpressure to the overpressure in the incident blast wave. It can be shown that for an ideal gas with a specific gas constant ratio 1.4, the reflection coefficient Λ is, according to Baker [5]

$$\Lambda = \frac{p_r - p_x}{p_y - p_x} = \frac{8M_x^2 + 4}{M_x^2 + 5}. \quad (1.5)$$

Equation 1.5 it can be seen that for a shock front moving with M_x equal to one, i.e. at sonic speed, the reflection coefficient will be two. This means that the overpressure is twice in the reflected blast wave. With increasing speed for the shock front, M_x , the reflection coefficient approaches eight. In a real blast wave, the specific gas constant ratio is not constant, and the coefficient is pressure-dependent; the reflection coefficient increases with increasing pressure.

1.2.2.2 Regular Reflection

In a regular reflection the blast wave has an incident shock at M_x with an angle of β . The reflected shock at M_r has an angle of δ as shown in Figure 1.5. The angle of reflection is not generally equal to the angle of incidence. The air conditions in front of the incident shock (region 1) are still at pressure p_x and temperature T_x . Behind the incident shock (region 2), the air conditions are the same as for free air shock, with pressure p_y and temperature T_y . The air conditions from the reflected shock (region 3), have the pressure p_r and temperature T_r .

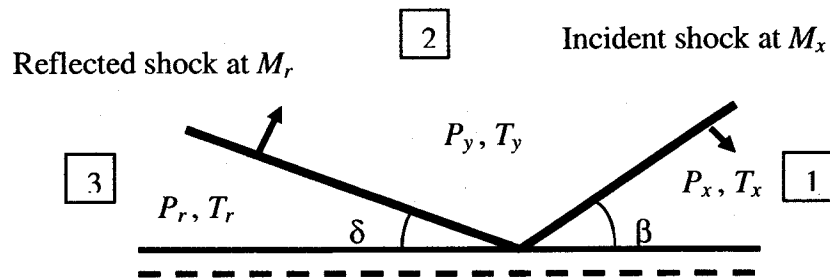


Figure 1.5: Oblique Reflection

1.2.2.3 Mach Stem Formation

There is a critical angle that depends on the shock strength, where an oblique reflection cannot occur. According to Baker (1973) [5], Ernst Mach [Mach and Sommer (1877)] showed that the incident shock and the reflected shock coalesce to form a third shock front. The created shock front is termed the Mach stem or Mach front, which is moving approximately parallel to the ground surface, as shown in Figure 1.6, with increasing height of the shock front. The point where the three shock fronts meet is termed the triple point. The Mach front and the path of the triple point are also shown in Figure 1.1.

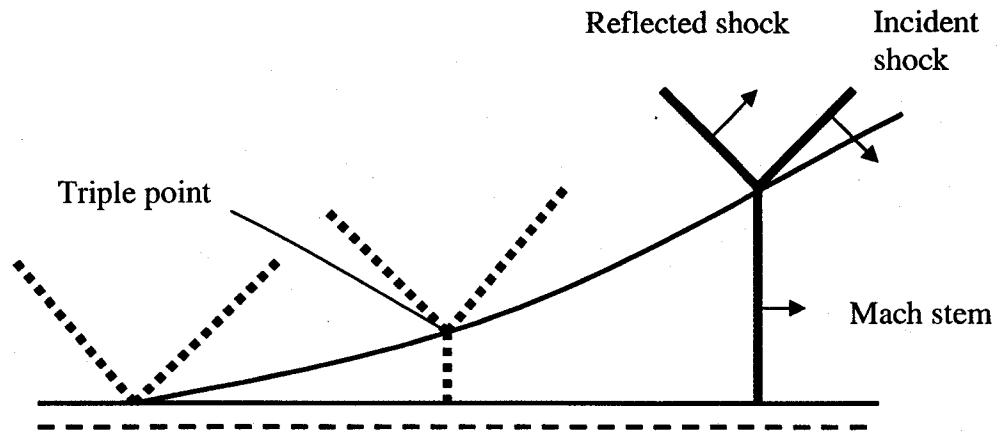


Figure 1.6: Mach Stem Formation

1.2.3 Shock Waves

The fundamental shock wave equations, known as the Rankine-Hugoniot equations, are derived from the equations for conservation of mass, momentum, and energy in the medium by choosing a fixed reference in space (the shock front), where the material motions are derived with respect to that region. Consider the one-dimensional model in Figure 1.7, where the material is moving with a velocity of U_0 against the shock front, and the material velocity is U_1 after passing the shock front. The pressure is P_0 and the density ρ_0 before the material reaches the shock front, and the pressure is P_1 and the density ρ_1 after the passage [3].

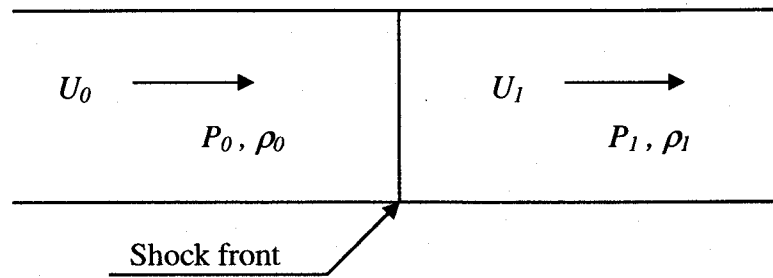


Figure 1.7: Model for One-Dimensional Shock Wave

Consider the conservation of mass flow per unit time and area in the model in Figure 1.7. It can be expressed for times t_0 and t_1 as

$$m = \rho_0 U_0 A \Delta t = \rho_1 U_1 A \Delta t \Leftrightarrow \rho_0 U_0 = \rho_1 U_1. \quad (1.6)$$

Considering the conservation of momentum, mass times the change in velocity is equal to the impulse of external forces. By using equation 1.6 the conservation of momentum can be derived as

$$m(U_0 - U_1) = P_1 - P_0, \quad (1.7)$$

where m is the flow of mass per unit area. The change in internal energy and kinetic energy is equal to the work done by external forces. It can be shown, as in Baker [5] that the conservation of energy per unit mass can be expressed as

$$E_1 - E_0 = (P_1 + P_0) \left(\frac{1}{\rho_0} - \frac{1}{\rho_1} \right). \quad (1.8)$$

Equations (1.6), (1.7) and (1.8) are the Rankine-Hugoniot equations. The Hugoniot curve expresses the relationship for and specific volume as shown in Figure 1.8. However, the material state is described by a discontinuous jump from one state to another, known as the Rayleigh line.

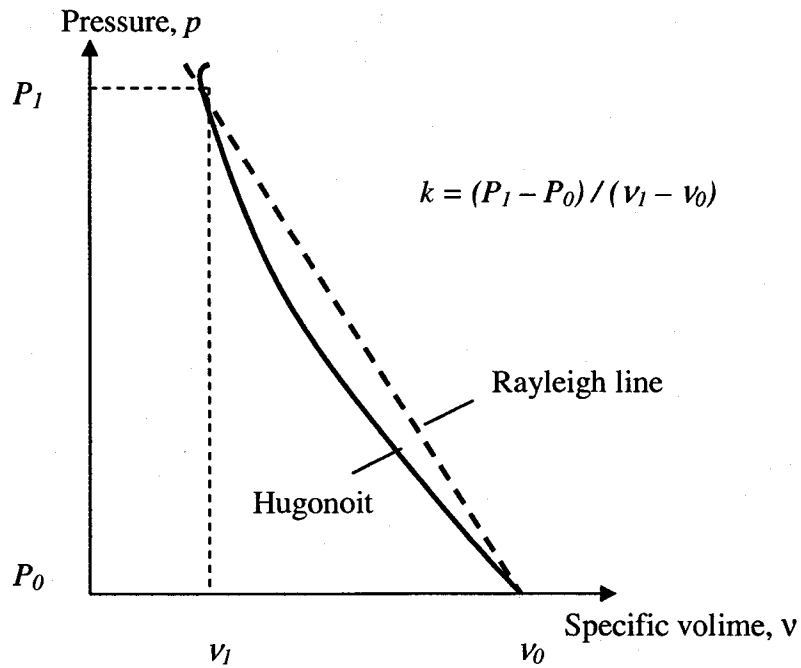


Figure 1.8: Hugoniot Curve and Rayleigh Line, k is the Slope of the Rayleigh Line

1.3 Modeling Blasts

In this section, the discussion will concentrate on two blast loading techniques available in the explicit finite element code, LS-DYNA.

1.3.1 ConWep

ConWep stands for Conventional Weapons. ConWep is a blast function which can be used to simulate blast load without having to explicitly model the high explosive. The blast function in LS-DYNA can be implemented for two cases, one for the free air detonation of a spherical charge and the other for surface detonation of a hemispherical charge. The surface detonation condition can be applied to simulate mine blasts as it can account for effects up to 5-20 cm below the surface of the ground. However ConWep does not account for other factors like depth of burial and soil properties, which can have significant impact on the final energy imparted on the target. ConWep air blast function

has inputs of TNT equivalent mass, type of blast (surface or air), location in space of detonation, and surface identification of which the pressure will be applied. From this information, ConWep calculates the appropriate pressure to be applied to the designated surface. ConWep function accounts for the angle of incidence of the blast wave, but does not account for the shadowing, confinement and secondary pressure wave effects. However, Randers and Pehrson [6] implemented empirical blast models by using the ConWep function inherent in the explicit finite element simulation tool DYNA3D. They tested the computational models against experiments to good agreement, and concluded that the ConWep function is adequate for use in mine blast applications.

1.3.2 Arbitrary Lagrangian Eulerian (ALE)

Blast phenomenon involves interaction of fluid with a structure and an effective method of modeling the fluid-structure interaction system is the Arbitrary Lagrangian-Eulerian (ALE) approach. ALE is very helpful when analyzing structural motions of severely deformed objects, such as in high explosive impact problem. The Arbitrary Lagrangian-Eulerian (ALE) approach combines the use of the Lagrangian and Eulerian reference frames. A Lagrangian reference frame acts by fixing a grid to the material of interest then as the material deforms the grid deforms with it. The Eulerian Reference Frame, which is fixed in space, allows for material to flow through the grid. However, it does not track the path of any individual particle. An ALE approach allows for both a flexible grid and a grid that allows for material to flow through it. In essence, it takes the best part of both reference frames and combines them in to one. It allows for the grid to track the material to some extent, but when the grid deforms excessively and distorts the

aspect ratio of the grid beyond an acceptable point it adjusts the grid and measures the flux of the material during the adjustment of the grid [7].

ALE technique application in blast modeling involves modeling the high explosive charge and surrounding fluid in an Eulerian mesh, which is then coupled with a Lagrangian mesh (the target). The ALE method models the explosion and resulting pressure profile throughout the Eulerian mesh. The fluid-structure interaction is based on penalty-contact methodology: the Eulerian elements are coupled with quadrature points on the face of the Lagrangian elements. Mahmadi et al. [7] used two levels of ALE technology (Eulerian Multi-Material and ALE formulations) to demonstrate the air blast phenomenon. A comparison between the numerical and experimental pressure histories of the blast showed good correlation. Also, this method has already been successfully implemented in many applications like sloshing tank problem, land mine simulation [8] and air bag simulation [9]. However, ALE modeling of blasts is computationally expensive than ConWep.

1.4 Literature Review

The following discussion will concentrate on work done by various researches on several sub structures of a light armored vehicle.

1.4.1 Armored Vehicle Hull

Extensive research is done by U.S. Army Research Laboratory to analyze the dynamic response of combat vehicles. Tank-automotive and Armaments Research, Development and Engineering Center (TARDEC), US Army has been effectively using Modeling and Simulation (M & S) to evaluate new designs prior to selection and testing,

support operational and development testing, evaluate field mishaps and/or accident situations, product improvement programs and alternative payloads [10].

Gupta et al [2] studied the dynamic response of the U.S. Army Armored Personnel Carrier, APC M113. A continuous hull structure model is used to represent the actual vehicle (Figure 1.9). A detailed analysis was carried out using finite element approach (using ADINA code) to evaluate the post-impact response at specific locations in the model. A shock response analysis was applied to the acceleration histories of the critical locations to obtain shock spectra at these locations.

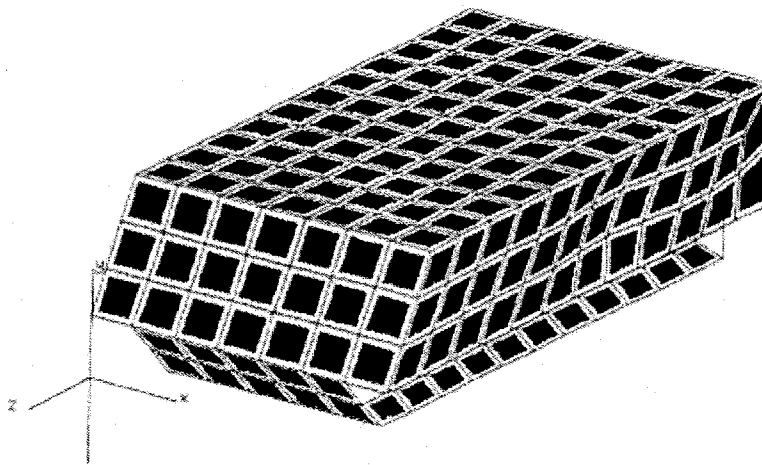


Figure 1.9: Simple Model of M113 Vehicle [2]

The spectra indicated that the simplified model contained no structural frequencies below 5 KHz, but the impact point exhibited a uniformly spaced sequence of harmonics continuing beyond the cut-off frequency of 5 KHz and having periods equal to multiples of the load duration. Their study also indicated that no structural frequencies higher than 440 Hz can be detected at all the locations except the impact point where the same sequence of harmonics were noticed.

It was realized that a continuous model may not be able to accurately determine the dynamic response of the vehicle as it did not incorporate all the essential features of the vehicle. Therefore, the driver and cargo hatch openings, as well as engine access and rear door cutouts were included in a basic hull model of M113 to allow comparison with experiments [1]. The FE model with of the basic M113 metallic hull with multiple access openings is shown in the Figure 1.10.

Some differences were observed between computed and experimental frequencies. The computed mode shapes at the low frequency range exhibited very little response which is attributed to the floor while the roof underwent considerable outward bending deformation. The lowest three flexible modes from the modal experimental analysis primarily showed the deflection of the roof with a large deflection centered over commander's cupola and the cargo hatch. A fundamental frequency of 33.27 Hz was computed from the model but was not detected in the experiments. The difference between the computations and the experiment was mainly attributed to the position of the exciters in the experimental model.

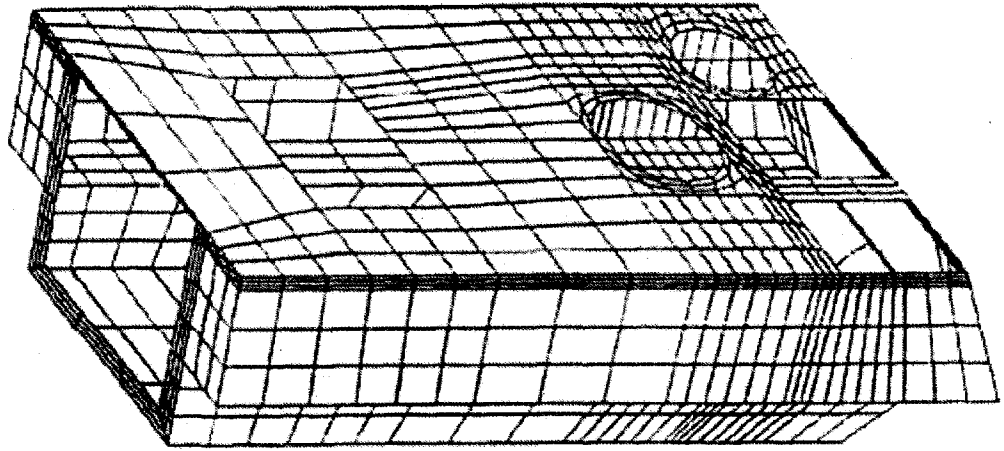


Figure 1.10: Finite Element Model of Basic M113 with Multiple Access Openings [1]

In order to get a better picture of the overall dynamic response, three major sub-assembly models of an armored vehicle i.e. the hull, the turret and the gun were assembled together using PATRAN3 code to generate the full-up vehicle model [11]. The model is shown in the Figure 1.11.

The assembled FE model was used to simulate free vibrational response for the lowest 30 eigenfrequencies to facilitate comparison with experiments. A comparison of the eigenfrequencies and the mode shapes from the FE model with those from the experimental modal analysis results indicated poor agreement. It was noticed that several component masses attached to the experimental hull were not accounted for in the computational model. In order to account for these masses, an implicit modeling approach with respect to missing components was adopted using concentrated masses attached to corresponding nodes and uniformly distributed in the associated area in which these components are actually attached to the hull-turret assembly. After these changes,

the computational and experimental modal analysis results were in good agreement with each other.

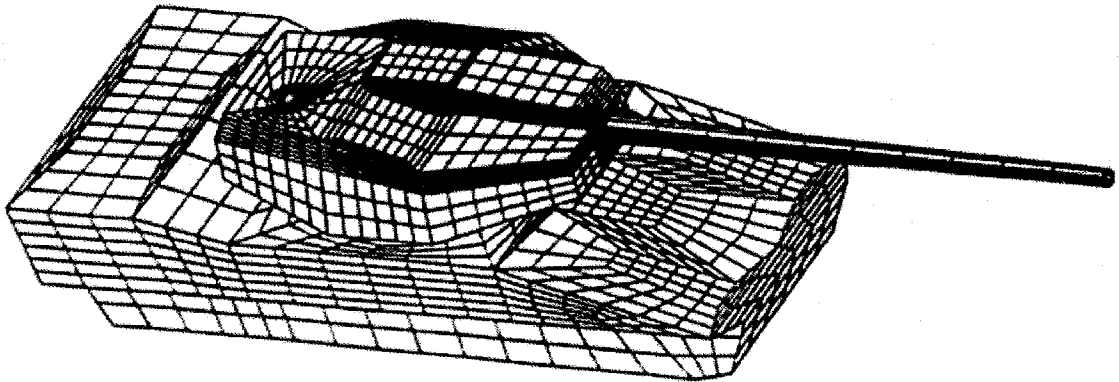


Figure 1.11: Finite Element Model of Hull-Turret-Gun assembly [11]

Unruh et al. [12] instituted a program of shock measurements in a scaled simulated armored vehicle to support an effort of shock protection of secondary components in combat vehicles. The scaled model was subjected to airblast, land mine blast and kinetic energy projectile impact. However, few researchers studied effects of mine blasts on military vehicles. For example, both Norman [13] and Hoskins et al. [14] employed an approximate energy method to study the vulnerability of tank bottom hull floor panels subjected to shallow-buried mine blast. Gupta [15] investigated the modeling and analysis of a blast defector for a tactical vehicle due to detonation of a mine buried in dry vs. saturated sand. Laine et al. [16] performed numerical simulations with a multi-material Euler processor to determine incident impulses and pressure histories from detonations of fully buried, flushed and surface anti-tank mines for dry porous sand and saturated clay. Lafrance [17] conducted a series of tests, in which anti-tank blast mines

were detonated underneath military support vehicles to develop an optimal protection system for the crew of such vehicles.

1.4.2 Space Frame Structures

Space frame structures are extensively used in the automobile industry in building vehicles. They increase the fuel efficiency by decreasing weight. They also add stiffness to the entire structure. However, from structural point of view, monolithic space frame structures are not considered as realistic solution for complex structures such as automotive bodies. This is mainly due to cost-effectiveness of manufacturing processes involved in building these structures. As a result, most space frames structures are designed as assemblies of components with simpler geometries. In contrast to commercial vehicles, space frame structures in armored vehicles may be subjected to severe deformations. Joints in space frames play a very important role in maintaining the structural integrity of a combat vehicle during such transient events. Non-linear shock transfer performance of joints has substantial influence on the dynamics of assembled structures as they induce a large amount of damping into the structure [18]. Study of shock transmission through the various jointed (both mechanical and adhesive) components of the combat vehicle is of particular interest to the Army. There is a need to guarantee the survivability and minimize the damage caused to both the primary and secondary electronic systems present inside the combat vehicle. Another area of concern is to reduce or damp the shock transmission caused by a projectile impact. Hence it is important to study the dynamic behavior of space frame structures under extreme loads before they are used in light armored vehicles to ensure the safety of critical equipments and the crew.

The introduction of low-priced computers revolutionized the method of structural analysis. Though once considered as impractical and too complicated as an analysis technique, the matrix method of structural analysis is easily programmed and commonly used. This also facilitated in development of several models by researchers to study the dynamic analysis of space frames. Masuda et al [19] presented a dynamic response analysis method which can deal with frames with finite rotations in the three-dimensional space. The method mainly concentrated on studying the dynamic instability (a state at which small increment in loading produces sudden changes in maximum response) in the presence of strong geometric non-linearity and three-dimensional behavior. Karpurapu et al [20] proposed a kinematic model for linear or non-linear analysis that is specially suitable for the three-dimensional framed structures of general shape. The transformation matrices proposed in the model was purely based on geometric properties which made the model to be used in both linear and non-linear analysis of space frames. Goman Wai et al [21] suggested a displacement based finite element technique which can handle genuinely large deflections with rotations more than 15° . An incremental secant stiffness approach was used which considered the effects of joint flexibility for the nonlinear analysis of two and three dimensional frames. The model was advantageous in handling large deflections accurately in three dimensional space and fast rate of convergence. Chan [22] also presented a simple, efficient and practical procedure for dynamic and static large deflection analysis of space frames. The special feature of the method was its ease of implementation in computer program and fast rate of convergence for equilibrium. Research has also been done on developing tools that help in optimizing geometric parameters of space frames by imposing stress and free frequency constraints

[25]. In addition to these computational models, several commercial finite element codes are capable of performing dynamic analysis of complex structures. However there is a need to verify the effectiveness of these different models in case of space frame structures used in armored vehicles because of the extreme nature of the loading involved.

Space frame structures are built with a number of beams joined together by suitable method. The beam members in armored vehicles may undergo severe deformation in the presence of high transient events like projectile impacts and blasts. To ensure the safety of the crew inside armored vehicles, the whole structure should collapse within the crushable zone to absorb the impact energy. This can be easily achieved by reducing the structural stiffness of the structure by the addition of imperfections like dents and bents [24]. However, high stiffness in a structure is required to protect the sensitive electronic equipment by reducing the vibrations and noise. Hence the design of the beams in the space frame structures of armored vehicles should concentrate on increasing the energy absorption not compromising on the stiffness. Sandwich beams comprising stiff and strong face sheets and low density cores seem to be possible solution for light armored vehicles as they provide superior quasi-static bending strength. The resistance of sandwich beams to dynamic loads remains to be fully investigated in order to quantify the advantages of sandwich construction over monolithic designs for application in shock resistant structures [26].

1.5 Objective of the Research

The present work is part of a collaborative effort between the Army Research Labs (ARL) and University of Nevada, Las Vegas. Light combat vehicles play a key role

in supporting heavy armored vehicles in actual battle field. As such they are subjected extreme loads in the form of projectile impacts or blasts. To be effective on the battlefield, they must be capable of sustaining operation in the face of mechanical shocks due to blast loads. Shock from a blast loading may risk the lives of the occupants of a military vehicle and damage the sensitive electronic components within it. The objective of this work is to develop an approach to mitigate shock in military vehicles. The targeted representative models for actual armored vehicles chosen for this purpose are: a recently developed space frame structure and a vehicle hull structure representing the APC M113 A2 vehicle. A non-monolithic space frame structure is developed by ARL as part of its program for the development of efficient light armored vehicles. The space frame structure is chosen to analyze the shock transmission due to a fragment/ impact load, while the vehicle hull structure is used to study shock transmission due to a mine blast. The following procedure is adopted to minimize shock in these vehicles.

1. Identify critical locations in the models that can be benchmarked as positions for attenuating shock.
2. Use finite element techniques to model and analyze the vehicles.
3. Design proper joints in the vehicle structure to disrupt/deviate/absorb such shock loads.
4. Optimize geometric parameters of the proposed joint for the vehicle hull model and for the existing joints in the vehicle space frame model to minimize shock transmission across the critical locations.

CHAPTER 2

DESCRIPTION OF MODELS

2.1 General Aspects of Armored Vehicles

There has been a considerable improvement in the performance of armored vehicles due to the addition of several structural features. In this section an overview of important sub segments of an armored vehicle is provided. Additionally, an effort is made to explore different types of projectiles that an armored vehicle can be exposed to.

Four structural areas may be used to identify vehicles: suspension system, turret, main gun, and commander's station. Most armored vehicles have these four areas though not all vehicles do. Reactive armor, camouflage, and increased use of sandbags can greatly alter the shape of vehicles. Figure 2.1 shows details of a general armored vehicle [34].

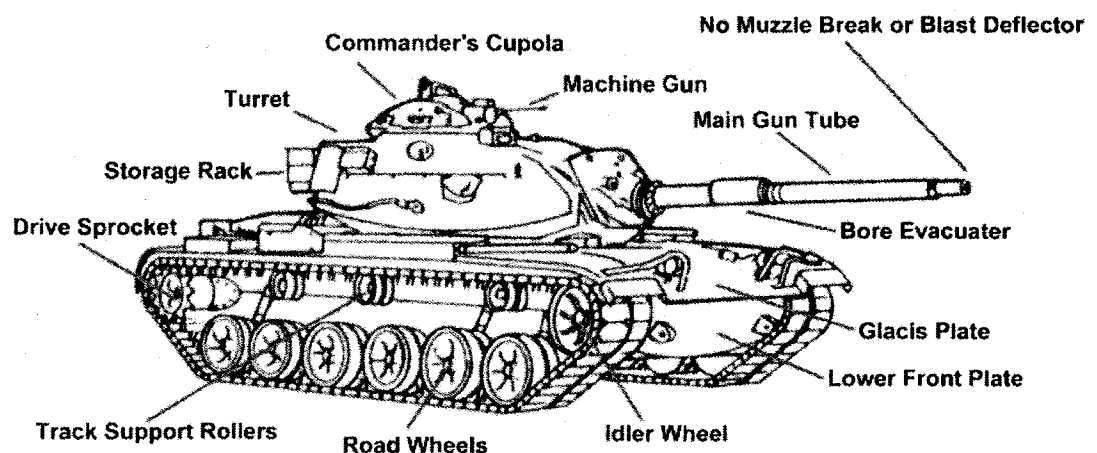


Figure 2.1: Details of a General a Armored Vehicle [34]

2.1.1 Suspension System

This is the least reliable area for identification as it is often concealed by vegetation or by terrain. Characteristics of the suspension system of combat vehicles are:

- Tracked vehicle.
- Number of road wheels.
- Spacing between road wheels.
- Number of support rollers.
- Armored skirt.

2.1.2 Turret

A turret can be characterized using the following:

- Position on the hull: well forward, center, or to the rear.
- Shape of turret: rounded, elongated, or boxy.
- Presence, absence, or location of searchlight.
- Externally mounted storage racks and other equipment.

2.1.3 Main Gun

Armament varies from machine guns to large cannons. In turreted vehicles, normally the heaviest armament is in the turret. Main gun identification features include:

- The presence and location along the gun tube of a bore evacuator.
- The presence of a muzzle brake or blast deflector. Types of muzzle brakes:
 - Single baffle.
 - Double baffle.
 - Multi-baffle.
- The presence or absence of a thermal jacket.

2.1.4 Commander's Station

This is usually a simple hatch or a cupola. A cupola is a small turret-like projection on the top of the turret that houses the commander's station, either on the right or left side. A cupola usually mounts a machine gun.

2.2 Projectiles

2.2.1 Kinetic Energy Projectiles

The kinetic energy (KE) projectile uses high velocity and mass to penetrate its target. Penetration depends directly on the projectile's velocity, weight, and the angle at which it hits. Projectiles may have incendiary (tracer) pellets to aid in aiming and provide an incendiary effect. Incendiary projectiles can be used to penetrate a target and ignite its contents [34].

Types of KE projectiles include:

2.2.1.1 Ball

Normally of a relatively small caliber (5.56 to 14.5 millimeters) and fired from pistols, rifles, and machine guns. The round's projectile penetrates soft targets on impact at a high velocity.

2.2.1.2 Antipersonnel (APERS)

Payload of APERS consists of a large number of hardened steel darts (flechettes). Detonation of the projectile sprays a cloud of flechettes into the target area. APERS rounds intended for direct fire artillery defense at close range are usually fuzed to detonate on muzzle action. They are also known as flechette, beehive, or cannister.

2.2.1.3 Armor Piercing (AP)

AP are designed to penetrate armor plate and other types of homogeneous materials. Armor piercing projectiles have a special jacket encasing a hard core or penetrating rod which is designed to penetrate when fired with high accuracy at an angle very close to the perpendicular with respect to the target.

2.2.1.4 Armor Piercing Discarding Sabot (APDS)

APDS consists of a sub-caliber penetrator rod encased in a light metal or plastic sabot. Centrifugal force and air pressure cause the sabot to discard on leaving the gun barrel. The penetrator rod is spin-stabilized.

2.2.1.5 Armor Piercing, Fin-Stabilized Discarding Sabot (APFSDS)

APFSDS is similar to APDS, but the penetrator is fin-stabilized.

2.3 Chemical Energy

The chemical energy (CE) projectile uses some form of chemical heat and blast to achieve penetration. It detonates either at impact or when maximum penetration is achieved. Chemical energy projectiles carrying impact-detonated or delayed detonation high-explosive charges are used mainly for direct fire from systems with high accuracy and consistently good target acquisition ability. Types of CE projectiles are discussed below.

2.3.1 High Explosive (HE)

It causes blast, fragmentation, and incendiary damage to the target. HE is the most common type of mortar and artillery round.

2.3.2 High Explosive Anti-Tank (HEAT)

It is designed to detonate a shaped charge on impact. At detonation, an extremely high velocity molten jet is formed. This jet penetrates a large thicknesses of armor, continues along its path, and sprays molten metal inside the target. If the jet hits an engine or ammunition, it may start a fire or cause an explosion. Rotation reduces the effectiveness of HEAT rounds, so spin-stabilized projectiles usually do not use HEAT warheads. HEAT rounds generally range in size from 60 to 120 mm. As a rule of thumb, a HEAT round can penetrate armor up to five times the warhead's diameter (e.g. a 100mm round can penetrate 500mm). Tanks, anti-tank weapons, and automatic cannons usually use these types of projectiles. Figure 2.2 shows how a warhead penetrates rolled homogeneous steel armor. The details are discussed below.

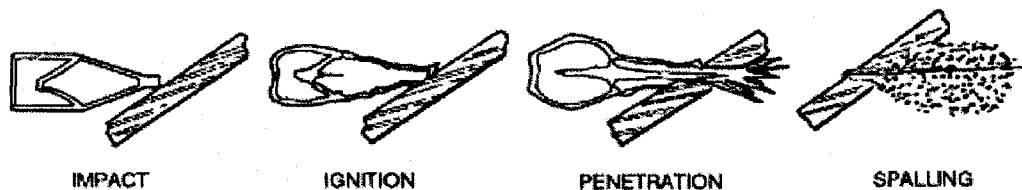


Figure 2.2: Warhead Penetrates Rolled Homogeneous Steel Armor [34]

2.3.2.1 Impact

The nose cone crushes; the impact sensor activates the fuze.

2.3.2.2 Ignition

The ogive crush switch activates the electric detonator. The booster detonates, initiating the main charge.

2.3.2.3 Penetration

The main charge fires and forces the warhead body liner into a directional gas jet that penetrates armor plate.

2.3.2.4 After-Armor Effects (spalling)

The projectile fragments and incendiary effects produce blinding light and destroy the target's interior.

2.3.3 High Explosive Plastic (HEP)

It flattens against the target on impact then explodes. The armor is not penetrated, but the shock wave knocks a scab off the inside of the armor plate which bounces around the interior of the target at high speed. Unlike HEAT, HESH projectiles have a secondary antipersonnel capability. Also known as high explosive squash head (HESH).

2.3.4 Flame Weapons

Flame weapons are characterized by both physical (flame and overpressure) and psychological casualty-producing abilities. The intense flame may also exhaust the oxygen content of inside air causing respiratory injuries to occupants shielded from the flaming fuel. Flame does not normally need to be applied with pinpoint accuracy to accomplish its mission. Flame weapons include flamethrowers, incendiary grenades, white phosphorus (WP) artillery shells, and fuel-air/thermobaric munitions. Fuel-air (aka thermobaric) munitions disperse fuel into the atmosphere forming a fuel-air mixture that is detonated. The fuel is usually contained in a metal canister and is dispersed by detonation of a central burster charge carried within the canister. Upon proper dispersion, the fuel-air mixture is detonated. Peak pressures created within the detonated cloud reach 300 pounds per square inch (psi). The ability of thermobaric weapons to provide massed heat and pressure effects at a single point in time cannot be reproduced by conventional

weapons without massive collateral destruction. Flame weapons can be used against fortified positions, interior buildings, tunnels (to include subways and sewers), and open areas. They can also be used to control avenues of approach for personal and lightly armored vehicles. When employed properly, even if the round or burst misses, enough flaming material and overpressure enters the position or area to cause casualties and disrupt operations. Thermobaric munitions will provide a more effective and selective flame capability that is easier and safer to employ at all levels of tactical operations without the side effect of large area destruction due to uncontrolled fires.

2.4 Armor Protection

Armor protection must dissipate a projectile's energy and thus prevent total penetration. Shielding against kinetic energy (KE) projectiles should initially stop or deform the projectiles in order to prevent or limit penetration. KE survivability considerations include oblique impact, or impact of projectiles at other than a perpendicular angle to the target surface, which increases the apparent thickness of the armor and decreases the possibility of penetration. The potential for ricochet increases as the angle of impact from the perpendicular increases.

2.4.1 Improved Armor Technology

Improvements in armor technology are becoming much more common worldwide. Many older tanks and armored vehicles are being retrofitted with improved armor, so it is not just newer vehicles which protection. These advanced armor configurations improve the vehicles' survivability against all weapons, but for the most part they are specifically designed to protect against HEAT (high explosive anti-tank)

warheads. This is a complex technical subject, and growing more so every year, but essentially these improved types of armor fall into four categories.

2.4.1.1 Reactive Armor

Reactive armor comes in several varieties, but the principle is essentially the same on all. The armor consists of blocks of explosives sandwiched between two metal plates and bolted on the outside of the vehicle. Small-arms and artillery shrapnel will not set off the blocks. However, when a HEAT round strikes the block, the explosive ignites and blows outwards. The blast and the moving steel plates disperse and deflect the jet of the HEAT warhead, dramatically reducing its ability to penetrate armor. Many countries are now fielding different versions of reactive armor, which can be easily be retrofitted onto older vehicles.

2.4.1.2 Laminated Armor

It consists of flat layers of steel armor plate with layers of ceramics, fiberglass, or other nonmetallic materials in between. This armor is highly effective against all types of weapons, but is difficult and expensive to manufacture.

2.4.1.3 Composite Armor

Composite armor consists of a nonmetallic core (usually some kind of ceramic) around which the rest of the steel of the hull or, more commonly, the turret, is molded. This is much more effective than conventional steel armor against all types of weapons, but less so than laminated armor. However, it is less difficult and expensive to manufacture. Hulls made of composite armor do not have to be slab sided, like those made of laminated armor.

2.4.1.4 Applique Armor

Applique armor is essentially extra plates mounted or welded on top of the hull or turret of a vehicle. They can be made of any material, but are frequently made of ceramic or laminated materials. Like reactive armor, applique armor is an easy and cost-effective way of improving the protection of older vehicles.

2.5 Latest Developments

TARDEC has taken up several projects for modernizing armored vehicles. The work being done is consistent with Strategic Planning Guidance, the Army Science and Technology Master Plan (ASTMP), the Army Modernization Plan and the Defense Technology Area Plan (DTAP) of the United State Defense. The present work is part of one of its projects, Combat Vehicle and Automotive Technology (C05) performed in collaboration with the Army Research Lab (ARL). This project investigates, designs and develops advanced armor materials, advanced structural armors ballistic defeat mechanisms, and armor packaging solutions to achieve light weight, ballistically-superior armors/structures that provide the last line of defense for Future Combat Systems (FCS) and Future Force vehicles. The effort also provides for analysis, modeling, and characterization of advanced armor solutions designed to protect against collateral damage from residual debris generated by the Active Protection (AP) threat defeat mechanisms. The major focus is on providing technology solutions that decrease weight, reduce space claims and lower the cost for protection against medium kinetic energy (KE) projectiles, chemical energy (CE) war heads, Explosively Formed Penetrators (EFPs) and blast fragments from mines. Ballistic protection technologies developed under this project will be evaluated and incorporated into the Integrated Survivability

Advanced Technology Demonstration (IS ATD). The goal of the IS ATD is to provide “convincing evidence” of the superiority of a “layered” approach to survivability [36].

2.6 The APC M113

The M113A1, informally known as the Gavin, is a lightly armored full tracked air transportable personnel carrier designed to carry personnel and certain types of cargo. The M113-family was developed from M59 and M75 by Ford and Kaiser Aluminum and Chemical Co. in the late 1950's. The vehicle is capable of: amphibious operations in streams and lakes; extended cross country travel over rough terrain; and high speed operation on improved roads and highways. The M113 is a lightly armored personnel carrier that provides good mobility combined with fair firepower and protection. The M113 APC is used to transport and position combat troops and supplies. The M113/A1/A2/A3 is capable of LAPES (low altitude parachute extraction system) and LVAD (low velocity air drop) operations. The details of APC M113 A1, APC M113 A2 and APC M113 A3 will be discussed in this section.

2.6.1 APC M113 A1 Armored Personnel Carrier

The first major upgrade came in 1964 with the introduction of the M113A1 package which replaced the original gasoline engine with a 212 horsepower diesel package. The new power train was soon incorporated into the existing vehicle family as the M113A1 (Figure 2.3), M577A1, and M106A1, as well as several new derivative systems. Some of these new derivatives were based on the armored M113 chassis (the M125A1 mortar carrier and M741 "Vulcan" air defense vehicle) while others were based on an unarmored version of the chassis (including the M548 cargo carrier, M667 "Lance" missile carrier,

and M730 "Chaparral" missile carrier). Continuing modernization efforts led to the introduction of the A2 (Figure 2.4) package of suspension and cooling enhancements in 1979.

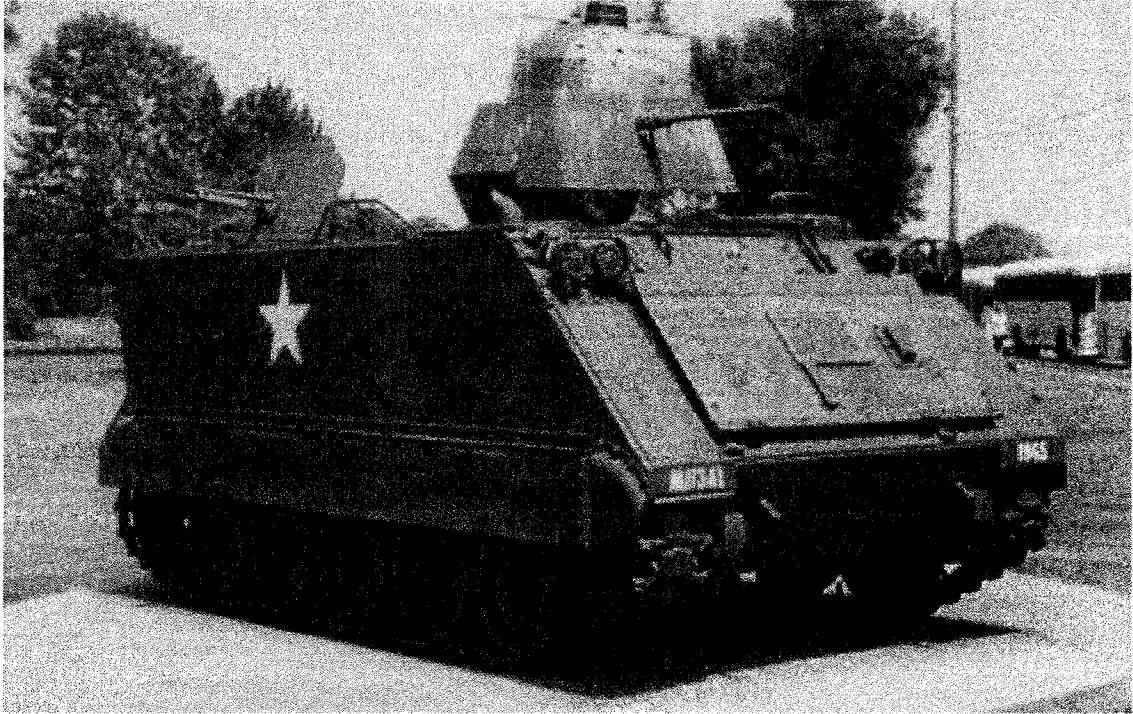


Figure 2.3: APC M113A1 Armored Personnel Carrier [35]

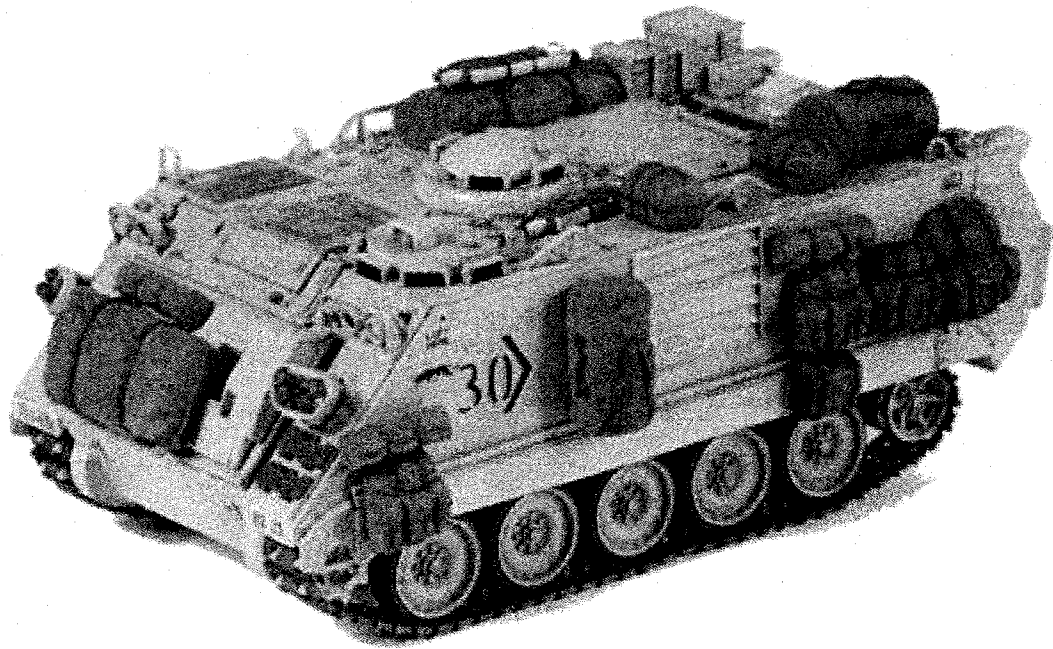


Figure 2.4: APC M113A2 Armored Personnel Carrier [35]

2.6.2 APC M113A3 Armored Personnel Carrier

The M113A3 is a full-tracked armored personnel carrier provides protected transportation and cross country mobility for personnel and cargo. A light armored vehicle weighing 27,200 pounds, it carries 11 infantry personnel in addition to the vehicle driver and track commander. It is capable of sustained speeds of 41 mph on level roads and accelerates from 0 to 35 mph in 27 seconds (this compares to 69 seconds for the M113A2).

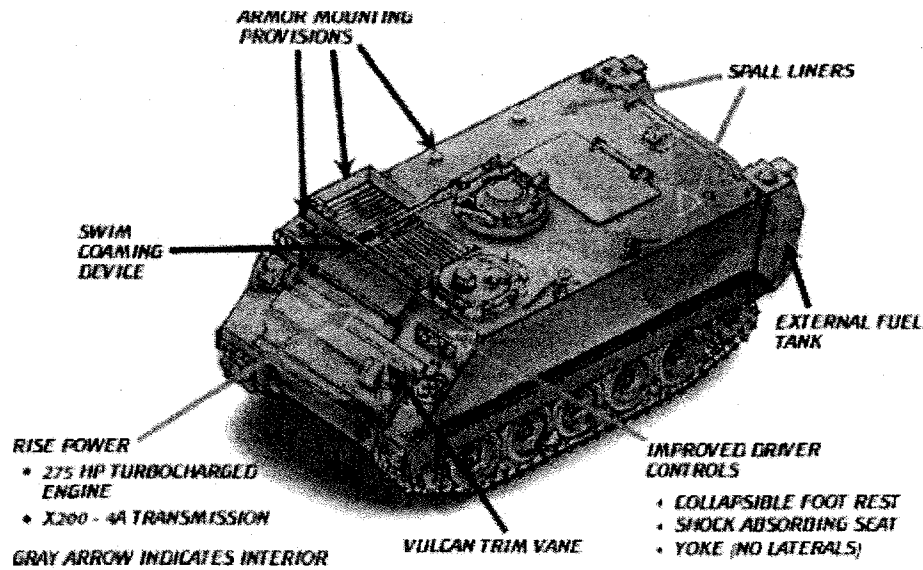


Figure 2.5: APC M113A3 Armored Personnel Carrier [35]

The M113A3 is a product improved version of the M113A2 with improved transmission and engine. The U.S. Army first identified the need to up-power the M113A2 carrier in the mid-1970s. This need was driven by increases in vehicle weight and a requirement to increase the mobility and survivability of the system. Steering is improved with an automotive-type steering yoke and foot brake arrangement which improves driver control, lessens fatigue and simplifies driver training from that of the A1/A2 steering/braking laterals. Due to load matching ability and increased steering capability, cross country performance is also improved.

Crew survivability is increased by the addition of spall suppression liners and locating the fuel tanks externally, on the rear of the vehicle. The inside of the vehicle (sides, roof and rear) are covered with spall suppression liners which limit troop injuries from the effect of overmatching weapons by restricting the spread of spall when a round penetrates the hull. External fuel tanks free up 16 cubic feet of usable space inside the

vehicle and reduce the fire hazard inside the crew compartment. Two tanks and independent valving provide redundancy in the fuel system allowing continued operation when one tank is damaged. External differences between M113A2 and M113A3 include external fuel tanks and provisions for the installation of an add-on-armor kit.

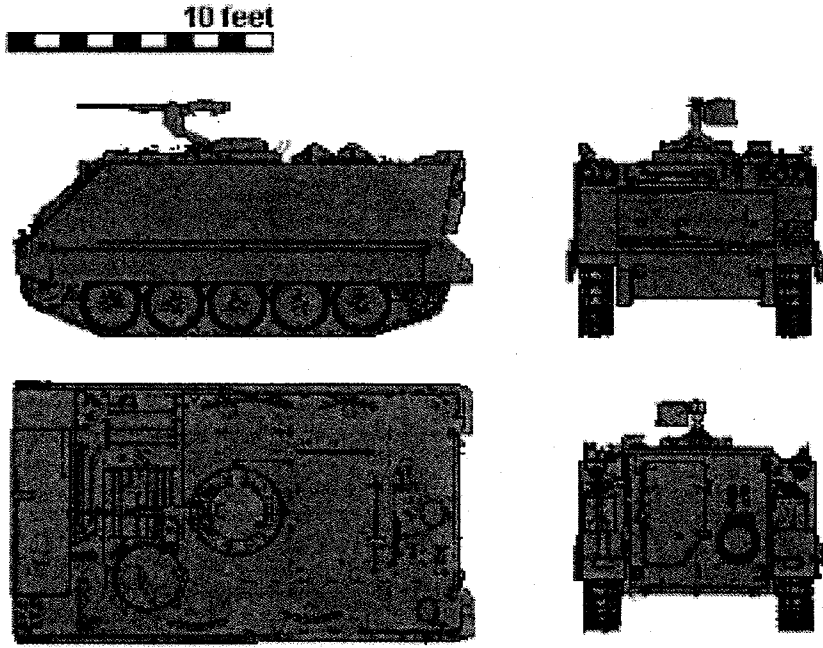


Figure 2.6: Different views of an APC M113 [35]

Table 2.1: Specifications of APC M113 [35] (Table continued in the next page)

General	
Length	191.5"
Width	105.75"
Height	86.5"
Clearance	16"
Weight, combat loaded	27,180 lb. (12,329 kg)
Maximum weight	31,000 lb. (14,061 kg)
Net weight	23,880 lb. (10,832 kg)
Air drop weight	22,128 lb. (10,037 kg)
Personnel capacity	2 + 11
Fuel tank capacity	95 gallons (360 liters)
Ground pressure	8.63 psi (0.60 kg/cm ²)
Performance	
Speed on land	41 mi/h (66 km/h)
Speed in water, with track	3.6 mi/h (5.8 km/h)
Cruising range	300 mi (483 km)
Turning radius	Pivot to infinite
Slope	60%
Side slope	40%
Trench crossing	66 in. (168 cm)
Vertical wall climbing	24 in. (61 cm)
Braking (20-0 mi/h)	40 ft.
Engine	
Make and model	Detroit Diesel 6V53T
Displacement	318 in.3 (5.2 liter)
Fuel	Diesel (DF2)
Rated horsepower	275 hp
Gross horsepower-to-weight ratio	20.2 hp/ton
Transmission, Automatic	
Make and model	Allison X200-4B
NOTE: Table is continued in the next page	
Steering	Hydrostatic
Brake type	Multiple wet plate
Running Gear	
Suspension	Torsion bar
Road wheels	5 per side, 24 inch diameter (61 cm)
Track type	Steel single pin, detachable rubber pad
Number of shoes	63 left, 64 right
Track pitch	6 in. (15.2 cm)
Track width	15 in. (38 cm)
Shock absorbers	3 per side
Wheel travel	9.0 in. (22.9 cm)

Electrical System	
Generator	
Amperes	200, 300 optional
Volts, dc	28
Batteries	4, type 6TL, 120 amp-hr, 12-volt each
Armament	
50 cal MG	2,000 ready rds.
Armor	
Basic hull	5083 Aluminum
Bolt-on armor kit	Steel armor
Mine armor	Steel armor
Gun shield kit	Steel armor
Spall suppressant	Composite panel
Fire Extinguishers	
Fixed	5 lb. (2.3 kg) CO2 for engine compartment
Portable	5 lb. (2.3 kg) CO2

2.7 Model 1

The Armored Personnel Carrier (APC) designated as APC M113 A2 is labeled as Model 1 for studying the shock transmission due to a mine blast load in this thesis. The work performed by Das Gupta et al. [11] provided basic inputs for the construction of the model. Overall length, width and height of the vehicle are 4.863 m, 2.686 m and 2.5 m respectively while the height till the flat roof is 1.422 m. As can be seen from Figure 2.7, the vehicle consists of several complex assemblies and sub assemblies which are integral part of the vehicle. If all these models are incorporated in a Finite Element Model there is a high possibility of accurately predicting the dynamic behavior of the vehicle under a mine blast. However, some parts like doors, hatches do not play a major role in the overall structural integrity of the vehicle. In addition to this, incorporating all the details makes the overall study process computationally expensive. Hence, a more simplified model is chosen for this study. The simplified model of the vehicle designed in the solid

model is shown in the Figure 2.7. The details of the geometry are shown in the Figure 2.8 and Table 2.2.

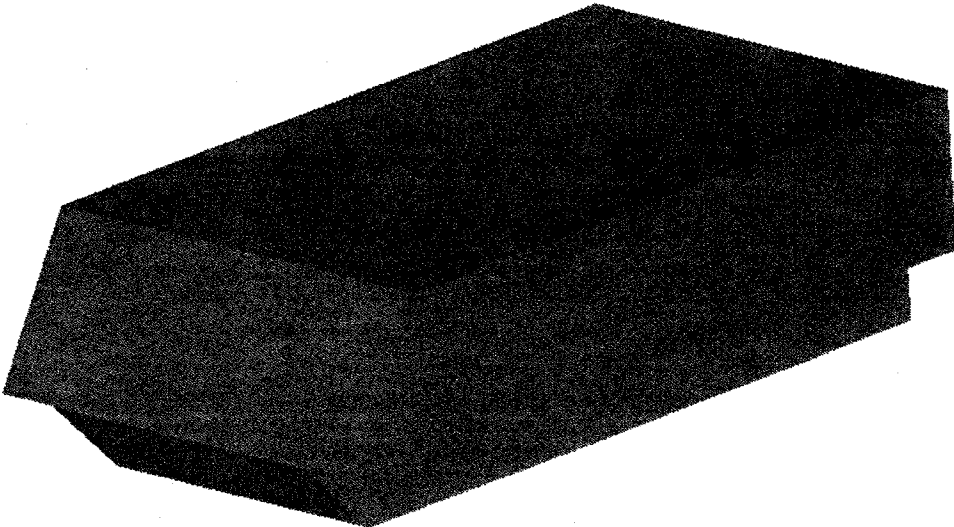


Figure 2.7: Model 1

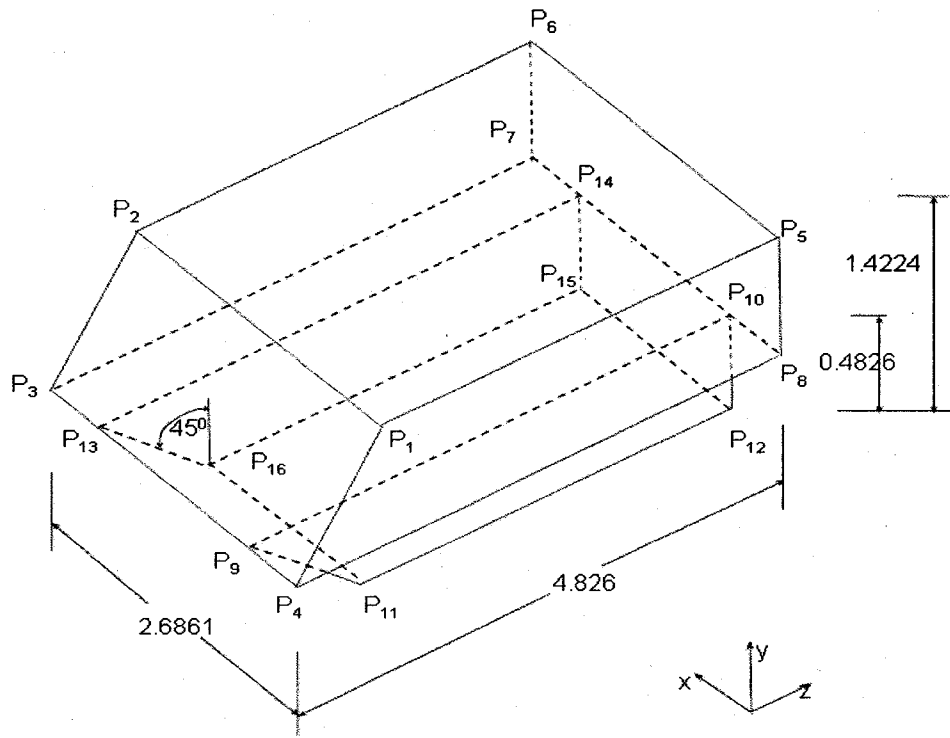


Figure 2.8: Dimensional Details of Model 1

Table 2.2: Key Point details (Dimensions accurate to a tenth of a mm)

Keypoints	X Coordinate (m)	Y Coordinate (m)	Z Coordinate (m)
P ₁	0.0000	1.4224	0.5425
P ₂	2.6860	1.4224	0.5425
P ₃	2.6860	0.4826	0.0000
P ₄	0.0000	0.4826	0.0000
P ₅	0.0000	1.4224	4.8260
P ₆	2.6860	1.4224	4.8260
P ₇	2.6860	0.4826	4.8260
P ₈	0.0000	0.4826	4.8260
P ₉	0.3810	0.4826	0.0000
P ₁₀	0.3810	0.4826	4.8260
P ₁₁	0.3810	0.0000	0.4826
P ₁₂	0.3810	0.0000	4.8260
P ₁₃	2.3050	0.4826	0.0000
P ₁₄	2.3050	0.4826	4.8260
P ₁₅	2.3050	0.0000	4.8260
P ₁₆	2.3050	0.0000	0.4826
Commander	1.5350	0.0000	2.0620
Driver	0.7658	0.0000	0.8775
Panel	0.0000	0.7959	0.6031

2.7.1 Critical Locations on the Vehicle

As can be seen from the Figure 2.8, the whole vehicle is built in the form of a hollow box with walls of specified thickness. The study is concentrated on the effects of shock propagation in the whole structure due to a mine blast located at a specified depth below the vehicle. The effect of this destructive mine blast on the vehicle crew safety and the

effectiveness of the electronic component is studied using this model. The critical points identified for this study are the locations of the driver seat, the commander seat and the instrument panel location. The severity of the shock at these locations is measured in terms of peak and RMS accelerations.

2.8 Model 2

This model is related to the development of a light weight space frame for the IS ATD vehicle. The final design of the IS ATD vehicle is still under development; however a targeted model of the vehicle is shown in the Figure 2.9. The space frame is incorporated within the vehicle as shown in the Figure 2.10. A representative model of the IS ATD vehicle, called AX-1 is used by the ARL for testing its behavior under gun firing, mobility racking and mobility bending load cases. The proposed AX-1 model is shown in the Figure 2.10. This model represents the upper half of the IS ATD vehicle. The space frame is a non-monolithic type with several joints and struts making up the entire structure. In the present study, Model 2 i.e. AX-1 deals with the response of the structure against gun firing case. However, in this model parts like doors, hatches etc have not been considered as they do not play significant role in the overall structural integrity of the vehicle. In addition to this, incorporating all the details makes the overall study process computationally expensive.

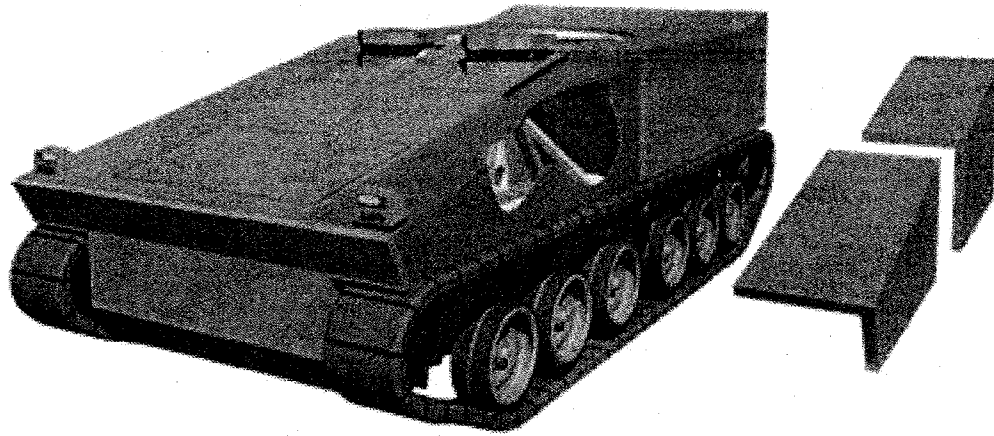


Figure 2.9: IS ATD Vehicle [31]

2.8.1 Details of Model 2

The overall dimensions of the space frame are 4.05 m in length, 1.94 m in width and 0.76 m height while the height at the frontal portion of the space frame is 0.25 m. The detailed locations of each node are shown in the Table 2.3. Numbers in the figure indicate nodes (joining locations) and the origin is located at the middle of the strut along the nodes 5, 8 and is indicated by the letter 'o' in the figure. It is to be noted that the space frame is symmetric about the plane XY. The details of the length of joints at each nodal point are shown in Tables. A simple notation has been used to describe the length of joints at each node and the type of cross section used. For example, LN_{8-7} indicates length of the joint at node location 8 along the line 8-7 and LN_{7-8} indicates length of the joint at node location 7 along the line 7-8 (Joints can be easily identified with changed color at each node location as shown in the Figure 2.10). Three types of cross sections rectangular tubing, angle and C-section have been used to construct the whole model. They are indicated by R, A and C respectively and are used in tables to indicate the type of cross section (CS) used at each joint. The details of the cross sections used in building

the space frame are shown in Figures 2.11, 2.12, 2.13 and Table 2.5. Since the model is symmetric about the plane XY , details on only one side are provided.

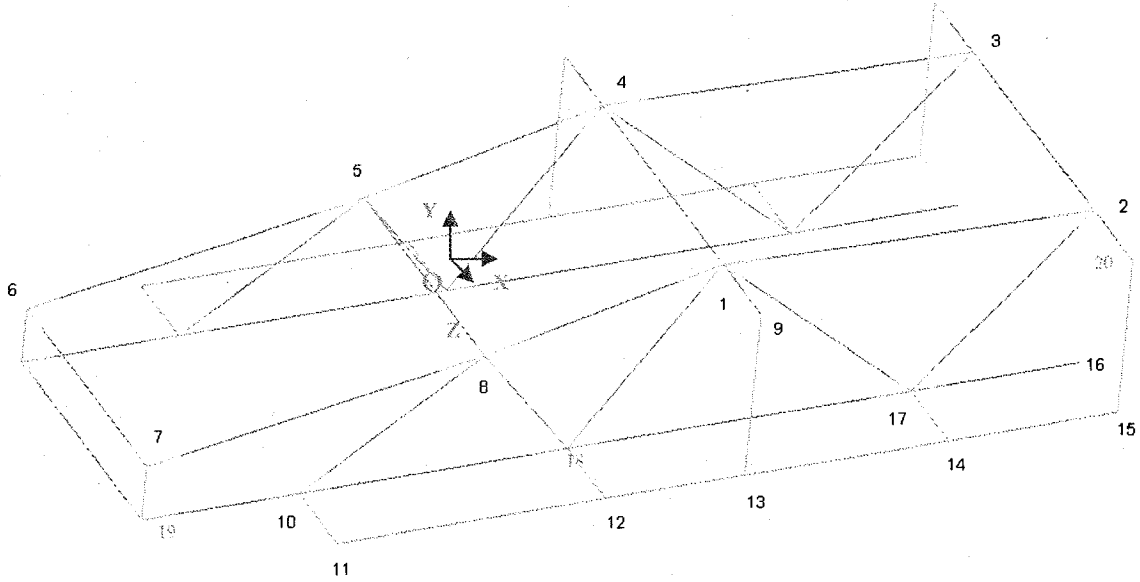


Figure 2.10: Simple Line Model with Node Point Locations of the AX-1 Space Frame

Table 2.3: Node Point Coordinates of the AX-1 Space Frame

Node	X-Coordinate	Y-Coordinate	Z-Coordinate
1	0.919	0.138	0.597
2	2.616	0.207	0.597
3	2.618	0.206	-0.597
4	1.891	-0.512	0.597
5	2.460	-0.512	0.597
6	-1.441	-0.259	-0.597
7	-1.441	-0.259	0.597
8	0.000	0.000	0.597
9	1.008	0.249	0.972
10	-0.759	-0.512	0.972
11	-0.759	-0.512	0.972
12	0.400	-0.512	0.972
13	1.008	-0.512	0.972
14	1.891	-0.512	0.972
15	2.460	-0.512	0.375
16	2.460	-0.512	0.597
17	1.891	-0.512	0.597
18	1.008	-0.512	0.972
19	-1.441	-0.512	0.597

Table 2.4: Length of Joints at Nodes

Location	Length	CS	Location	Length	CS	Location	Length	CS
LN ₁₋₈	0.196	R ₁	LN ₇₋₈	0.148	R ₁	LN ₁₈₋₈	0.120	R
LN ₁₋₁₈	0.142	R ₁	LN ₇₋₆	0.148	R ₁	LN ₁₂₋₁₈	0.057	C
LN ₁₋₉	0.077	R ₁	LN ₇₋₈	0.253	R ₁	LN ₁₃₋₉	0.002	C
LN ₁₋₄	0.077	R ₄	LN ₁₉₋₆	0.148	R ₁	LN ₉₋₁	0.143	R ₂
LN ₁₋₁₇	0.147	R ₁	LN ₁₉₋₁₀	0.148	R ₁	LN ₉₋₁₃	0.051	R ₃
LN ₁₋₂	0.195	R ₁	LN ₁₅₋₂₀	0.002	C	LN ₁₄₋₁₇	0.057	C
LN ₂₋₁	0.190	R ₁	LN ₁₀₋₁₉	0.143	R ₁	LN ₁₇₋₁₈	0.143	R ₁
LN ₂₋₁₇	0.089	R ₁	LN ₁₀₋₁₁	0.057	C	LN ₁₇₋₁₄	0.057	C
LN ₂₋₂₀	0.077	R ₁	LN ₁₀₋₁₈	0.143	R ₁	LN ₁₇₋₁₆	0.143	R ₁
LN ₂₋₃	0.077	R ₁	LN ₁₀₋₈	0.143	R ₁	LN ₁₇₋₂	0.124	R ₁
LN ₈₋₇	0.197	R ₁	LN ₁₁₋₁₀	0.057	C	LN ₁₇₋₉	0.120	R ₁
LN ₈₋₁₀	0.134	R ₁	LN ₁₈₋₁₀	0.143	R ₁	LN ₂₀₋₂	0.143	R ₂
LN ₈₋₁₈	0.134	R ₁	LN ₁₈₋₁₂	0.057	C	LN ₂₀₋₁₅	0.051	R ₃
LN ₈₋₁	0.198	R ₁	LN ₁₈₋₁₇	0.143	R ₁	All dimensions are in m.		
LN ₈₋₅	0.077	R ₄	LN ₁₈₋₁	0.124	R ₁			

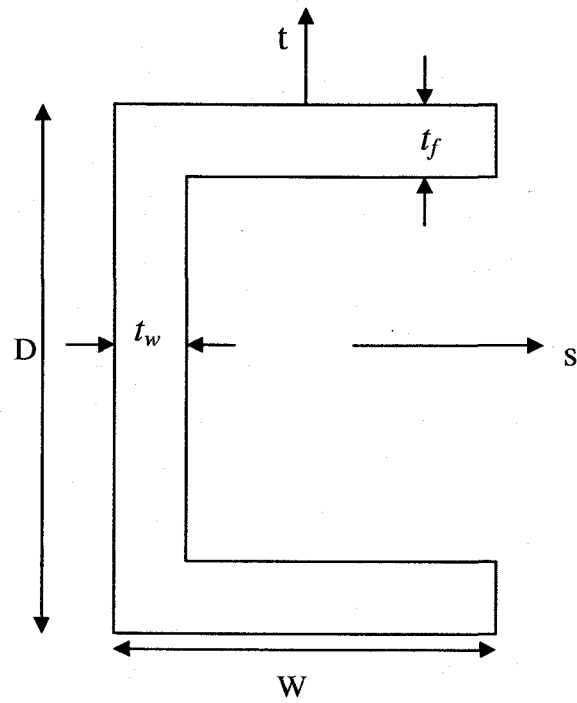


Figure 2.11: C Cross Section Parameters

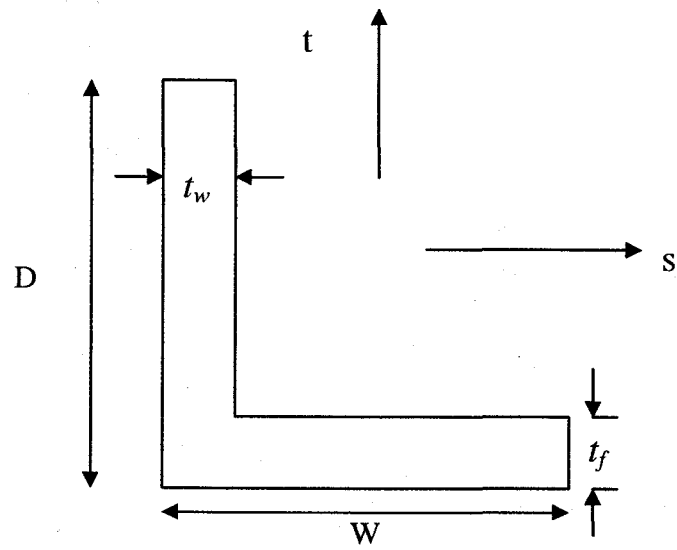


Figure 2.12: Angle Cross Section Parameters

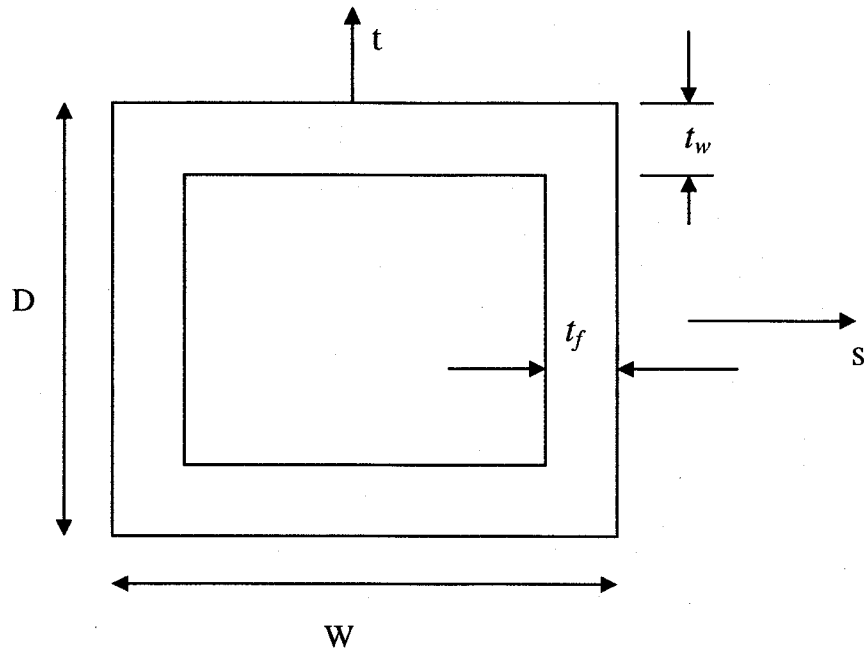


Figure 2.13: Rectangular Cross Section Parameters

Table 2.5: Cross Sectional Parameter Values for the Space Frame

CS Type	D	W	t_w	t_f
R ₁	0.102	0.102	0.0127	0.013
R ₂	0.102	0.102	0.0127	0.013
R ₃	0.076	0.076	0.0127	0.013
R ₄	0.023	0.140	0.0318	0.008
C	0.076	0.038	0.0127	0.013
A (Angle Bar)	0.057	0.067	0.0159	0.016
R (Strut1)	0.076	0.076	0.0064	0.006
R (Strut2)	0.051	0.051	0.0064	0.006

CHAPTER 3

DETAILS OF FINITE ELEMENT MODELS

3.1 Units

In this work, SI units have been used throughout the modeling and analysis.

Basic Units

Length: meter (m)

Mass: kg

Time: sec

Derived Units

Displacement: meter or m

Velocity: meter/sec or m/s

Acceleration: meter/sec² or m/s²

Force: Newton (N) or kg.m/s²

Stress: Newton/meter² or N/m² or Pascal (Pa). Also MPa = 10⁶ Pa is used.

Strain: m/m (dimensionless)

3.2 Model 1

3.2.1 Steps for Finite Element Analysis

As discussed before, Model 1 represents the main model for studying the shock transmission across the bottom panel of the armored vehicle due to a mine blast. The steps in creating the finite element analysis of this model are described below:

- Step I: Create the geometry using ANSYS 8.0 preprocessor.

- Step II: Define material properties, meshing, boundary conditions and application of appropriate loading condition that can simulate the mine blast.
- Step III: Solve the model using the explicit finite element code LS-DYNA.
- Step IV: Post-process results using LS-POST or HyperView.

3.2.2 Modeling

Finite element model of the simplified APC M113 vehicle is created using ANSYS 8.0 Preprocessor. The geometry of the entire vehicle is created by entering the key point locations as specified in Table 2.2. These key points are joined to obtain lines. The lines are then used to obtain rectangular or trapezoidal areas. The created geometry is shown in the Figure 3.1

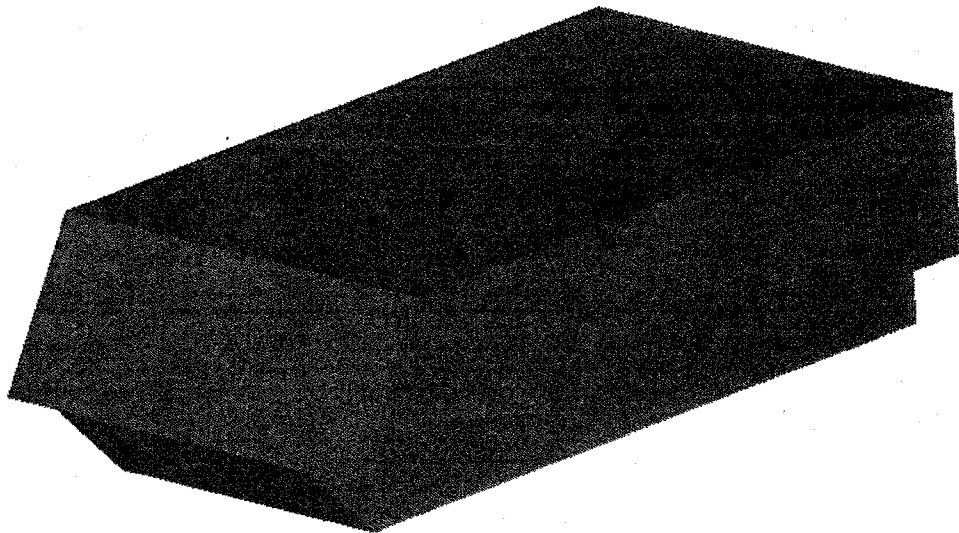


Figure 1: Simplified APC M113 Model

3.2.3 Meshing

The areas created were meshed using shell elements. Shell elements have been used to reduce computational time compared to using solid elements. 3D eight noded shell elements have been used for meshing the entire vehicle. Belytschko–Lin–Tsay type shell element formulation is used because of its computational efficiency. This element formulation requires less mathematical operations than the Hughes-Liu element formulation type [32]. Mesh stability study conducted by Naraparaju [30] showed that a uniform mesh of 0.04 m can be used to model projectile impact on the vehicle. Therefore, the model is meshed with a uniform size of approximately 0.04 m as shown in the Figure 3.2.

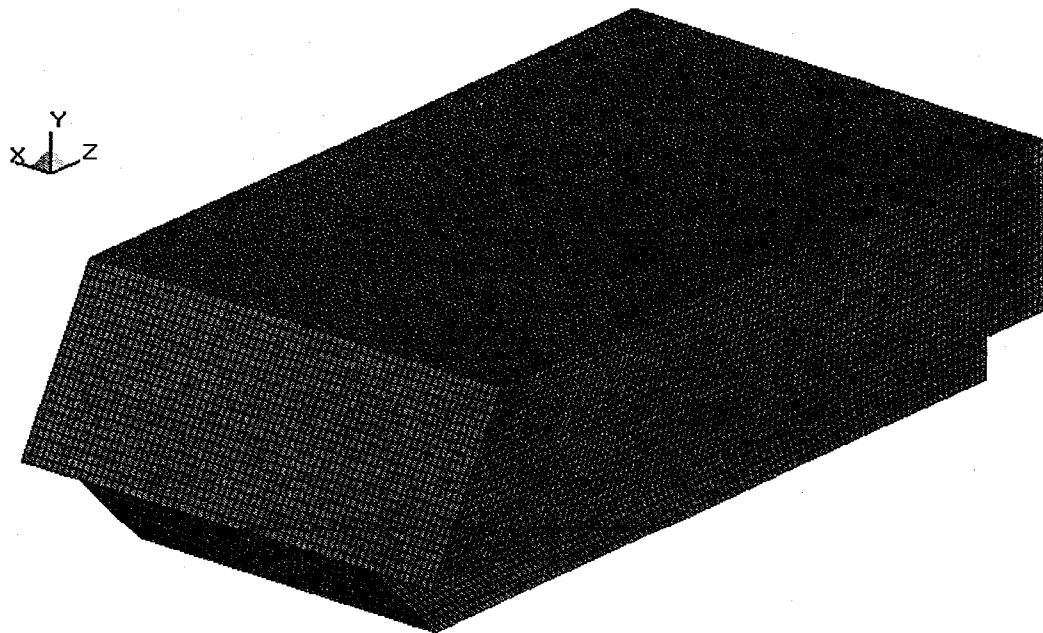


Figure 3.2 Meshed APC M113 Model

3.2.4 Boundary Conditions

3.2.4.1 Effect of Ground Surface

In order to simulate the resting of the vehicle on the ground surface, an infinite rigid wall is defined below the vehicle. This is the only boundary condition defined for the vehicle model 1. The rigid wall acts as an obstacle and does not allow any penetration of the referred elements (All elements of the vehicle in this case) under any loading conditions. A rigid wall does not take in to account the effect of soil properties or its individual fragments or combination of it. In order to assess the effect of vehicle-ground friction on the displacement response of the vehicle, a parametric study is conducted. It has been found that there is no significant change in the displacement response when coefficient of friction is added to the model. Hence, its effect is not considered in this case. The rigid wall boundary condition is shown in the Figure 3.3. The distance between the vehicle bottom panel and the rigid wall is 0.43m. However, if the effect of gravity is considered, there is a possibility that during the simulation process the vehicle may fall under gravity. To avoid this, a small simulation time of 30 ms, sufficient to neglect such an effect is considered.

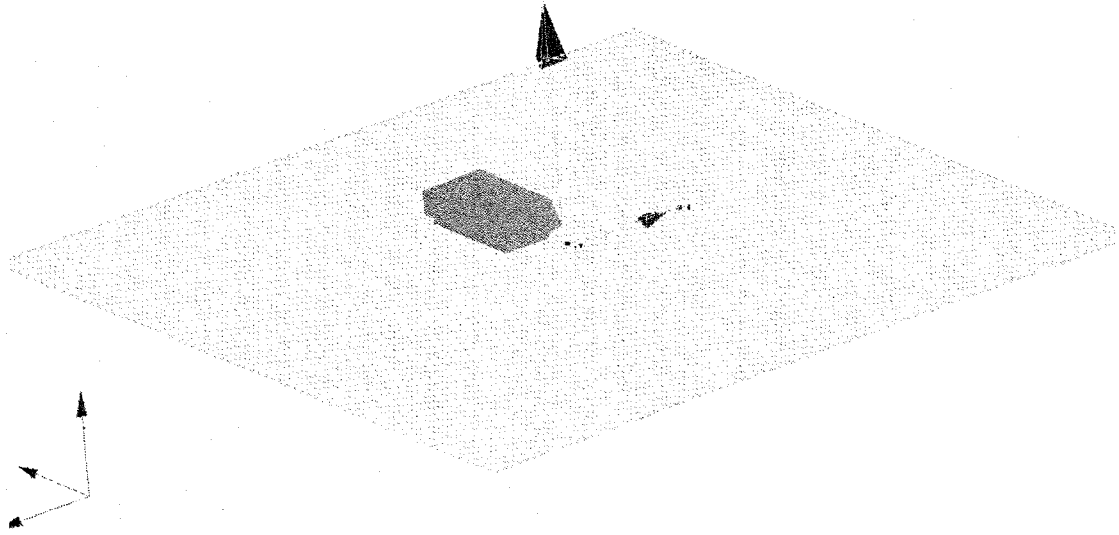


Figure 3.3 Rigid Wall Boundary Condition

3.2.4.2 Effect of Gravity

The effect of acceleration due to gravity on the dynamic response of the vehicle is considered in the model. An acceleration value of 9.81 m/s^2 is defined to consider this effect.

3.2.5 Loading Conditions

To simulate the mine blast, ConWep (Conventional Weapon) code, which is embedded in LS-DYNA is used. Many subroutines are implemented in the ConWep blast algorithm. First, the angle of incidence and distance between the surface segment and detonation point are calculated. The angle of incidence is the angle between the surface normal and the vector from the mid-surface node to the point of detonation, Figure 3.4. The time of arrival (T_a), time duration (T_d), peak incident and reflect pressures (P_i and

P_r), and incident and reflected pressure decay coefficients (a and b) can be determined based on these inputs [33]. The equations used in this process are listed below.

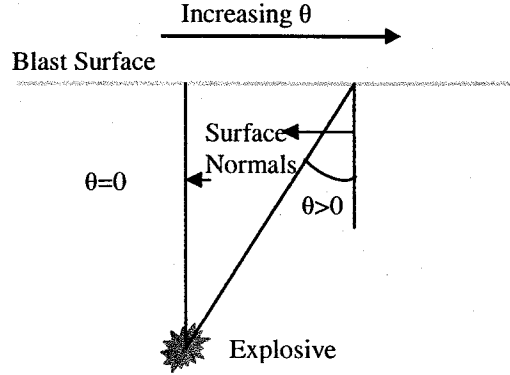


Figure 3.4 ConWep Illustration

$$t = M_i - Ta \quad (3.1)$$

Where M_i is model time

$$\text{Incident Pressure, } P(t) = P_i \left(1 - \frac{t}{T_d} \right) \exp\left(-at/T_d \right) \quad (3.2)$$

$$\text{Reflected Pressure, } P(t) = P_r \left(1 - \frac{t}{T_d} \right) \exp\left(-bt/T_d \right) \quad (3.3)$$

$$\text{Pressure Load, } L(\theta) = P_r \cos^2(\theta) + P_i(1 + \cos^2(\theta) - 2\cos(\theta)) \quad (3.4)$$

A blast load of TNT equivalent 0.5 Kg is given at the location (1.343, -0.430, 2.654) m to simulate the mine blast. This position is located at the center of the bottom panel and 0.43 m below it. The bottom panel is given as the target surface where the pressure due to the mine blast is applied. The load location is shown in the Figure 3.5.

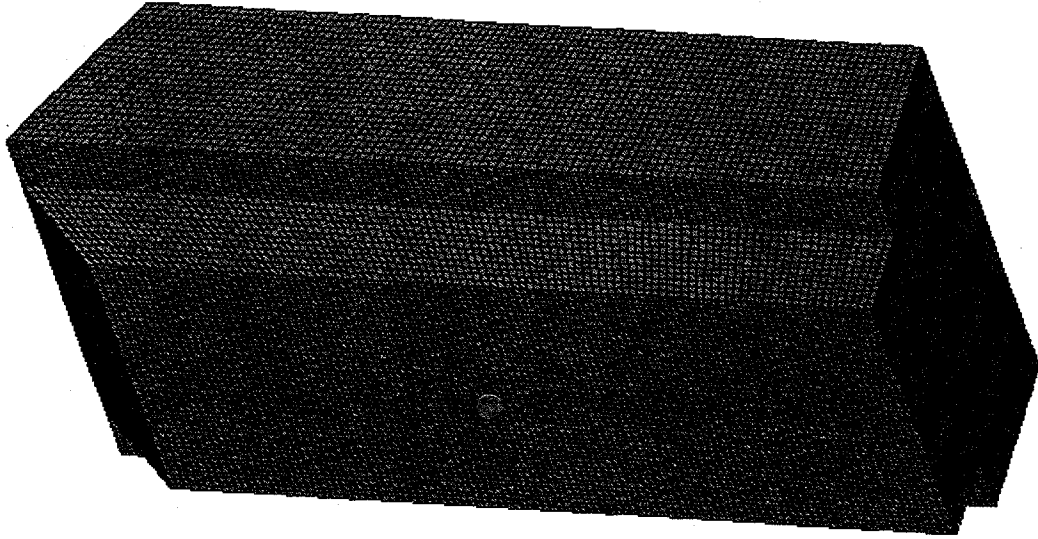


Figure 3.5 Load Location

3.2.6 LS-DYNA Cards

3.2.6.1 Control Card

Control cards are optional cards in an LS-DYNA input file and can be used to change the defaults, activate solution options such as mass scaling, adaptive remeshing, and an implicit solution. A control card defines the properties such as termination time, time step controls, warpage angle for shell, hourglass effect, rigid wall effect etc. A sample control card is given below.

```
*CONTROL_TERMINATION
$$ ENDTIM   ENDCYC   DTMIN   ENDENG   ENDMAS
      0.2       0       0.0     0.0     0.0
```

- ENDTIME in the card defines the termination time.

- ENDCYC defines the termination cycle. The termination cycle is optional and will be used if the specified cycle is reached before the termination time.
- DTMIN is the reduction factor for initial time step size to determine minimum time step.
- ENDENG is the percent change in energy ratio for termination of calculation. If undefined, this option is inactive.
- ENDMASS is the percent change in the total mass for termination of calculation. This option is relevant if and only if mass scaling is used to limit the minimum time step.

3.2.6.2 Database Card

Database card is written just after the title card. Database card defines the type of output format for results. The database card is shown below.

```
*DATABASE_BINARY_D3PLOT
$$ DT/CYCL      LCDT
      0.0025
      0
```

- DT/CYCL defines the time interval between the outputs. DT/CYCL is 0.25E-02, implies 10 D3Plots are generated for total simulation time of 0.025 seconds.
- LCDT is the optional load curve ID specifying the time intervals between the dumps.

3.2.6.3 Nodout Card

The Nodout card is used to define the number of data points intended when plotting a graph. The Database History Node card is used to define specific nodes for which the graphs are plotted. The Nodout card can be used to produce less number of D3plots with large number of data points. A sample card is shown below.

```

*DATABASE_NODOUT
$$      DT      BINARY
2.0000e-03      1
*DATABASE_HISTORY_NODE
$$      ID1      ID2      ID3
          1152      1505      6205

```

- DT is 2.0000E-03 implies 100 data points are retrieved for a termination time of 0.2 s.
- BINARY is 1 indicates the ASCII file is written.

3.2.6.4 Material Card

Material types and properties are defined in the material cards. The material properties used for the vehicle hull are those of Aluminum 7039-T64 [30]. In the actual stress strain curve, as shown in Figure 3.6, the stress goes up in a linear fashion to the yield point, then it increases non-linearly until it reaches the ultimate value. In the last phase, stress drops down until it reaches the failure point. For the purpose of FEA, this stress strain curve is simplified into a bilinear elastic plastic curve. In LS-DYNA, plastic-kinematic material model is selected. This material model covers for the stress strain curve in the elastic region (until yield stress) and also in the plastic region (beyond yield stress). The stress-strain curve is assumed to be linear within each of these regions. Such a simplified stress strain curve is shown in Figure 3.6 below. The slope of the stress-strain curve (from origin to the yield point) is defined as the Elastic Modulus of the material. The slope of the stress-strain curve (beyond yield point) is defined as the Tangent Modulus for this material model. To determine the linear portion of the curve in

the plastic region, the yield point is connected to the point $\left(\epsilon_f, \frac{s_u + s_{fu}}{2} \right)$.

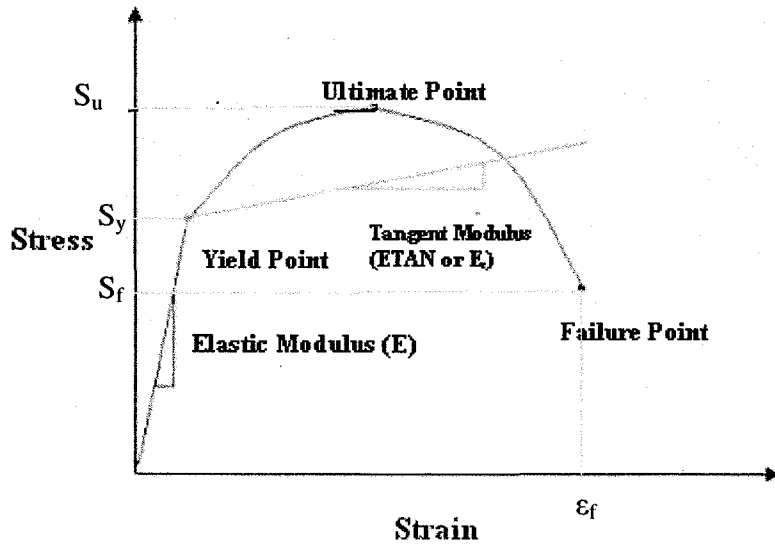


Figure 3.6 Typical and Simplified (Bilinear Material Model) Stress-Strain Curves

A sample material card is shown below and the various parameters used in the definition follow the card.

```

*MAT_PLASTIC_KINEMATIC
$-----1-----2-----3-----4-----5-----6-----7
$      MID      RO      E      PR      SIGY      ETAN      BETA
      1      2700.06.9000E+10      0.33      8000000      56200000      0.0
$-----8-----9-----10
$      SRC      SRP      FS
      0.0      0.0      0.13

```

- MID defines the material identification. RO defines the mass density (kg/m^3).
- E defines the Young's modulus (N/m^2). PR defines the Poisson's ratio.
- SIGY defines the Yield stress (N/m^2).
- ETAN defines the Tangent modulus (N/m^2).
- BETA defines the Hardening parameter.
- SRC defines the strain rate parameter, C, for Cowper Symonds strain rate model.

- SPR defines the strain rate parameter, P, for Cowper Symonds strain rate model.
- FS defines the failure strain for the eroding elements.

3.2.6.5 Loading Cards

ConWep blast function has inputs of TNT equivalent mass, type of blast (surface or air), location in space of detonation, and surface identification of which the pressure will be applied. ConWep calculates the appropriate pressure to be applied to the designated surface from this information. ConWep blast function is given using the *LOAD_BLAST card. A sample card is shown below.

```
*LOAD_BLAST
$WGT      XBO      YBO      ZBO      TBO      IUNIT      ISURF
0.50000   0.50000   -0.4300   2.6540   0        2          2
```

- WGT indicates the TNT equivalent mass of the explosive used;
- (XBO, YBO, ZBO) indicates the coordinates of the detonation point;
- TBO indicates time of explosion,
- IUNIT indicates the unit system used (2 is for SI units) and
- ISURF consists of 2 options for the type of blast which are air burst (option 1) and surface burst (option 2). In the present case option 2 is selected to confirm the load as mine blast. The detail of the card is shown below

To apply the ConWep blast function in LS-DYNA, two load curves should be given. These load curves are the requirement for the explicit code to run the simulation involving ConWep blast function. These are just used as a requirement and do not play any other role in the simulation process. The target surface where the pressure needs to be applied is given using the cards *LOAD_SEGMENT_SET and *SET_SEGMENT card. The *LOAD_SEGMENT_SET card used is shown below. The first value is used to refer

the target surface elements define by *SET_SEGMENT and the second value -2 is used to indicate that the load applied is due to ConWep blast function.

```
*LOAD_SEGMENT_SET  
1,-2
```

3.2.7 Results

The benchmarks for the shock analysis include the peak accelerations and the average values over the entire simulation period at the three critical locations specifies before (which are the commander seat, driver seat, and the instrumentation panel). The acceleration responses at the critical locations are shown in the Figure 3.7, 3.8, and 3.9. The average value of acceleration at a particular location is calculated by taking the summation of the accelerations at each time instant and dividing by the number of output points (n) for each curve.

$$Avg(x) = \frac{\sum_{i=1}^n x_i}{n} \quad (3.5)$$

The values recorded at each location are shown in the Table 3.1 for the original design. The value in the last row in the table i.e. mean of the averages indicates the average of average accelerations at the three critical locations. These results show that these values are high and should be reduced to ensure survivability of occupants and to avoid damage of sensitive electronic equipment.

Table 3.1 Results for Model 1

Maximum acceleration (m/s ²)	commander	4789
	driver	16480
	instrumentation panel	11965
Average acceleration (m/s ²)	commander	1148
	driver	2650
	instrumentation panel	1149
Mean of the averages (m/s ²)	1649	

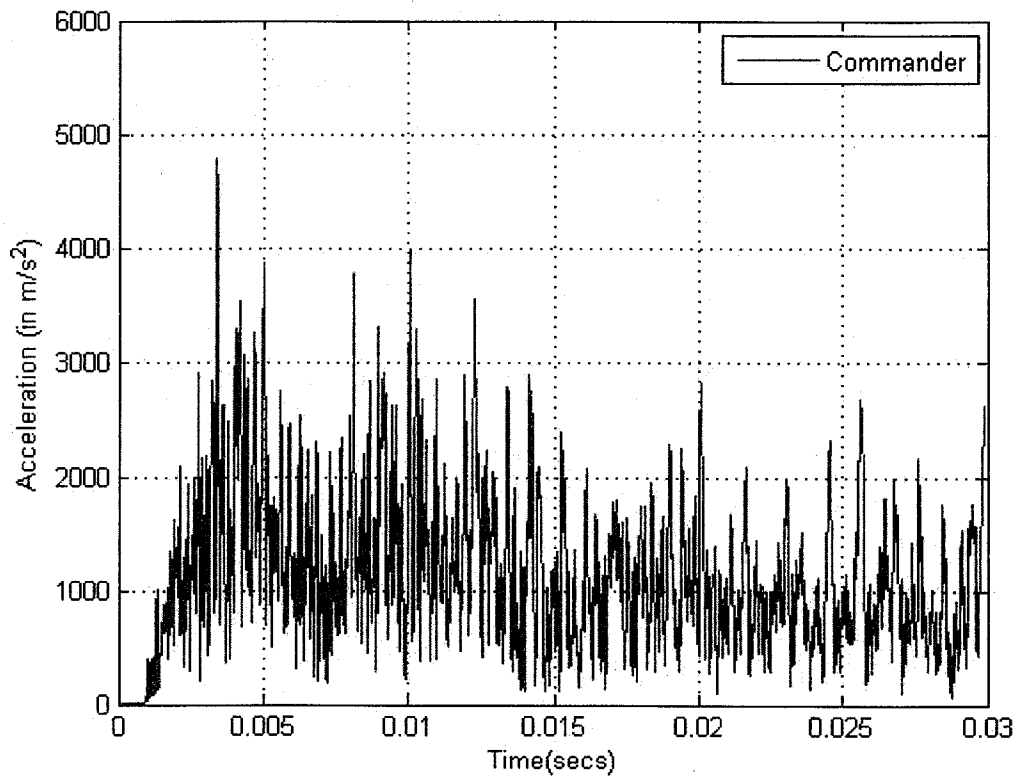


Figure 3.7 Acceleration Curves for Commander Location

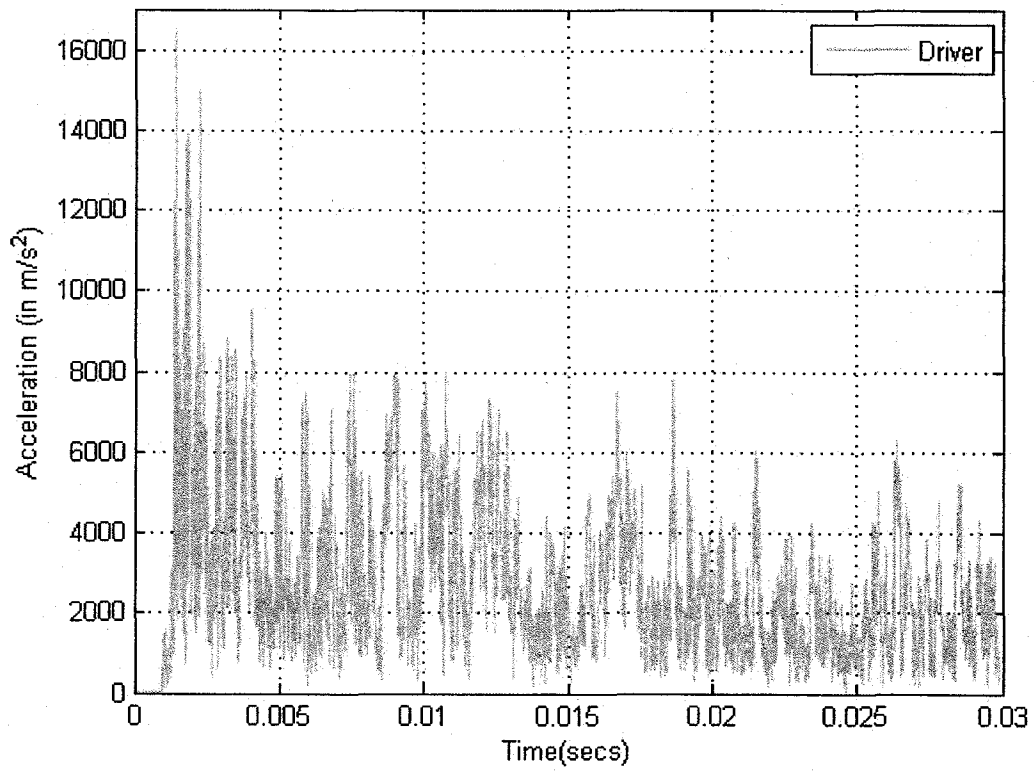


Figure 3.8 Acceleration Curves for Driver Location

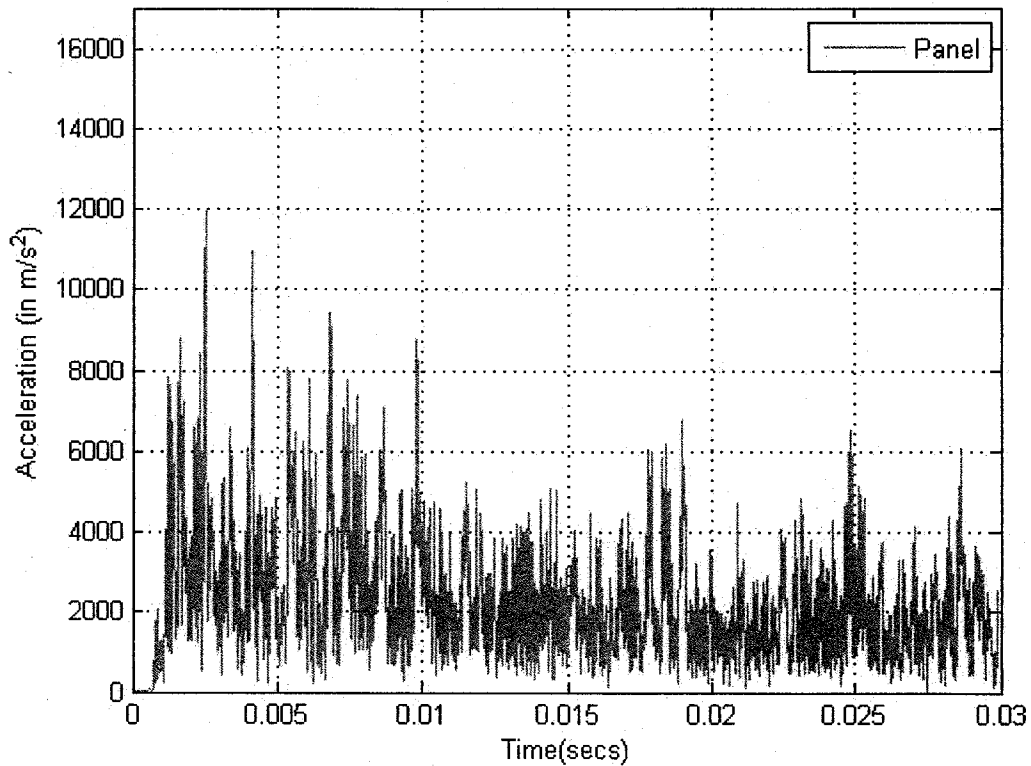


Figure 3.9 Acceleration Curves for Panel Location

To assess the effects of blast load on the overall vehicle structure, it is important to understand the way shock is propagating through it. Pressure contour plots, Figure 3.10 can be used to better understand shock propagation. While the maximum pressure occurs at the bottom panel, significant pressure is observed throughout the vehicle.

Non-linear structural response can be gauged by means of parameters like displacements and stresses. These parameters provide better understanding of the vehicle behavior under these highly transient events. Displacement contours are shown in the Figure 3.12. von Mises stress value is used for stress calculations since it can be used to

indicate failure. The yield strength value for the vehicle material (Aluminum – Al 7039 T64) is 380 MPa. When von Mises stresses in the model exceed this value, there would be plastic deformation in the structure. Hence, effective shock absorption can take place when the structure is plastically deformed. Figures 3.11 shows the von Mises stress contours. The maximum von Mises stress in the vehicle is 61MPa, which is significantly below the yield stress value of the material. Hence there is no plastic deformation and this can be confirmed from the plastic strain contours in Figure 3.13 which shows zero value through out the vehicle model. The reason for zero plastic deformation can be attributed to the fact that the blast load of 0.5 Kg is significantly low to deform the structure plastically. However, even at this load the acceleration values at the critical locations are significantly high. In order to reduce the shock at these locations other means need to be pursued.

In this work, shock reduction by joint design approach is considered. In what will be described later, attaching a joint attached to the bottom panel and the rest of the vehicle is considered to introduce geometric non-linearity. Due to this, the propagation of shock is disrupted, and reflected to some extent, before it reaches to the critical areas in the vehicle.



Figure 3.10 Pressure Contours for Model 1 at 30 ms

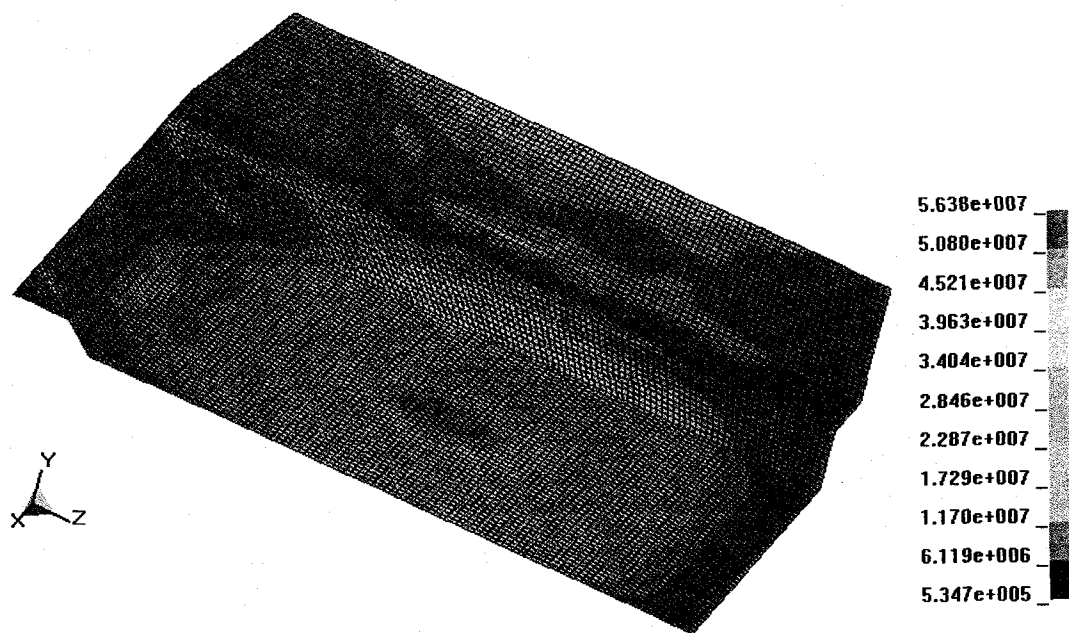


Figure 3.11 von Mises Stress Contours for Model 1 at 30 ms



Figure 3.12 Displacement Contours for Model 1 at 30 ms

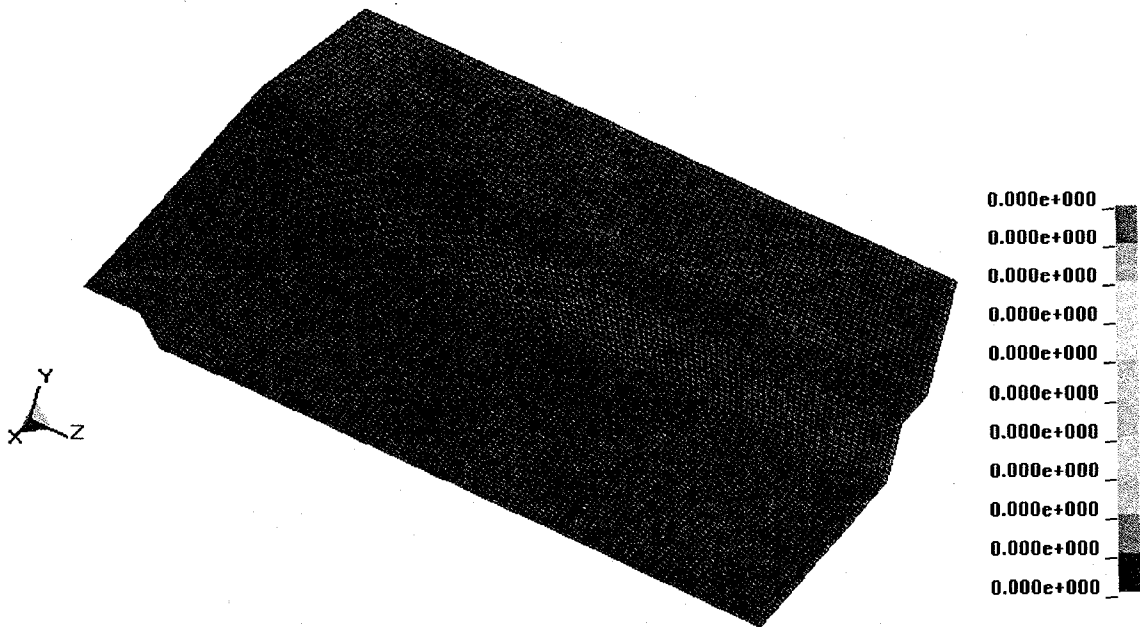


Figure 3.13 Plastic Strain Contours for Model 1

3.3 Model 2

3.3.1 Steps for Finite Element Analysis

Model 2 represents the main model for studying the shock transmission across the IS-ATD vehicle due to a projectile impact. The steps in creating the finite element analysis of this model are described below:

- Step I: Create the geometry using HyperMesh preprocessor.
- Step II: Define material properties, meshing, boundary conditions, contacts between different sub-assemblies and application of appropriate loading condition that can simulate the mine blast.
- Step III: Solve the model using the explicit finite element code LS-DYNA.
- Step IV: Post-process results using LS-POST or HyperView.

3.3.2 Modeling

The finite element model of the AX-1 model is created using HyperMesh Preprocessor. The geometry of the entire vehicle is created by entering the key point locations specified in Table 2.3. These key points are joined to obtain lines. These lines are then used to create the beam elements. In this model, 3D beam elements have been used to construct the entire frame structure. The explanation for creating 3D beam elements is provided in the section 3.3.3.1. Similarly to create the armor, initially key points, then lines and areas are used to obtain the rectangular, trapezoidal or circular areas according to the geometry of the AX-1 model. However, in order to account for the shell and beam thickness', the areas created are placed at an offset distance equal to half the shell and beam thickness. The created geometry is shown in Figure 3.14 while the frame is shown in Figure 3.15.

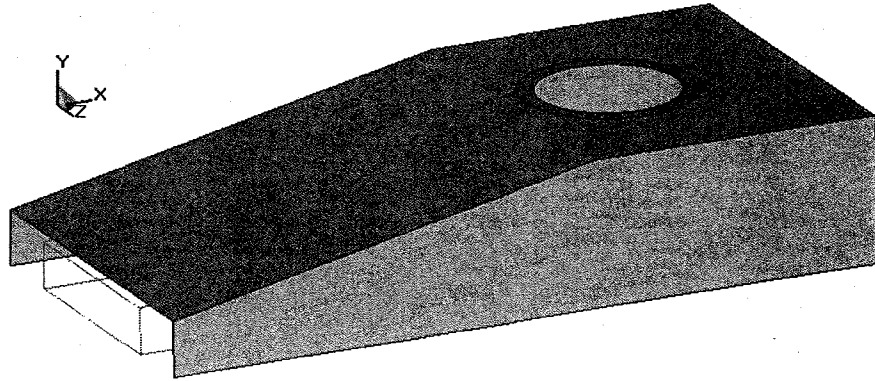


Figure 3.14: AX-1 Model

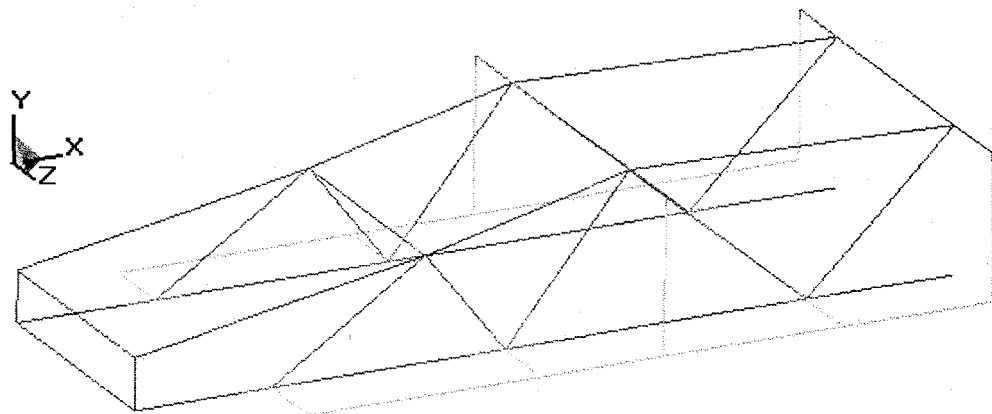


Figure 3.15: Frame of AX-1 Model

3.3.3 Meshing

The areas representing the armor are meshed using shell elements. Shell elements have been used to reduce computational time when compared to solid elements. Similar

mesh parameters as used in Model 1 are applied to Model 2. The meshed model is shown in the Figures 3.16. Since the space frame cannot be viewed completely in Figure 3.16, a separate figure is shown in Figure 3.17 removing the armor areas. To mesh the frame, 3D beam elements are used. Various boundary conditions, contact definitions, loading conditions and different LS-DYNA cards used for creating the input file of the finite element model are described in the subsequent sections.

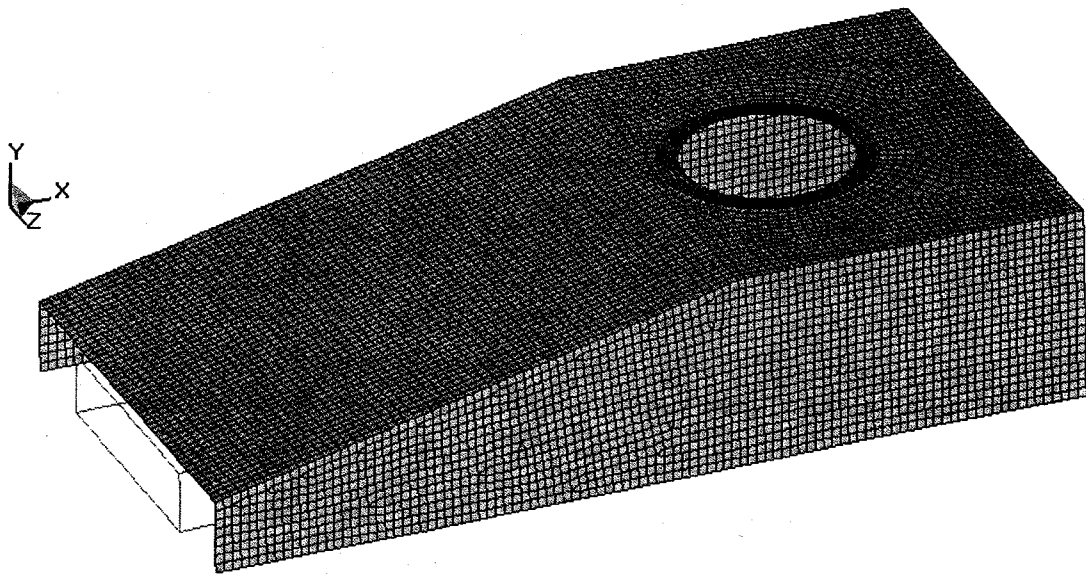


Figure 3.16: Meshed AX-1 Model

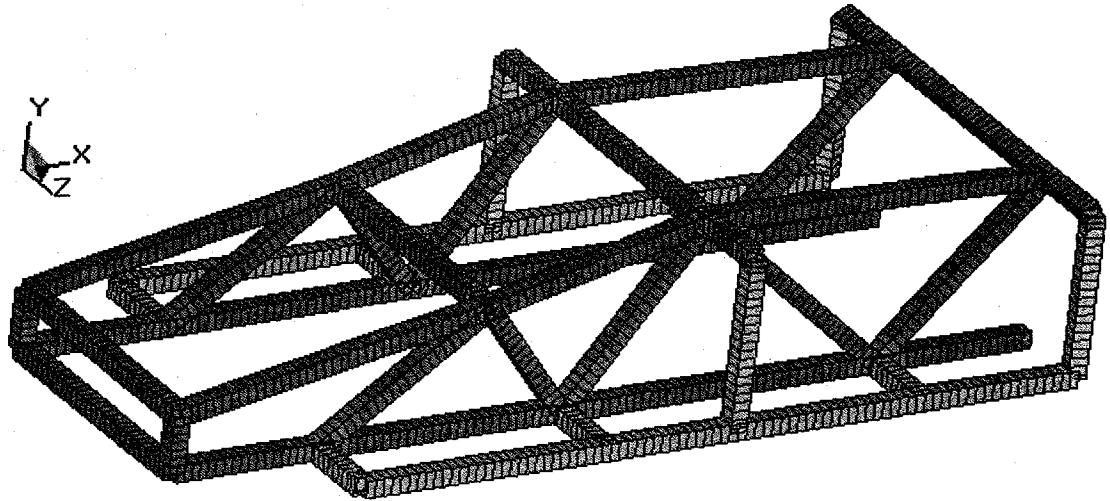


Figure 3.17: Mesh of the Space Frame in AX-1 Model

3.3.3.1 Modeling 3D Beam Elements

As described earlier, the whole frame structure is created in the form of lines. However, different segments within the space frame structure possess different orientations. To ensure that each cross section is defined such that it is perpendicular to the axis of each segment, a separate node, known as orientation node is defined for each segment. If the beam is curved, each and every element in the structure must have a separate orientation node so that the orientation of cross-section is perpendicular to any given element. Figure 3.18 shows the definition of beam elements in LS-DYNA. The beginning and end of the element are defined using nodes n1 and n2. Node n3 is added to create a plane (r-s plane) along with nodes n1 and n2 that is normal to the cross section of the element (s-t plane). From the Figure 3.18, we see that since n3 is defined in the r-s plane, the cross section of the beam element is oriented along the s-t plane.

Since the geometry of the space frame is defined by lines, single orientation node can be used to define 3D beam elements along that line. An example for one segment of the space frame is shown in the Figure 3.19 where a segment AB with tubular cross section uses single orientation node, C for all the elements.

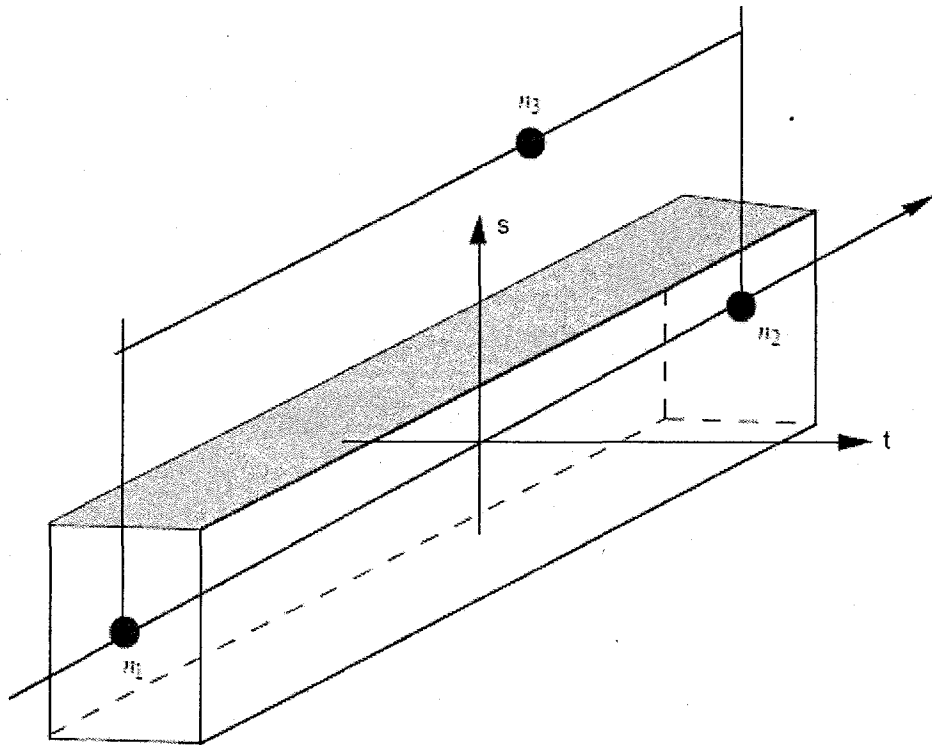


Figure 3.18: Defining the Beam Element

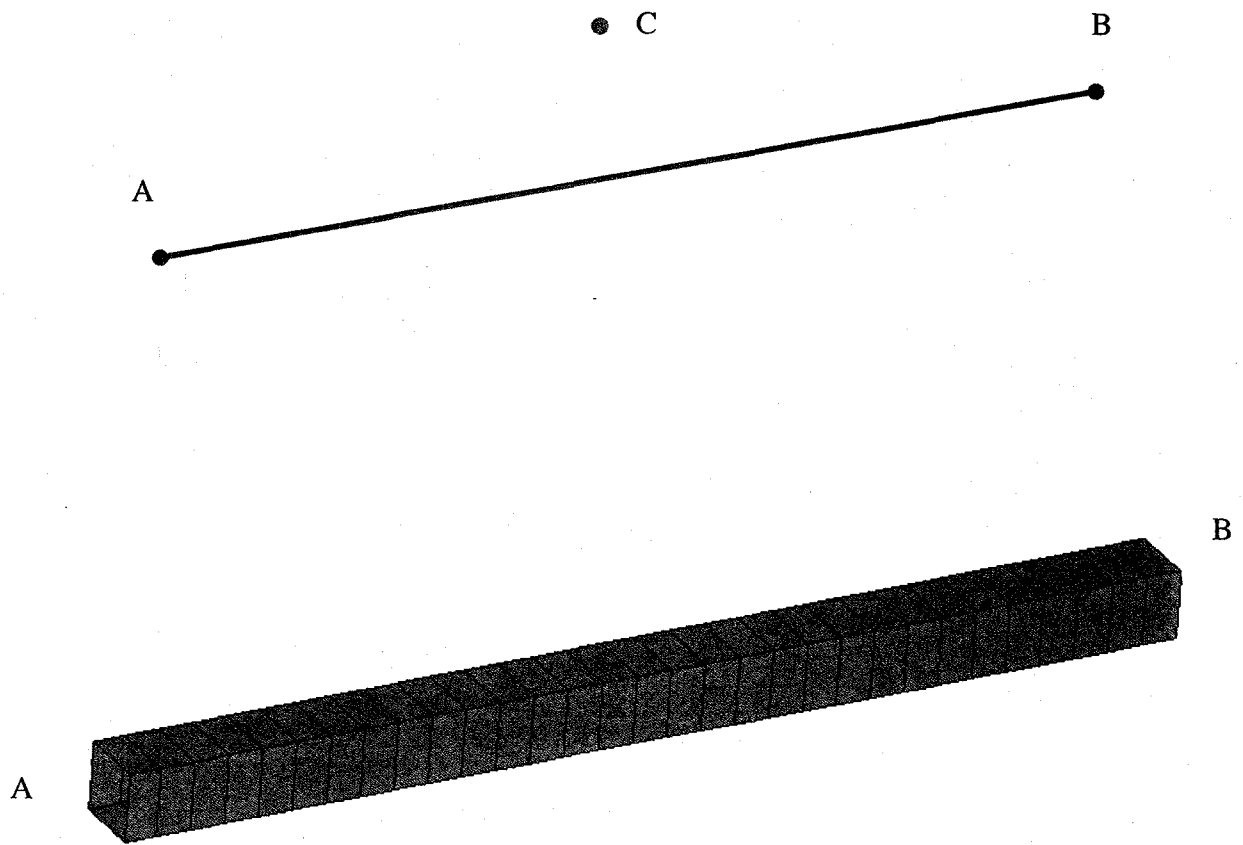


Figure 3.19: Example for Generating Beam Elements with Single Orientation Node

3.3.4 Defining 3D Beam Elements in LS-DYNA

For example, as shown below, a beam element with ID (EID) 1, is defined by start and end nodes N1 and N2 with N3 being the orientation node. Here PID stands for the part Id.

```
*ELEMENT_BEAM
$>>>>EID>>>>PID>>>>N1>>>>N2>>>>N3
      1      1      1      3      12
      2      1      3      4      13
      3      1      4      5      14
```

To define the cross-section parameters, *SECTION_BEAM card is used. A sample is shown below. The various parameters are described below.

```
*SECTION_BEAM
$>>>>SID>>>>ELFORM>>>SHRF>>>QR/IRID>>>>CST
      9      1      1.0      -5      2.0
$>>>>TS1>>>>TS2>>>>TT1>>>>TT2>>>>
      0.05715      0.05715      0.05715      0.05715

*INTEGRATION_BEAM
$>>>>IRID>>>>NIP>>>>RA>>>>ICST
      5      0      0.0000      3
$>>>>W>>>>TF>>>>D>>>>TW
      0.05715      0.01588      0.05715      0.01588
```

- SID- Section ID
- ELFORM- Element formulation with 1 indicates Hughes-Liu element formulation with cross section integration has been used.
- SHRF- Shear Factor
- QR/IRID- Integration Rule, negative value indicates that user defined integration rule has been used. User defined integration rule is defined using the card *INTEGRATION_BEAM. Absolute value of IRID is used to refer it in this card.
- TS1- Beam thickness in s-direction at node n1
- TS2- Beam thickness in s-direction at node n2
- TT1- Beam thickness in t-direction at node n1
- TT2- Beam thickness in T-direction at node n2
- NIP – Number of integration points
- RA - Relative area of cross section.
- ICST- Standard CS type.[2- C section, 3-Angle section, 5-Rectangular tubing]

- W, TF, D, TW- Parameters for the cross section. These are defined as described in the section.

3.3.4 Contact Definitions

The AX-1 model has several snap joints that are used to connect the armor with the frame. Several contact definitions that are available in LS-DYNA are used to represent these joints.

- To represent the joints connecting the frame and the armor, *CONTACT_AUTOMATIC_TIED_NODES_TO_SURFACE, contact definition is used. A set of four elements on the armor are used to tie with the corresponding beam location in the frame. This is shown in Figure 3.21, which gives an enlarged image of the zooming window used in Figure 3.20.
- To represent the surface contact between the armor and the frame members, a *CONTACT_AUTOMATIC_NODES_TO_SURFACE card definition is used. A band of elements on the armor are used to contact with the corresponding frame elements as shown in Figure 3.21. All the red colored joints shown in the Figure 3.17 are connected using the contact definition card *CONTACT_AUTOMATIC_TIED_NODES_TO_SURFACE card and the places where the frame elements contact the armor are connected using the card *CONTACT_AUTOMATIC_NODES_TO_SURFACE card.

In this way for the whole AX-1 model, 16 tied contacts and 14 surface contacts with the frame members. The complete finite element model with contacts and no boundary conditions is shown in the Figure 3.22.

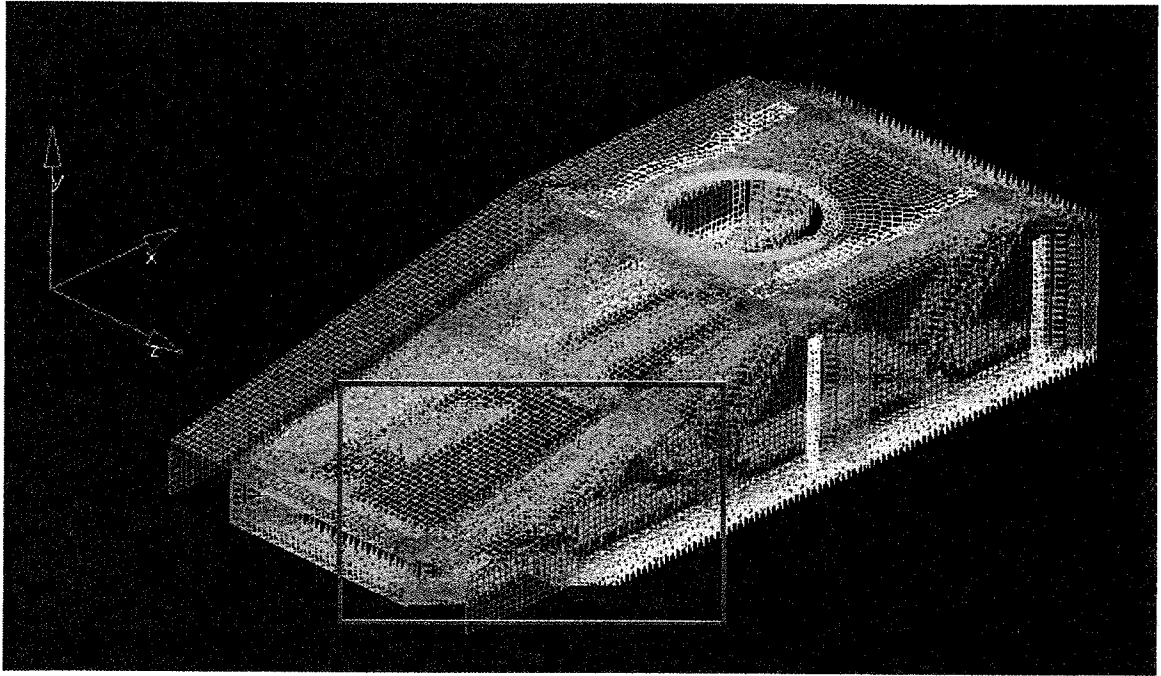


Figure 3.20: AX-1 Model from ARL

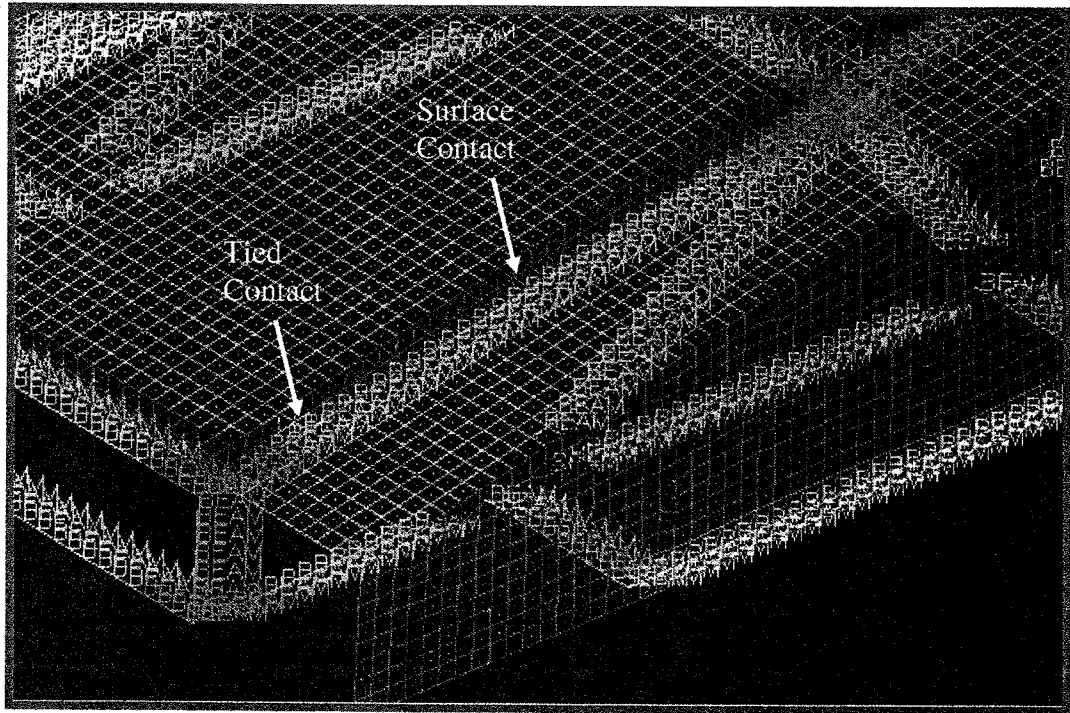


Figure 3.21: Zoom Window Details of FE Model in Figure 3.17.

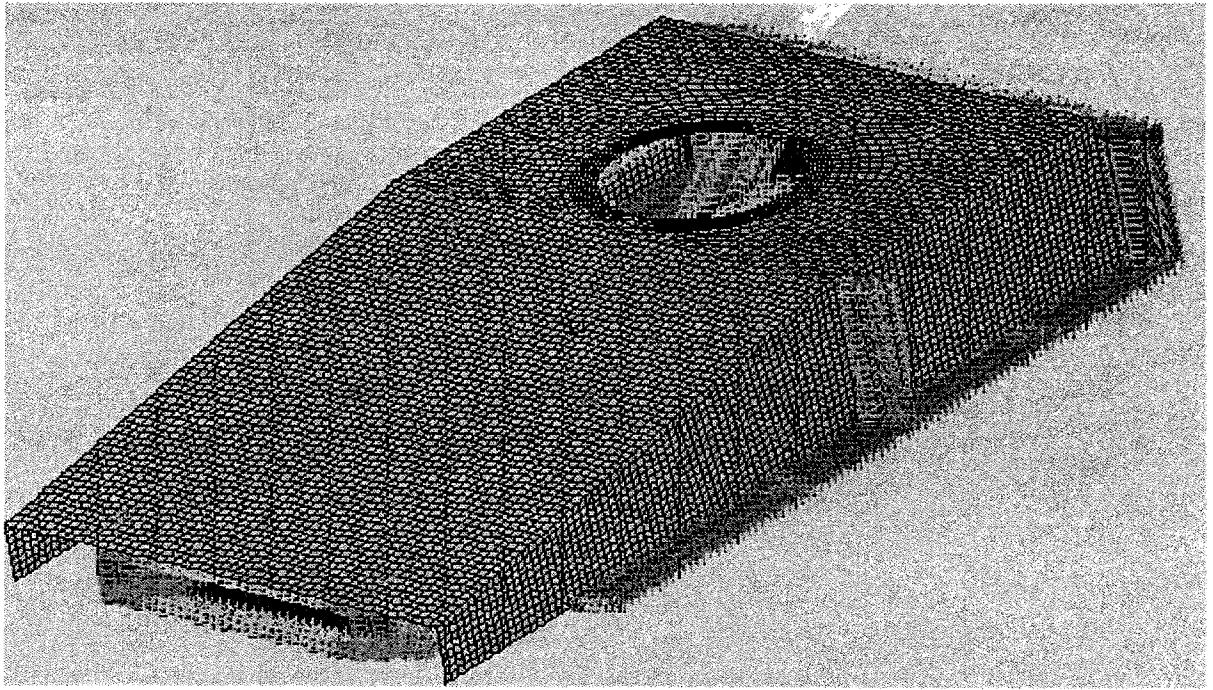


Figure 3.22: FE Model of AX-1

3.3.5 Boundary Conditions

The AX-1 frame (no armor) has structurally tested under static loading conditions at the University of Delaware- Center for Composite Materials (UD-CCM) facility. The structure is mounted and to be tested in the upright position. To meet this requirement in the FE model, corresponding nodes confirming to these locations on the back end of the frame and the armor are fixed not allowing motion in any direction. The FE model with contacts and boundary condition is shown in the Figure 3.22.

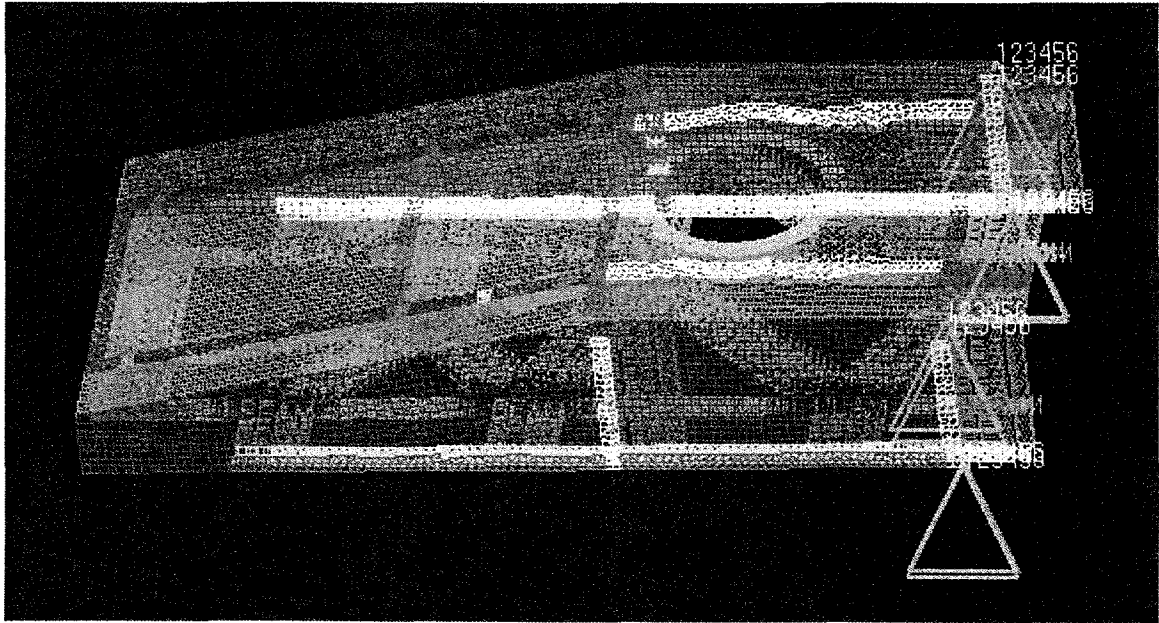


Figure 3.23: FE Model with Boundary Conditions

3.3.6 Loading Conditions

In this study, two load locations are chosen. The first load case corresponds to the impact on the side wall of the AX-1 model (shown in Figure 3.24) while the second load case corresponds to the impact at the front panel as shown in the Figure 3.25. The impulse curves used for these models are shown in Figures 3.26, 3.27. In order to observe the behavior of the model under varying loads, a parametric study is conducted on both load cases. A 50 KN incremental load has been used for the study. The values of 1200KN and 200 KN as shown in the impulse curves are chosen due to the fact that the

model at these load values does not undergo permanent deformation and the plastic strain value lies below the failure strain value.

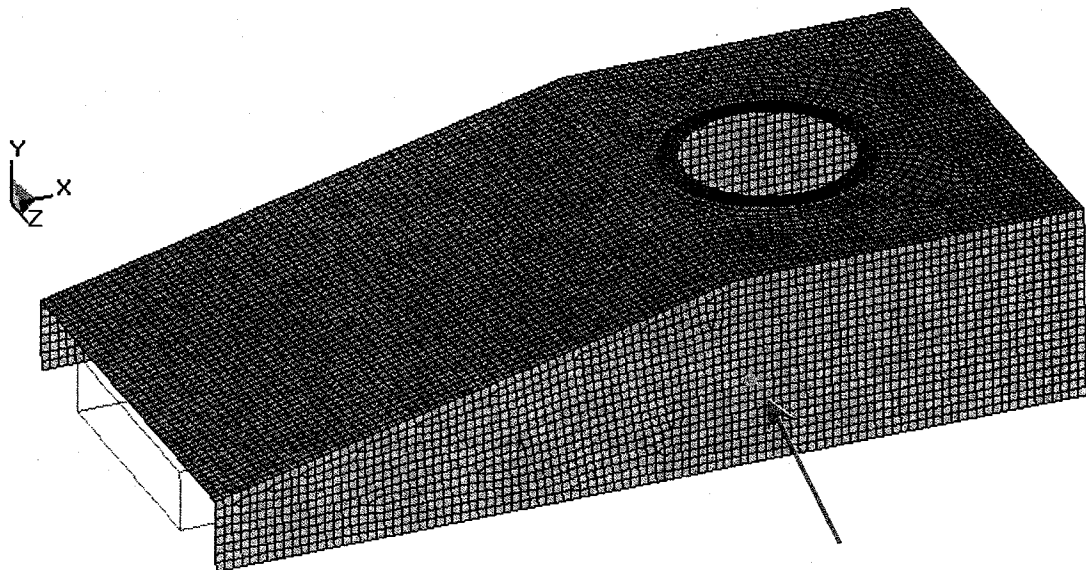


Figure 3.24: Load Case #1

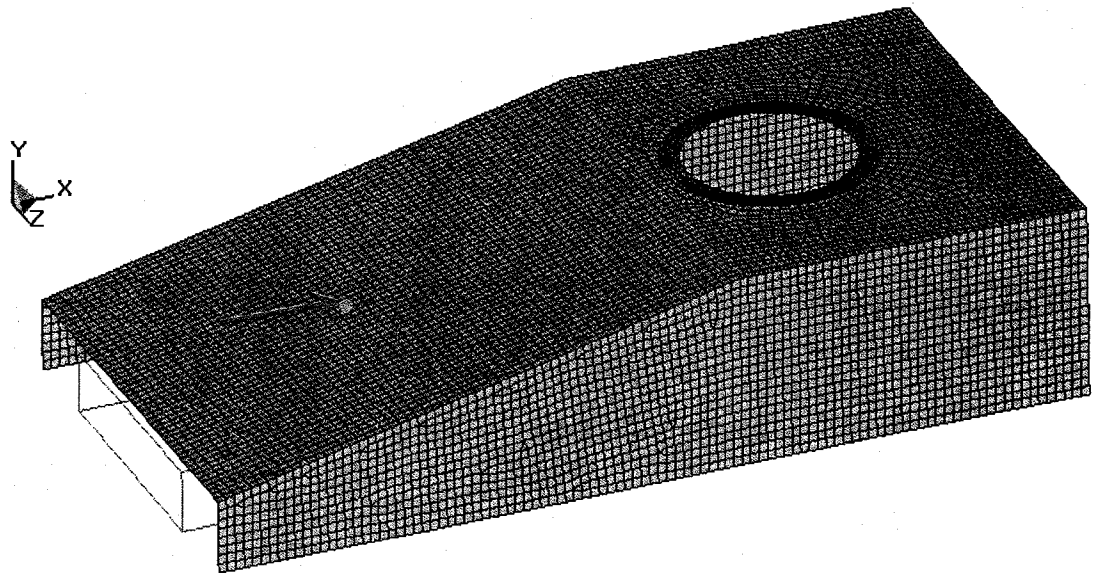


Figure 3.25: Load Case #2

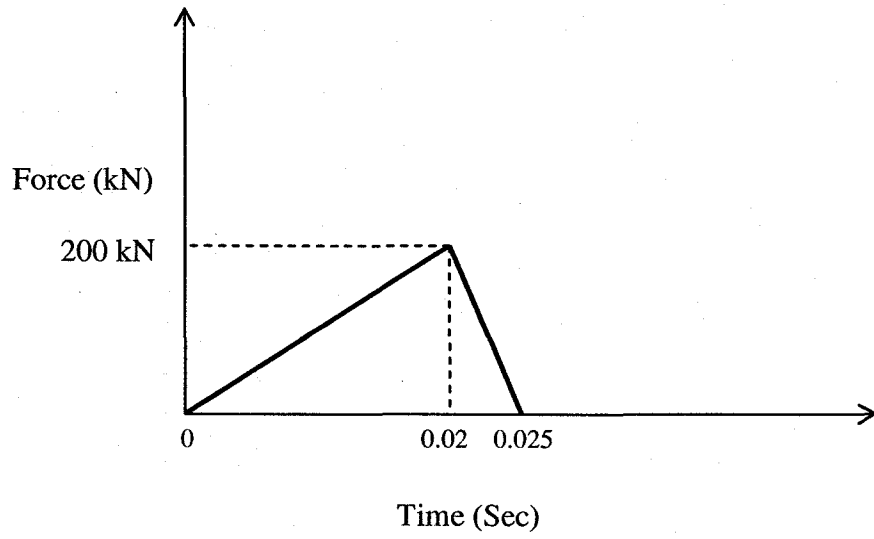


Figure 3.26: Load Curve for Load Case #1

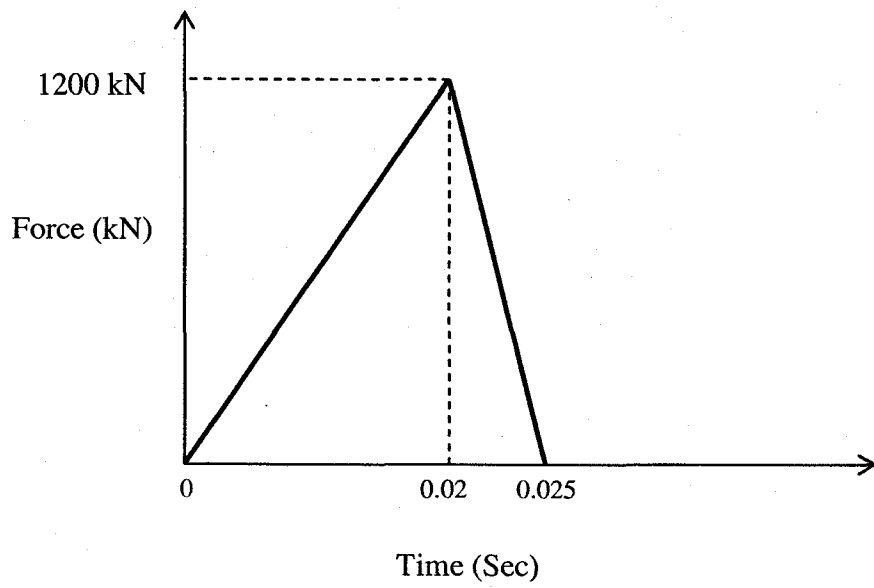


Figure 3.27: Load Curve for Load Case #2

3.3.7 LS-DYNA cards

3.3.7.1 Control Card

The detail of this card has already been explained in the Model 1. However, for the Model 2 ENDTIME is given as 0.025 s. A sample control card used is shown below.

```
*CONTROL_TERMINATION
$$ ENDTIM   ENDCYC   DTMIN   ENDENG   ENDMAS
    0.025    0        0.0     0.0     0.0

*CONTROL_TIMESTEP
$$ DTINIT   TSSFAC   ISDO    TSLIMIT  DT2MS    LCTM    ERODE    MSIST
    0.0      0.9      0        0.0     0.0

*CONTROL_SHELL
$$ WRPANG   ESORT     IRNXX   ISTUPD   THEORY   BWC     MITER    PROJ
    20.0     1         -1      1        2        2       1

*CONTROL_ENERGY
$$ HGEN     RWEN     SLNTEN  RYLEN
    2        2        2        2
```

3.3.7.2 Database Card

The database card used for this model is shown below.

```
*DATABASE_BINARY_D3PLOT
$$ DT/CYCL   LCDT
    0.0025
    0
```

3.3.7.3 Nodout Card

The nodout card used for this model is shown below.

```
*DATABASE_NODOUT
25E-04
```

3.3.7.4 Material Card

For both the armor and the frame similar material model as described in Model 1 are used.

3.4 Results

Some of the important parameters used for both loading case are listed below.

- LS-DYNA Solver (Version 970) is used with Double Precision.
- Analysis termination time = 0.025 sec.

3.4.1 Results for Load Case #1

Load case # 1 corresponds to the projectile impacting the side wall of the armor as shown in Figure 3.24. To understand the flow of shock through the model, displacement contours are observed and shown in Figures 3.28 and 3.29. We observe that shock transmits through majority of the structure even though the impact is locally concentrated on the side wall. To understand the effect of this impact load on the material, von Mises stress contours are used. These are shown in the Figure 3.30. It can be seen that the maximum stress on the armor occurs near the boundary condition location with an approximate value of 239 MPa. The yield stress value for the material of the armor and the frame is 380 MPa. Hence there is no plastic deformation in the armor due to this loading. However, plastic strain contours (Figure 3.31) on the frame suggest that there is a plastic strain of around 7% which is below the failure value of 13%. Any increase in load may result in the damage of the frame which is undesirable. These results also suggest that majority of the load is taken by the frame members.

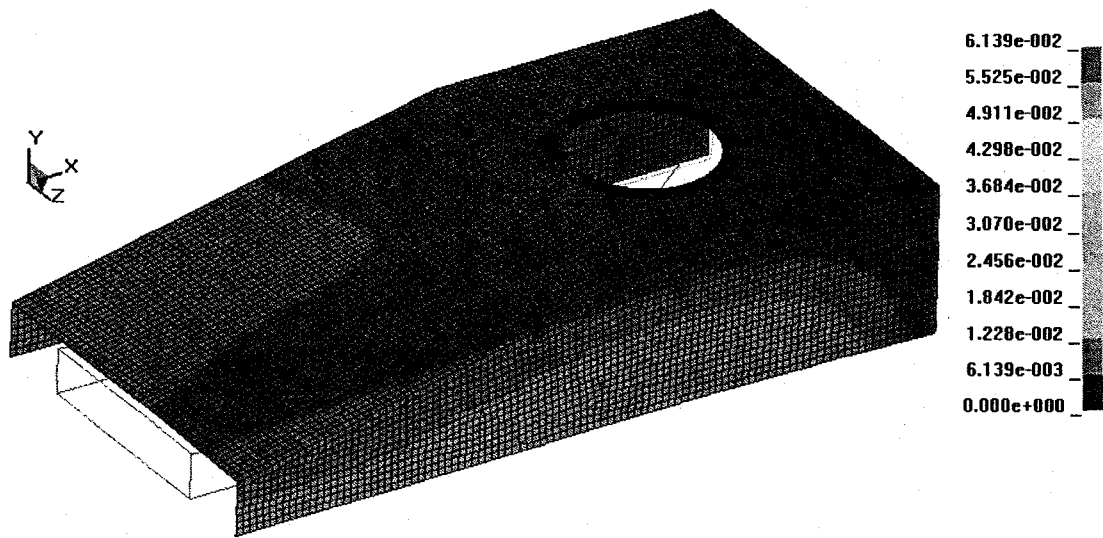


Figure 3.28: Displacement Contours for Load Case #1 at 25ms

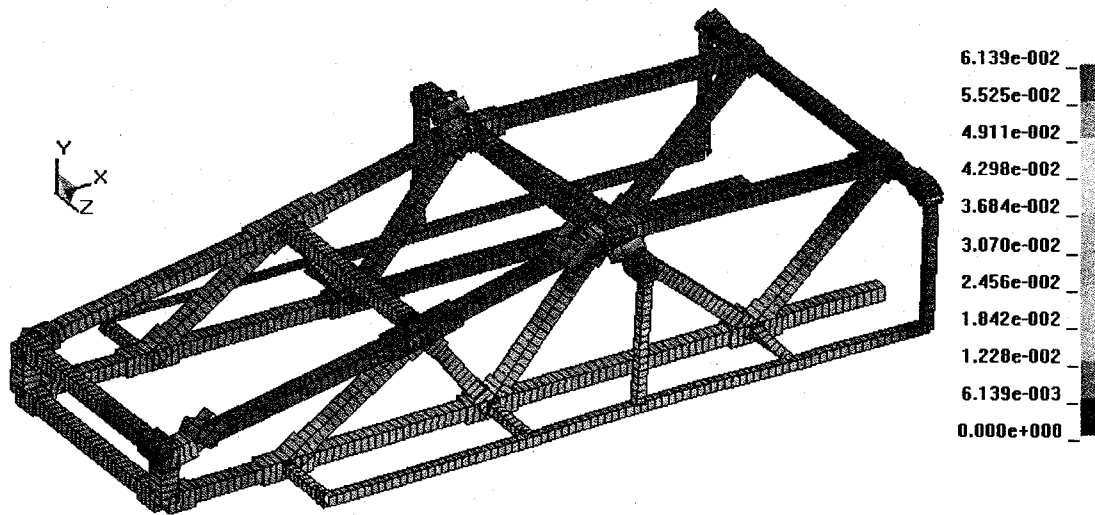


Figure 3.29: Displacement Contours of Frame for Load Case #1 at 25ms

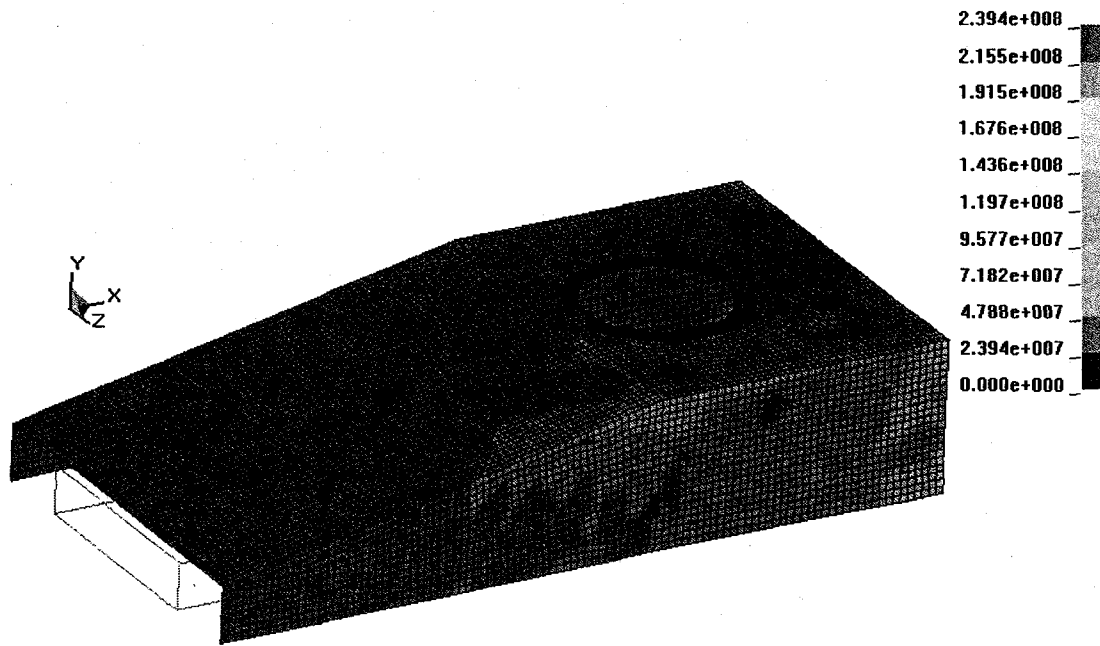


Figure 3.30: von Mises Stress Contours for Load Case #1 at 25ms

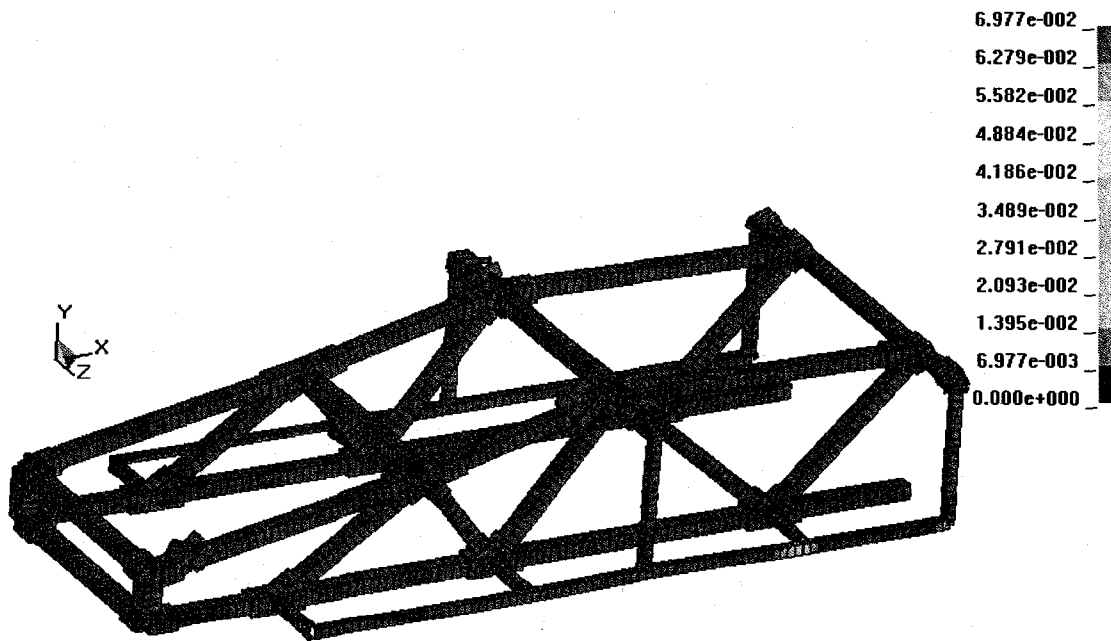


Figure 3.31: Plastic Strain Contours for Frame with Load Case #1 at 25ms

3.4.2 Results for Load Case # 2

Load case # 2 corresponds to the projectile impacting on the frontal portion of the armor as shown in Figure 3.25. The displacement contours on the armor and the frame are shown in Figure 3.32 and Figure 3.33 respectively. The Figures indicate that the shock propagation is more pronounced in this case. This is due to the fact that the applied load is higher and the von Mises stress contours shown in Figure 3.34 reflect this. Maximum stress of 417 MPa occurs at the location of applied load, which is higher than the yield stress value of 380 MPa for the material of the armor. Hence there is plastic deformation at this location and this is reiterated from the plastic strain contours of Figure 3.35. The maximum plastic strain is around 7% which is less than the failure strain value (13%) of the material. To see that if there is any plastic deformation in the frame members, plastic strain contours (shown in Figure 3.36) are observed. We see that almost negligible plastic strain occurs in these members. The maximum plastic strain at the load location is expected since there are no direct frame members in contact with the armor at this location.

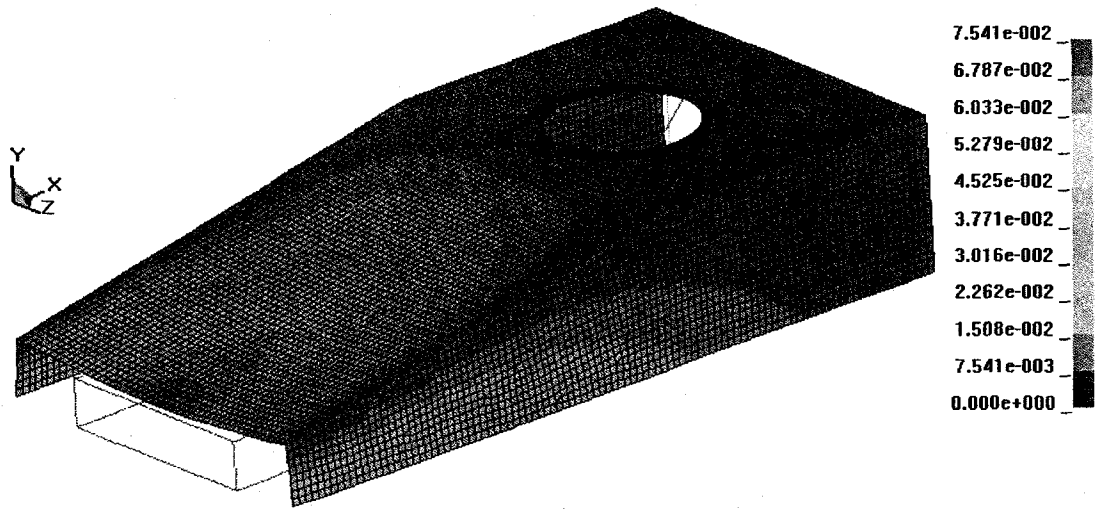


Figure 3.32: Displacement Contours for Load Case #2 at 25ms

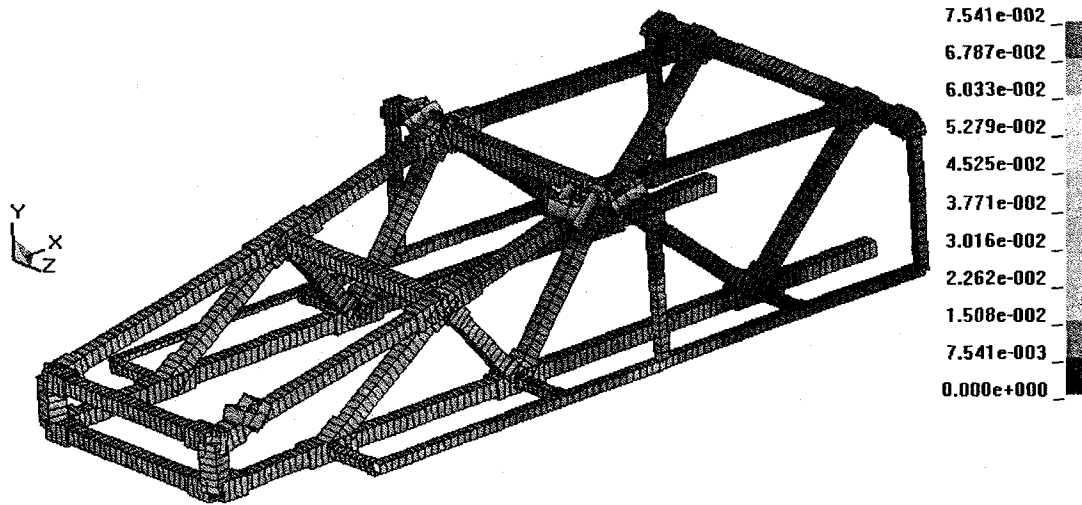


Figure 3.33: Displacement Contours of Frame for Load Case #2 at 25ms

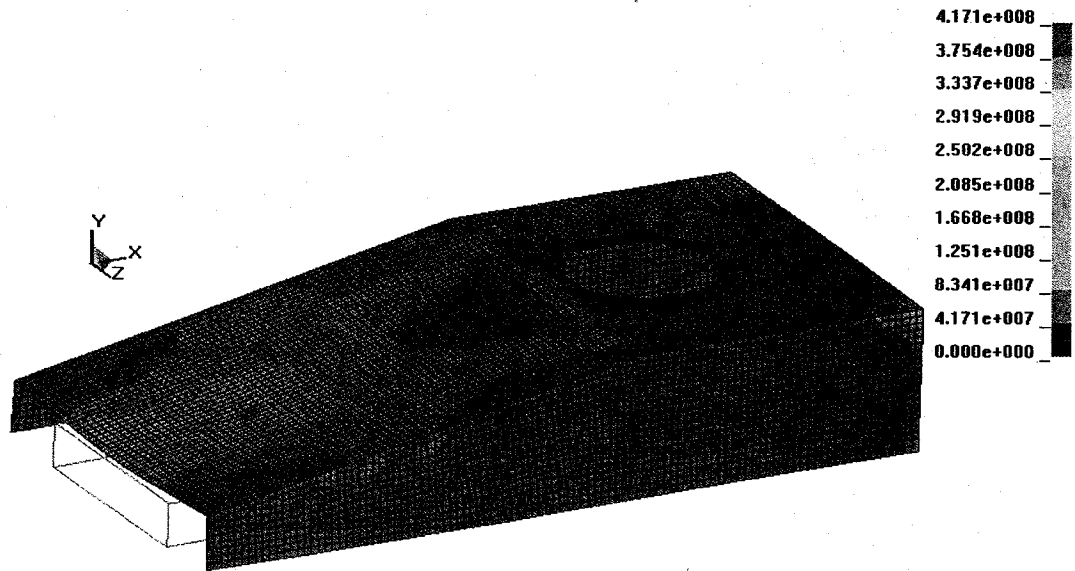


Figure 3.34: von Mises Stress Contours for Load Case#2 at 25ms

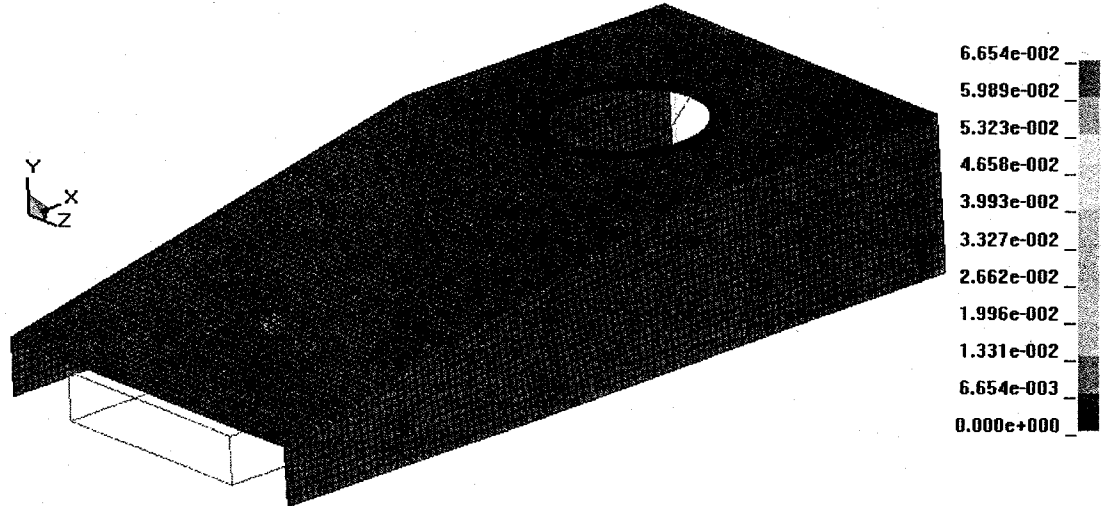


Figure 3.35: Plastic Strain Contours with Load Case#2 at 25ms

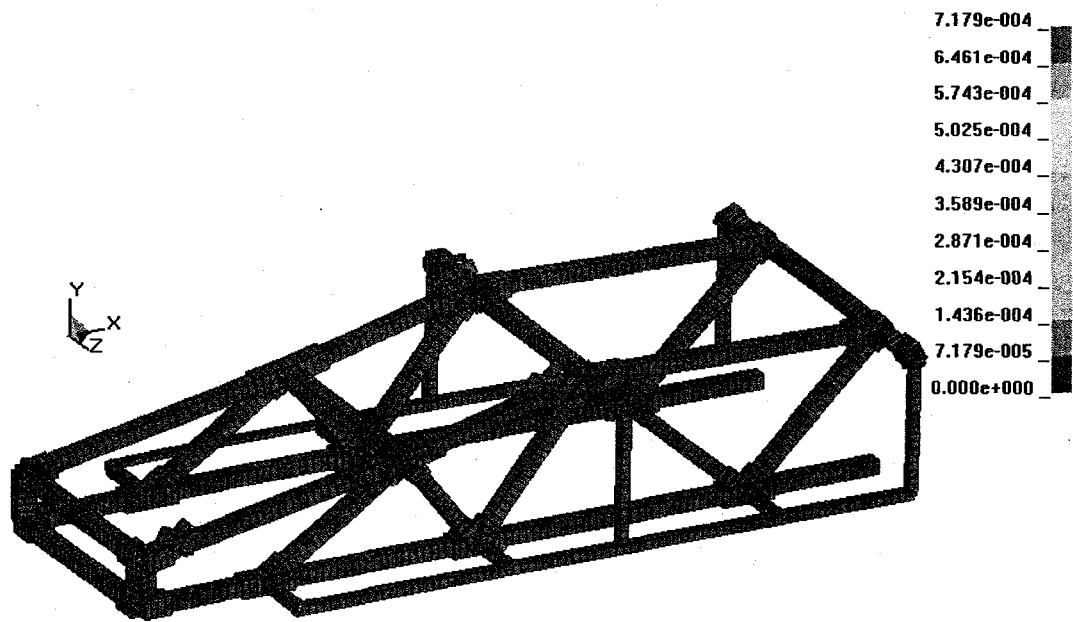


Figure 3.36: Plastic Strain Contours for Frame with Load Case#2 at 25ms

3.4.3 Effect of Joint Stiffness

Joints at eight nodal locations are chosen to examine the effect of stiffness of the joints on the overall structural response of the model. These nodes are selected as they represent majority of the joints in the model and also they are in close vicinity to the applied load cases. The first four nodes are 1, 8, 18, 17 as shown in Figure 2.10 and the other four nodes correspond to the symmetrical nodes of the first four nodes about the XY plane. The stiffness variation is performed by changing the lengths of the joints at the nodal locations. It is to be noted that no change in cross sectional properties of the joints is performed while changing the stiffness. Two stiffness cases are considered. The first case (case A) corresponds to smallest length of the joints. Length of each joint at the eight nodal locations in this case is approximately equal to 0.04 m. In the second case (case B), the lengths of the joints are increased to the maximum extent. However,

considering the real time application, the joint lengths are increased to be approximately around twice the lengths when compared with the of initial case. The details of the two cases are summarized below in the Table 3.2.

Table 3.2 Stiffness Variation Details for Model 2

Case #	Approximate Length of Each Joint (m)	Mass of Joints at Eight Nodal Locations (Kg)	% Change in Mass of Joints at Eight Nodal Locations with Initial Case
Case A	0.04	49.70	47% Decrease
Case B	Twice Initial Case	152.84	62% Increase

3.4.3.1 Results and Discussion

The nonlinear response of the model for the above two cases is considered for both the side impact load (Load Case #1) and front impact load (Load case # 2) cases. The displacement contours for the minimal stiffness case with Load Case # 2 are shown in the Figures 34 and 35. The displacement contours for the maximum stiffness case with Load Case # 2 is shown in the Figures 36 and 37. Comparing these results, we see that the displacement values in case A gives lesser values than the case B. For case A, the maximum displacement is 0.083 m and for the case B the value is 0.078. However, the propagation of shock is similar in both cases.

The displacement contours for the minimal stiffness case with Load Case # 1 is shown in the Figures 3.41 and Figure 3.42. The maximum displacement values for both loading cases and stiffness cases are summarized in Table 3.3. The displacement contours for the maximum stiffness case with Load Case # 1 is shown in the Figures 3.43 and Figure 3.44. Comparing these results, we see that the displacement values in the case A gives lesser values than the case B. For the minimum stiffness case, the maximum displacement is 0.061 m and for the maximum stiffness case the value is 0.063 m. This is

contrary to what is expected since a stiffer structure should give less displacement values. However, if we examine the results closely, we observe that in these cases, the location where the load is applied is not in the near vicinity of varying stiffness. The displacement contours for the minimal contours suggest that the propagation of shock extends far beyond the location where the load is applied. However, propagation of shock is limited towards the load application panel in the maximum stiffness case. Displacement contours on the frame members give a clear indication that the deformation occurs more locally at the point of application of load. The high stiffness location beyond this point ensures that shock is not propagated through the entire structure.

These results indicate that changing the stiffness can influence the overall behavior of the structure and a stiffer structure gives better response. However adding stiffness to the structure also increases its overall mass. Hence, there is a need to find an optimal stiffness for the structure without greatly increasing the mass.

Table 3.3 Displacement Results

Displacement Results in m	Load Case # 1	Load Case # 2
Case A	0.061	0.083
Case B	0.063	0.078

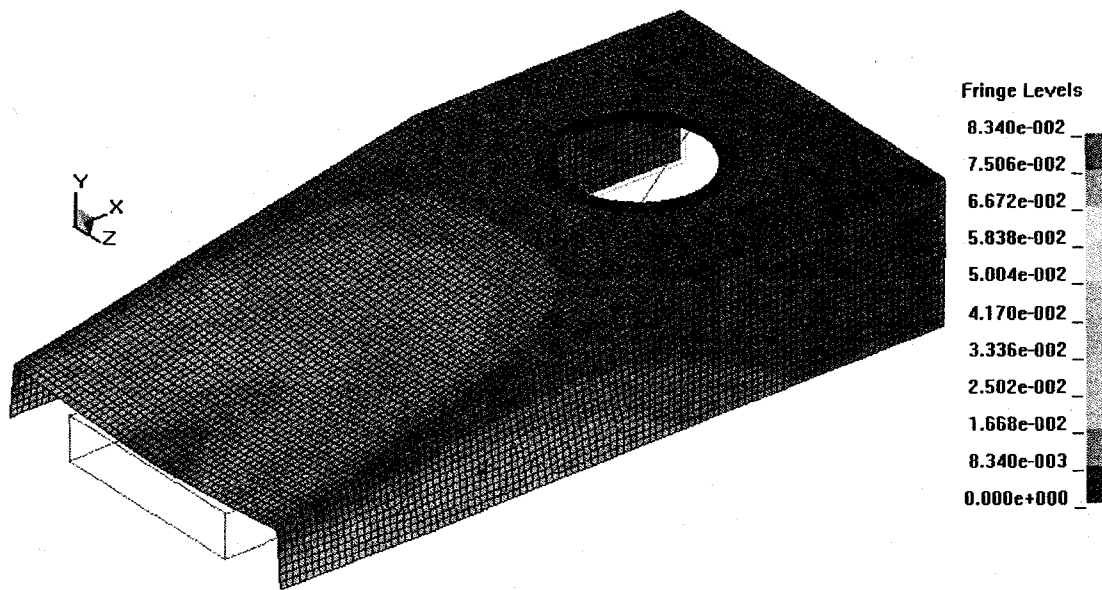


Figure 3.37: Displacement Contour for Case # 1 with Load Case # 2 at 25ms

Contour (Analysis system)
 Displacement (Mag)
 6.233E-02
 5.541E-02
 4.849E-02
 4.155E-02
 3.463E-02
 2.770E-02
 2.078E-02
 1.385E-02
 6.926E-03
 0.000E+00
 No result
 Max = 6.233E-02
 Min = 0.000E+00

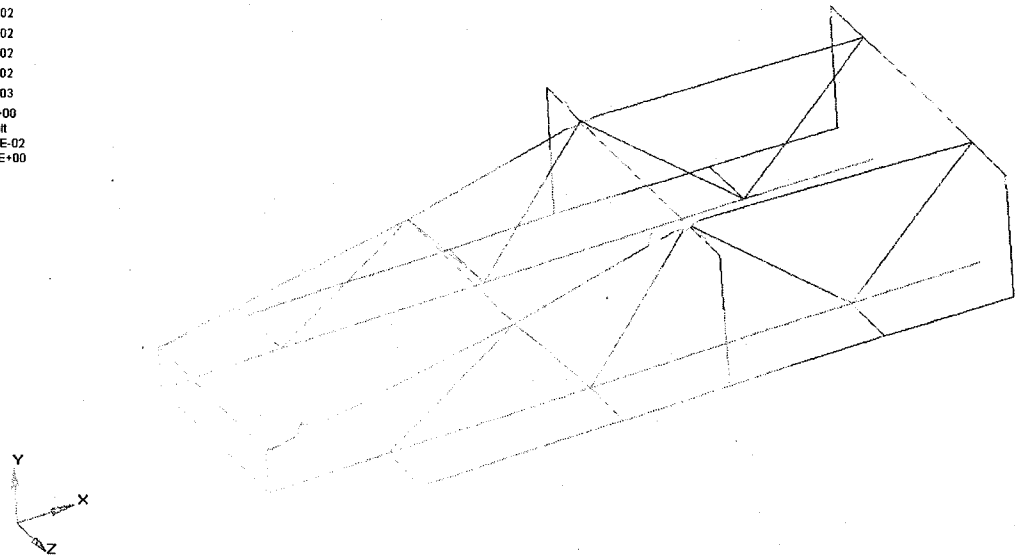


Figure 3.38: Displacement Contours of Frame for Case # 1 with Load Case # 2 at 25ms

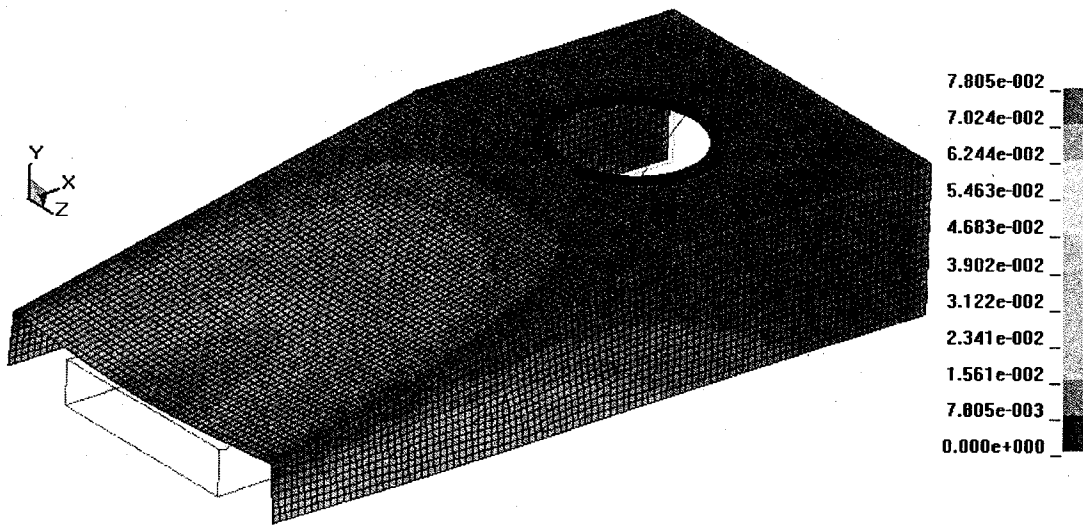


Figure 3.39: Displacement Contour for Case # 2 with Load Case # 2 at 25ms

Contour (Analysis system)
 Displacement (Mag)
 7.805E-02
 6.938E-02
 6.071E-02
 5.203E-02
 4.336E-02
 3.469E-02
 2.602E-02
 1.734E-02
 8.672E-03
 0.000E+00
 No result
 Max = 7.805E-02
 Min = 0.000E+00

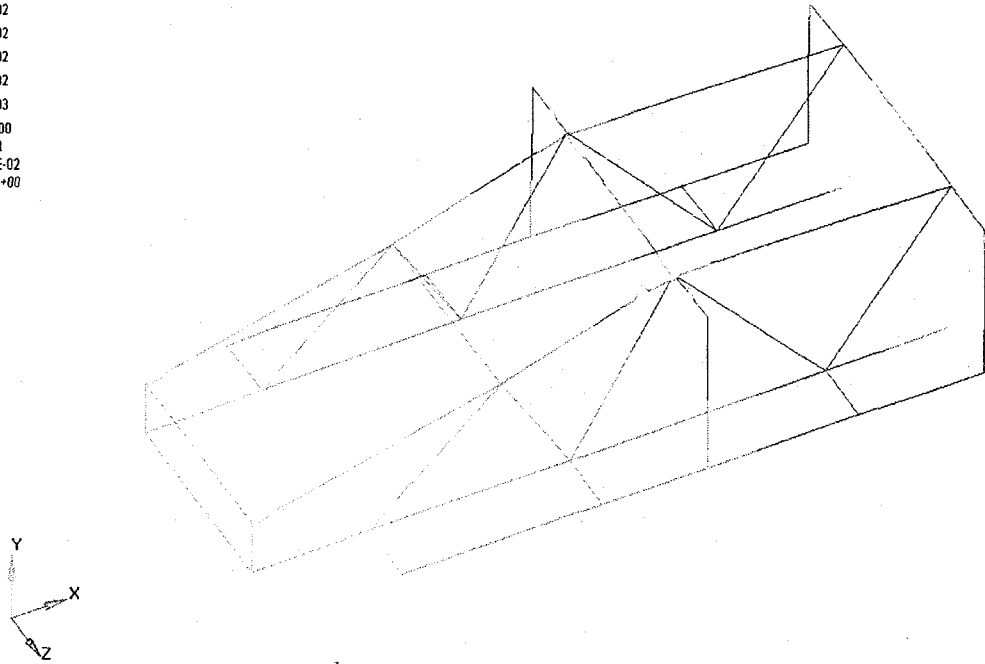


Figure 3.40: Displacement Contours of Frame for Case # 2 with Load Case # 2 at 25ms

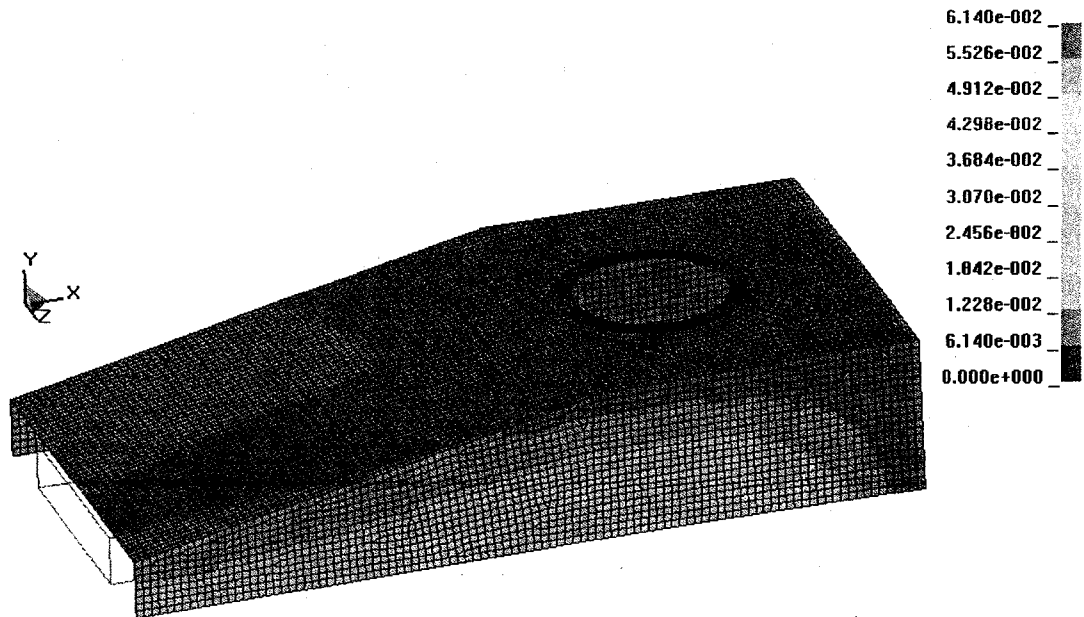


Figure 3.41: Displacement Contours of for Case # 1 with Load Case # 1 at 25ms

Contour (Analysis system)
Displacement (Mag)
6.279E-02
5.581E-02
4.883E-02
4.186E-02
3.488E-02
2.791E-02
2.093E-02
1.395E-02
6.976E-03
0.000E+00
No result
Max = 6.279E-02
Min = 0.000E+00

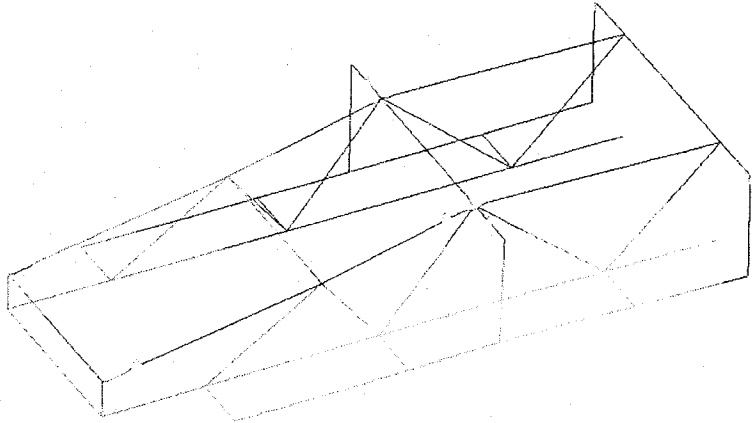


Figure 3.42: Displacement Contours of Frame for Case # 1 with Load Case # 1 at 25ms

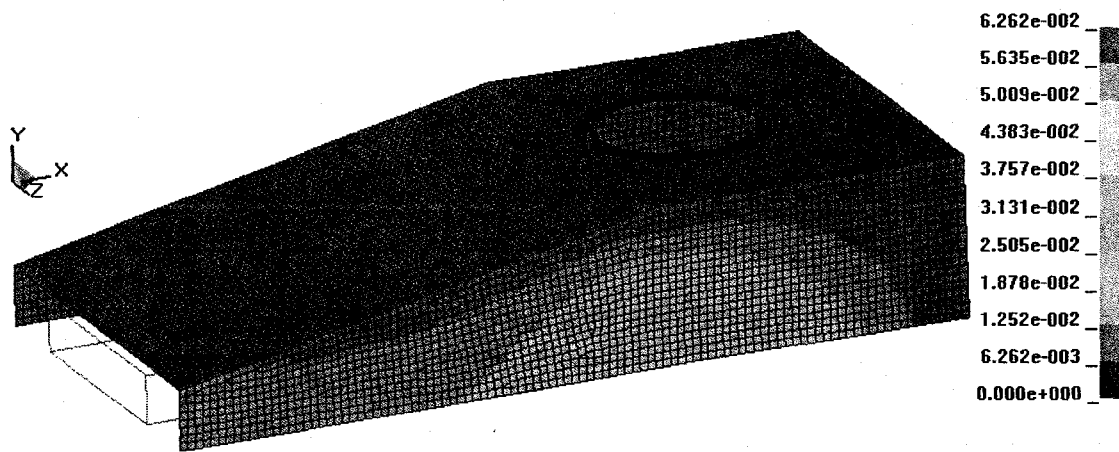


Figure 3.43: Displacement Contours of for Case # 2 with Load Case # 1 at 25ms

Contour (Analysis system)
Displacement (Mag)
6.262E-02
5.566E-02
4.870E-02
4.174E-02
3.479E-02
2.783E-02
2.087E-02
1.391E-02
6.957E-03
0.000E+00
No result
Max = 6.262E-02
Min = 0.000E+00

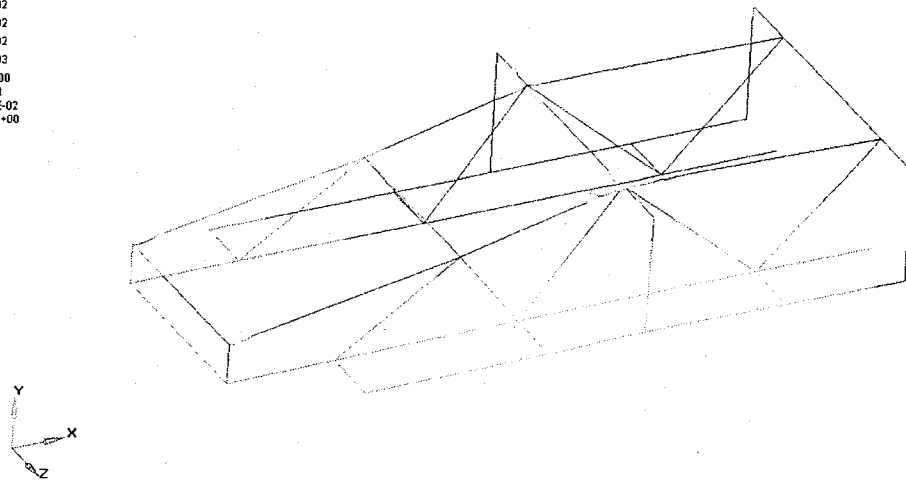


Figure 3.44: Displacement Contours of Frame for Case # 2 with Load Case # 1 at 25ms

CHAPTER 4

BOTTOM JOINT DESIGN AND OPTIMIZATION- MODEL 1

4.1 Joint Design for Shock Mitigation

Mine blast loading can cause significant damage to critical locations within the vehicle. A new joint design is proposed to reduce the shock at these locations. This joint design needs to meet the following requirements:

- Maximize energy absorption due to impact or blast loadings.
- Minimize propagation of shock from the directly affected region to the critical locations.
- Ease of assembly and disassembly.
- No permanent damage to the remainder of the vehicle beyond the directly affected part and the joint.

To satisfy the above requirements, an L-shaped bottom joint is proposed. A typical joint configuration, connecting the bottom panel to the rest of the vehicle, is shown in Figure 4.1. In this design, the bottom plate is connected to the rest of the vehicle using an angle shaped joint. The joint connects the bottom panel with the vertical walls of the vehicle. The bottom panel is designed to withstand mine blast loads, while the joint is designed to absorb and interrupt the shock propagation throughout the

vehicle structure, thus preventing major damage due to shock loading to the remainder of the vehicle. Different views, of the joint and the connecting plates are displayed in Figures 4.2 and 4.3.

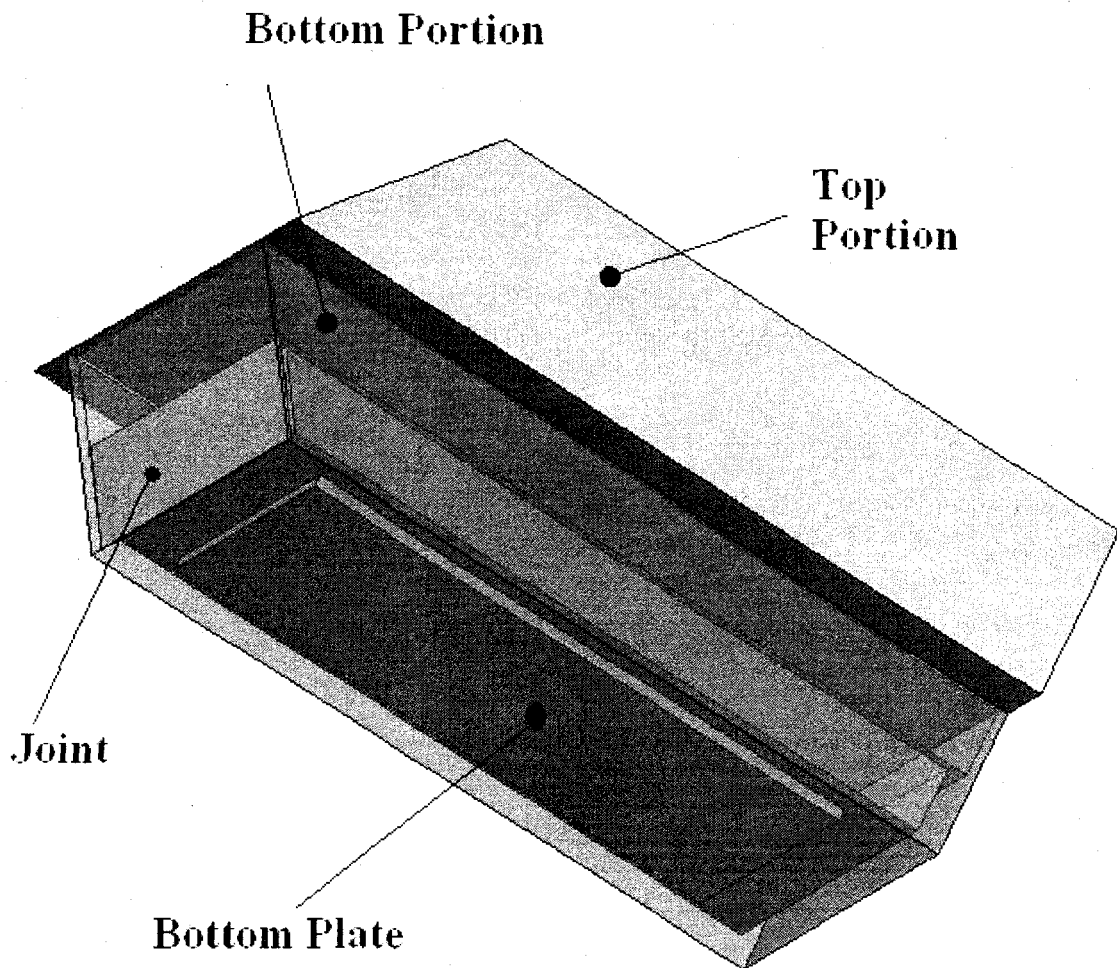


Figure 4.1 Vehicle Model with Joint (Bottom portion is made transparent to view joint)

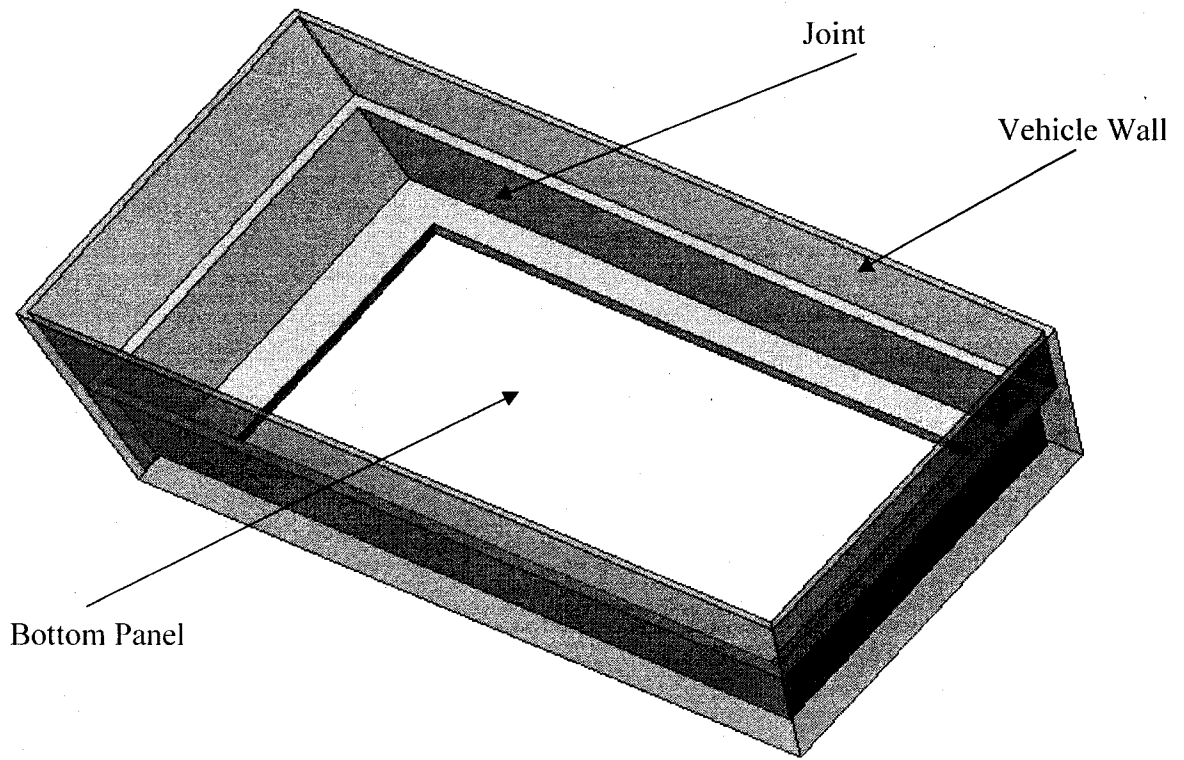


Figure 4.2 Typical Joint Configuration (Bottom portion of the vehicle including joint)

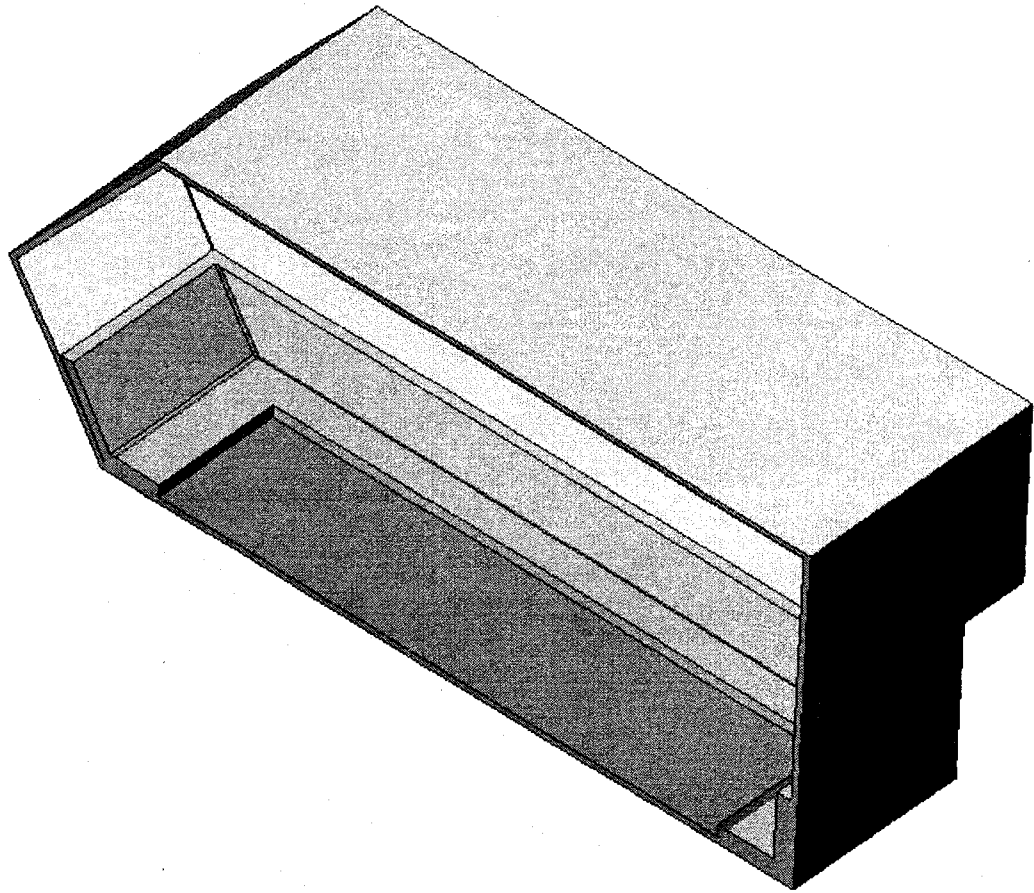


Figure 4.3 Sectional View of the Vehicle Model with Joint

A joint could be connected to the main vehicle model in various ways. One way is by the use of adhesive which allows for good bonding. Another possible way is to weld the joint to the adjacent plates. However upon damage or for repair, disassembly of the joint will become very difficult. For the ease of assembly / disassembly, bolting the joint to the vehicle structure would be a more appropriate method [30]. In this study, only bonding connection method is explored since the explicit code LS-DYNA provides pre-defined contact cards which can be approximated to perfect bonding conditions.

4.2 Parametric Finite Element Analysis

The entire finite element model consists of two parts - vehicle and the joint. The joint is assumed to be bonded to the vehicle, which means that the bond material follows the same behavior as the adjacent material. Appropriate size of the joint for mitigating shock will be determined by optimization studies. Shell elements are used for the vehicle and joint structures. For creating a parametric model, the entire vehicle joint model is divided into fixed and variable portions.

4.2.1 Fixed Code

The vehicle structure (without joint) itself is divided into two parts: the bottom panel and the rest of the vehicle. The vehicle structure model, excluding the bottom panel and the joint, is as shown in Figure 4.4. Elements on this portion have a fixed size and shape. This fixed region is modeled and meshed in ANSYS 8.0, discussed in Section 3.2.3. This part of the vehicle is discretized into 21,186 shell elements that approximate size 0.04 m square as shown in Figure 4.5. An LS-DYNA input file is created using the ANSYS model and the other necessary cards like boundary conditions, material properties, control, and database cards etc, are added to form the fixed portion of the LS-DYNA input file.

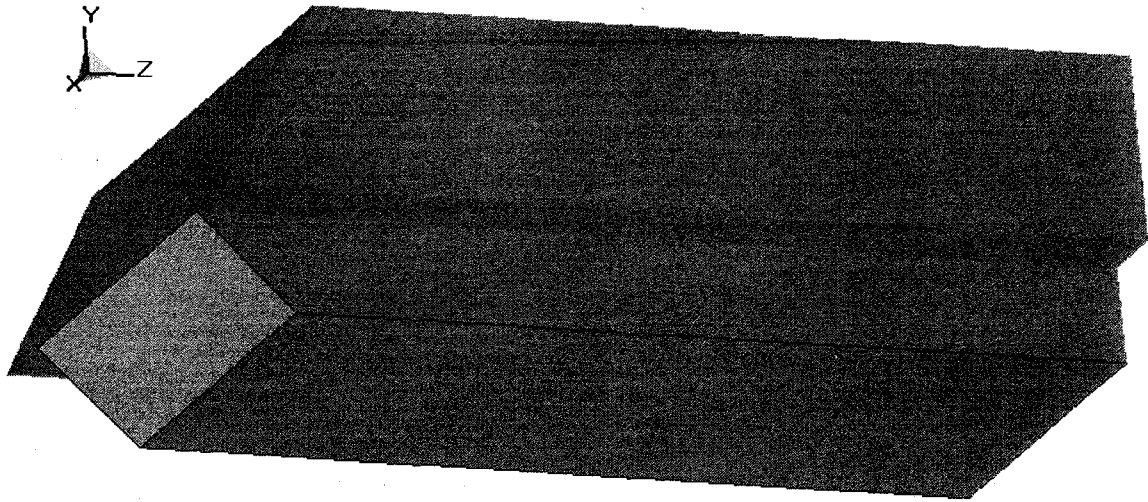


Figure 4.4 Model Geometry – Fixed Part

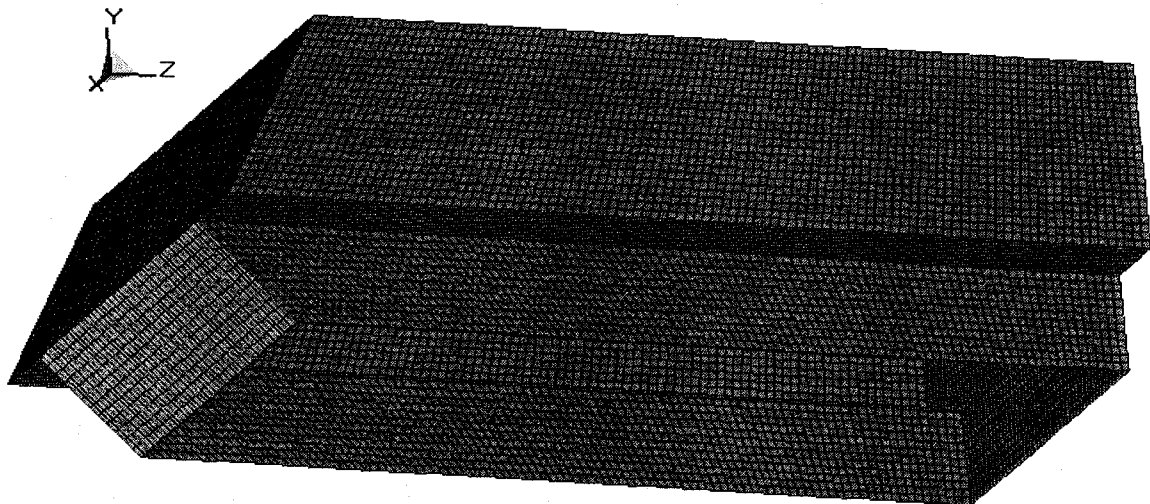


Figure 4.5 Mesh - Fixed Part

4.2.2 Variable Code

The variable part consists of the joint and the vehicle bottom panel. The joint geometry is described by using four dimensions; thicknesses, t_3 and t_4 , and lengths, L_3 and L_4 , as shown in Figure 4.6. If the value of either L_3 or L_4 changes, the geometry is altered and consequently the mesh of the dynamic part of the model needs to be changed.

Hence, a parametric modeling and meshing approach is adopted for this part. For this purpose, a MATLAB code is written to perform the operations that are required to create and mesh the dynamic part of the model based on the joint dimensions.

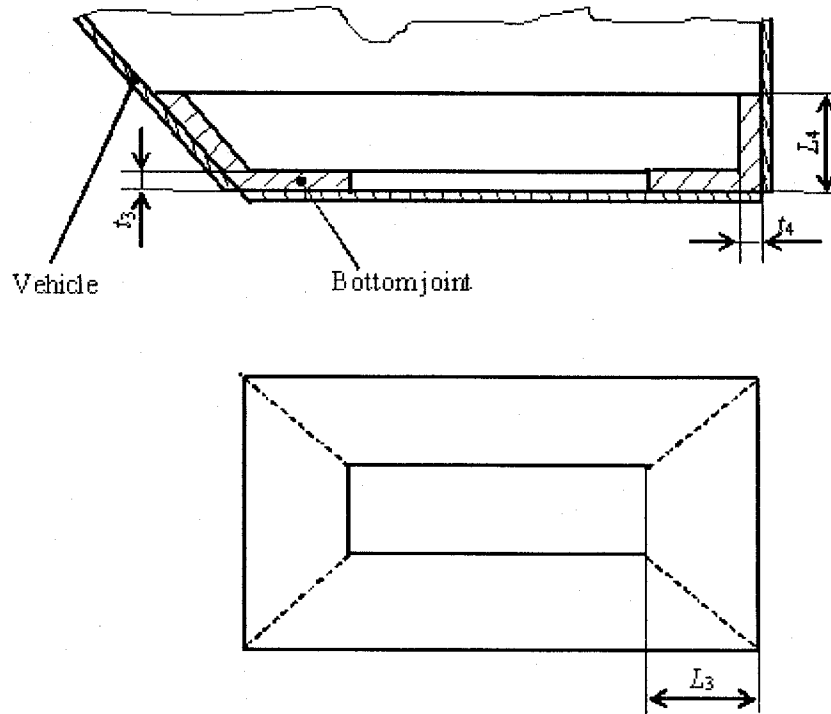


Figure 4.6 Joint Design Variables

4.2.2.1 Modeling Procedure

Initially keypoints, then lines and finally areas are created to form the joint and the vertical plate. The dimensions of all of these areas are entirely dependent on the values of the four variables (t_3 , t_4 , L_3 , and L_4). The joint is divided into eight areas (A2 through A9) as shown in Figures 4.7 and 4.8. The horizontal portion of the joint which connects the bottom panel of the vehicle is divided into four areas (A2 through A5), while the rest of the four areas (A6 through A9) constitute the vertical portion of the joint which connects the upper part of the vehicle structure. In Figure 4.7, the points 1, 2, 3,

and 4 correspond to the keypoints P_{11} , P_{12} , P_{15} and P_{16} , respectively as shown in Figure 2.6. The coordinates of these keypoints are listed in Table 2.7. This area represents the portion excluded in the fixed code of the vehicle model, shown in Figure 4.5. The geometry (rectangular definition) of A1 is fixed and its shape varies according to joint parameters. Beginning with this fixed shape and based on the values of the design variables, the coordinates of the points necessary to create areas which form the joint's horizontal portion (A2 through A9) and the vertical portion (A10 through A14) are found out as explained in several steps below.

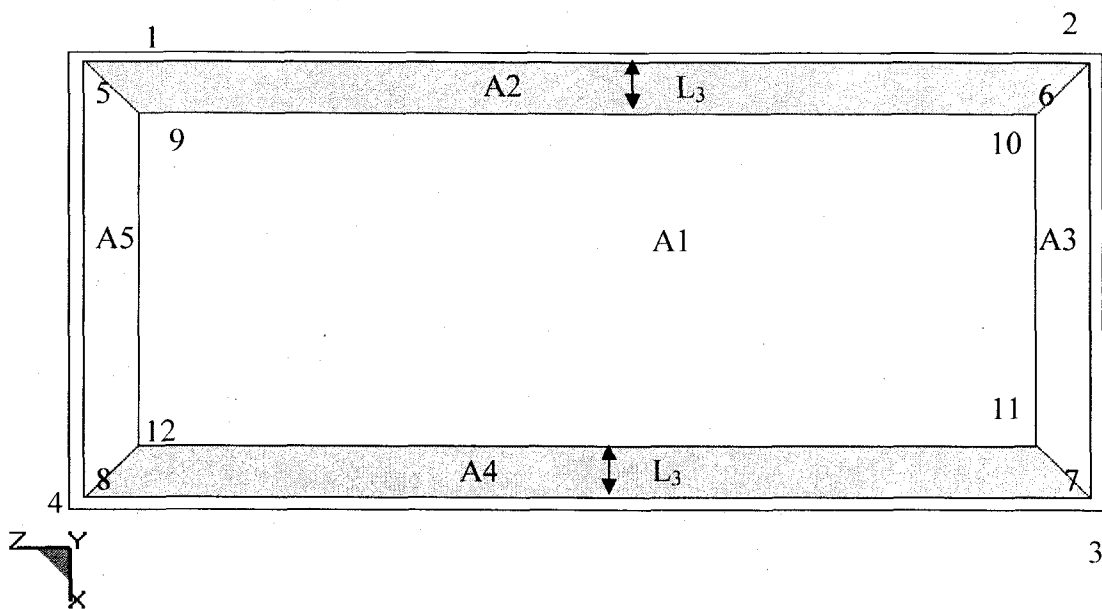


Figure 4.7 Top View Showing the Joint Areas A2-A5 and Outline of the Vehicle Bottom Section

Step 1: Modeling of Joint Areas A2 through A5

The joint outline (represented by the points 5, 6, 7, and 8) shown in Figure 3.10, is modeled at a small offset value from the area A1 (points 1, 2, 3, and 4). This offset value

is set equal to half the sum of the variable T (vehicle hull thickness) and t_2 . This offset is necessary to allow for the thickness of the shell elements used for the vehicle and the joint. The innermost hollow region (formed by points 9, 10, 11 and 12) is of the same shape as the joint outline (points 5, 6, 7, and 8). The width of the areas A2, A3, A4 and A5 is set equal to the variable dimension L_3 . From this information, the locations of the points 9, 10, 11, and 12 can be computed. The equations used to compute the coordinates of the points 5 through 12 relative to the coordinates of the fixed points 1 through 4 are shown in Table 4.1 below. Once the locations of all the points (1 through 12) are known, the appropriate set of points are joined to create areas A2, A3, A4, and A5.

Table 4.1 Relations for Computing the Coordinates' of Points 5 through 12

KP #	X Coordinate	Y Coordinate	Z Coordinate
5	$x_1 + ((T+t_1)/2)$	$y_1 + ((T+t_2)/2)$	$z_1 + ((T+t_1)/2)$
6	$x_1 + ((T+t_1)/2)$	$y_1 + ((T+t_2)/2)$	$z_2 - ((T+t_2)/2)$
7	$x_3 + ((T+t_1)/2)$	$y_1 + ((T+t_2)/2)$	$z_2 - ((T+t_2)/2)$
8	$x_3 + ((T+t_1)/2)$	$y_1 + ((T+t_2)/2)$	$z_1 + ((T+t_1)/2)$
9	$x_1 - ((T+t_1)/2)$	$y_1 + ((T+t_2)/2)$	$z_1 + (L_3 + (T+t_2)/2)$
10	$x_1 - ((T+t_1)/2)$	$y_1 + ((T+t_2)/2)$	$z_2 - (L_3 + (T+t_2)/2)$
11	$x_3 + ((T+t_1)/2)$	$y_1 + ((T+t_2)/2)$	$z_2 - (L_3 + (T+t_2)/2)$
12	$x_3 + ((T+t_1)/2)$	$y_1 + ((T+t_2)/2)$	$z_1 + (L_3 + (T+t_2)/2)$

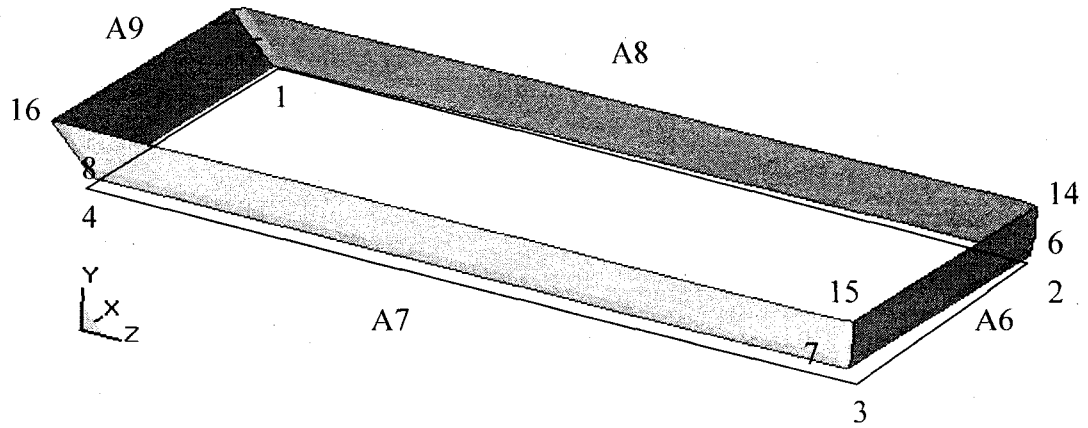


Figure 4.8 Joint Areas A6-A9 and Outline of the Vehicle Bottom Section

Step 2: Modeling of Joint Areas A2 through A5

Areas A6, A7, A8, and A9 of the joint are vertical in direction and represent the upper portion of the joint. The height of these areas is set equal to the value of the joint dimension L_4 . The vertices of the areas A6 through A9 are marked by points 5 through 8 and 13 through 16. The coordinates of points 5-8 are computed using the relations in Table 4.1. The equations used to compute the coordinates of the points 13 through 16 relative to the coordinates of the fixed points 1-4 are shown in Table 4.2. The Φ value in the table represents the slope of the line due to coordinates P_9 and P_{11} shown in the Table 3.1.

Table 4.2 Relations for Computing the Coordinates' of Points 13-16

KP #	X Coordinate	Y Coordinate	Z Coordinate
13	$x_1 + ((T+t_3)/2)$	$y_1 + L_4 + ((T+t_3)/2)$	$z_1 + (((T+t_4)/2) / (\Phi))$
14	$x_1 + ((T+t_3)/2)$	$y_1 + L_4 + ((T+t_3)/2)$	$z_2 - ((T+t_4)/2)$
15	$x_3 + ((T+t_3)/2)$	$y_1 + L_4 + ((T+t_3)/2)$	$z_2 - ((T+t_4)/2)$
16	$x_3 + ((T+t_3)/2)$	$y_1 + L_4 + ((T+t_3)/2)$	$z_1 + (((T+t_4)/2) / (\Phi))$

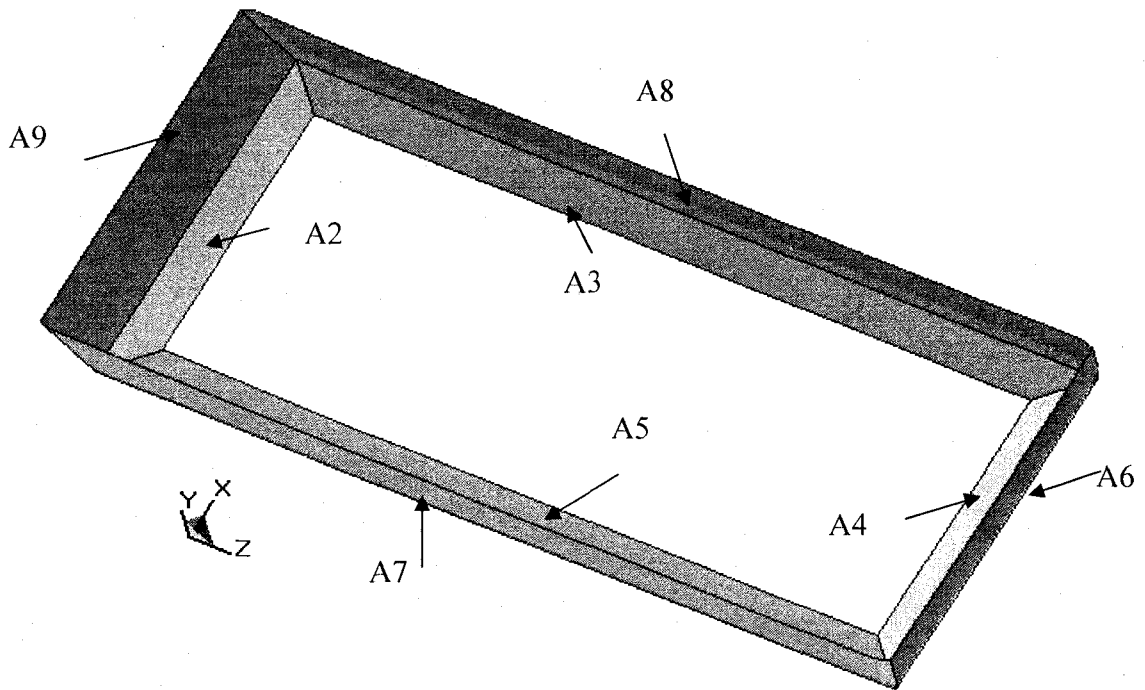


Figure 4.9 Complete Joint Model (Areas A2-A9)

Step 3: Modeling of Bottom Panel (Areas A10 through A14)

The vehicle bottom panel, shown in Figure 3.5, is created by dividing it into five areas (A10 through A14) as shown in Figure 4.10. The model is developed such that there is an exact size and shape match between the areas A2, A3, A4, and A5 on the joint

and the areas A10, A11, A12, and A13 on the bottom panel respectively. It can be noted that the area A14 matches the hollow shape in the middle of the joint, shown in Figure 4.9. The entire joint is created at an offset distance, equal to half the sum of ' t_1 ' and ' T ', from the bottom panel in the y-direction. This is done to account for the shell thicknesses of the vertical plate ' t_1 ' and the vehicle hull ' T '. The coordinates of the points 17 through 24 used to create these areas are computed using the relations shown in Table 4.3.

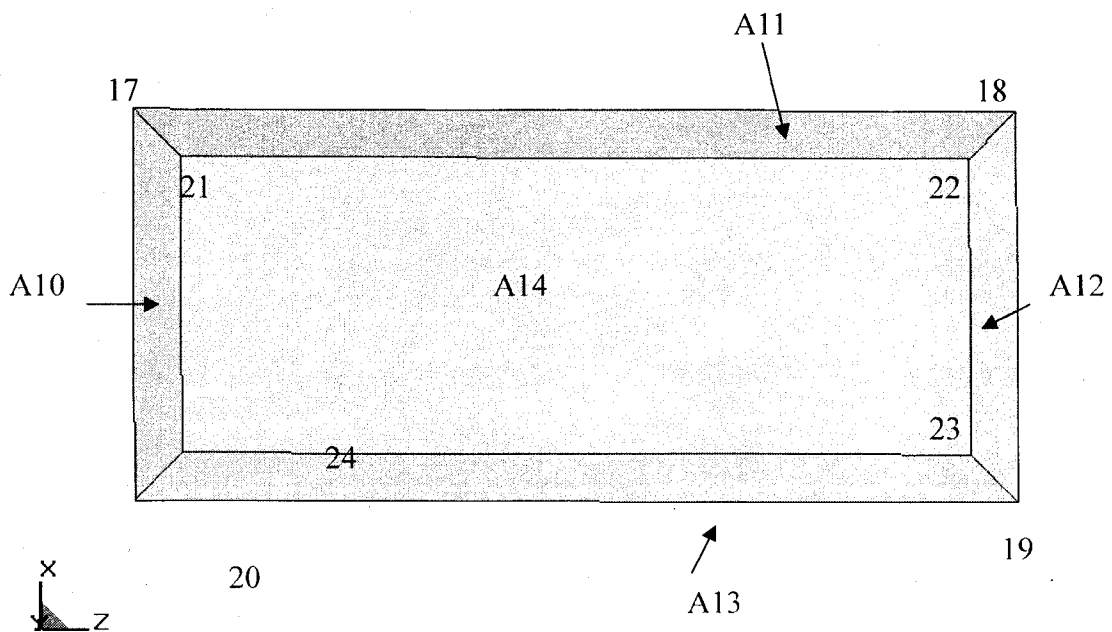


Figure 4.10 Different Areas of the Bottom Plate

Table 4.3 Relations for Computing the Coordinates' of Points 17 through 24

KP #	X Coordinate	Y Coordinate	Z Coordinate
17	$x_1 - ((T+t_4)/2)$	y_1	$z_1 + ((T+t_4)/2)$
18	$x_1 - ((T+t_4)/2)$	y_1	$z_2 - ((T+t_4)/2)$
19	$x_3 + ((T+t_4)/2)$	y_1	$z_2 - ((T+t_4)/2)$
20	$x_3 + ((T+t_4)/2)$	y_1	$z_4 + ((T+t_4)/2)$
21	$x_1 - L_3 - ((T+t_4)/2)$	y_1	$z_1 + (L_1 + (T+t_4)/2)$
22	$y_1 - L_1 - ((T+t_4)/2)$	y_1	$z_2 - (L_1 + (T+t_4)/2)$
23	$y_3 + L_2 + ((T+t_4)/2)$	y_1	$z_2 - (L_1 + (T+t_4)/2)$
24	$y_3 + L_2 + ((T+t_4)/2)$	y_1	$z_1 + (L_1 + (T+t_4)/2)$

4.2.2.2 Meshing

The mesh on the joint and the vehicle bottom panel varies depending on the size of the joint used; hence parametric meshing is adapted for these parts. Figure 4.11 shows the side view of the joint region. The mesh on the joint areas A2 to A5 is first created. Similar mesh patterns are then used on the corresponding areas A10 to A13 of the bottom panel. The complete mesh creation is explained in the steps below.

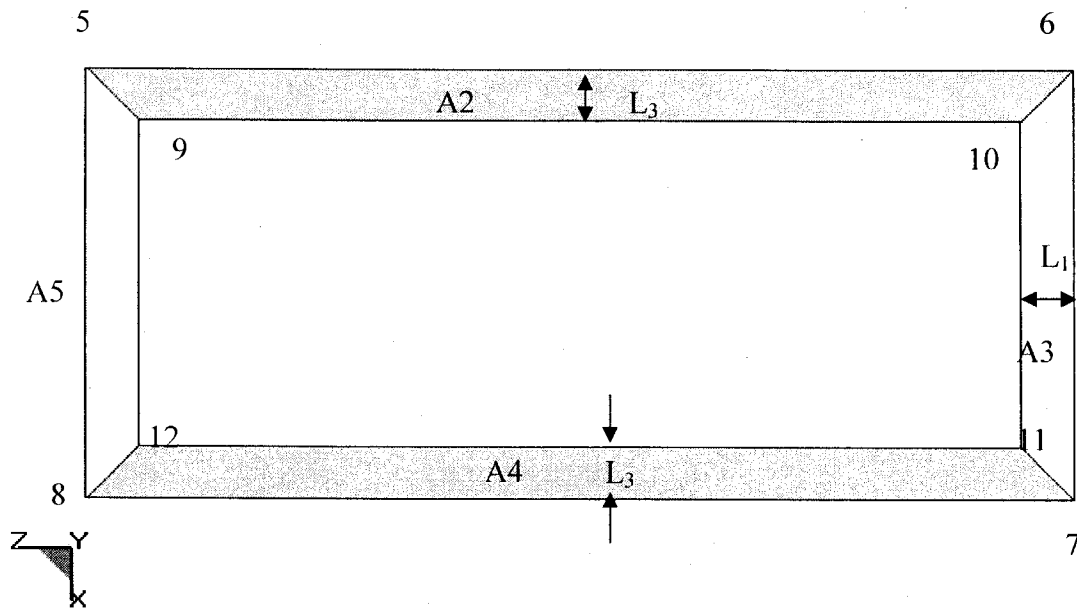


Figure 4.11 Side View of the Joint Areas A2-A5

Step 1: Meshing Area A2 – Calculations of Number of Division along its Length

The basic element size (length and width), denoted as 'w', is fixed at 0.04 m. The process of meshing the area A2 is discussed first. The number of element divisions (N_{e1}) on the line connecting the points 5 and 6, is determined by dividing the length of the line ($z_6 - z_5$) by the element edge length value 'w'. The value obtained is rounded off to the nearest integer and is used as the number of element divisions on the line connecting the points 5 and 6. The line, connecting the points 9 and 10, also has the exact same number of divisions.

Step 2: Meshing Area A2 – Calculations of Number of Division along its Height

Mesh divisions along the height of the area A2 or the line connecting the points 5 and 9 is dependent on the value of L_3 . The number of mesh divisions is required to be even so that there is always a line of nodes midway between the lines connecting the points 5 and 9, and points 6 and 10. The element edge length is set to be at least 'w'. The length of the line connecting the points 5 and 9 is divided by 'w' and the resultant value is rounded off to the nearest lower even integer to obtain the element divisions (N_{e2}) on the line connecting the points 5 and 9.

Step 3: Meshing Areas A3 through A5 of the Joint

Similar approach is used to create the mesh pattern for the remaining areas A3, A4 and A5. The mesh patterns for these areas are as shown in Figure 3.15. For a sample value of 0.25 m for ' L_3 ', the number of element divisions would be computed as: $N_{e1} = 0.25/w$. Since ' w ' = 0.04, $N_{e1} = 6.25$ which when rounded off to the nearest integer yields the value of $N_{e2} = 6$. Figure 4.12 shows the meshed model of the areas A2 through A5. It can be observed that any two neighboring areas share the same nodes at the line of contact.

Step 4: Meshing Areas A6 through A9 of the Joint

The size and mesh of the areas A6, A7, A8, and A9 of the joint are dependent on the dimension ' L_4 '. Similar procedure as described in Step 3 is used to create the mesh pattern shown in Figure 3.15. For a sample value of 0.190 m for ' L_2 ', N_{e3} would be $0.190/w$. Since ' w ' = 0.04 here, $N_{e3} = 4.75$ which when rounded yields the value of $N_{e3} = 5$. The mesh of areas A6 through A9 is shown in Figure 4.13. Figure 4.14 shows the complete joint mesh. From Figure 4.14, it can be observed that the number of divisions

along the length of the joint areas A6, A7, A8, and A9 matches exactly with the number of divisions along the length of joint areas A2 through A5 so that there is a node to node coordination between these two sets of areas. This allows for the continuous flow of shock from joint areas A2 through A5 to A6 through 9.

Step 5: Meshing Areas A10-13 of the Bottom Panel

The bottom panel areas A10, A11, A12, and A13 are meshed in exactly the same manner as the corresponding areas (A2, A3, A4, and A5) on the joint respectively. The bottom panel mesh is shown in Figure 4.15. The exact mesh pattern of the bottom panel with that of the bottom portion of the joint helps in smooth propagation of shock throughout the joint and the rest of the vehicle structure when subjected to a shock load in the form of mine blast. The complete vehicle joint meshed model is shown in Figure 4.16.

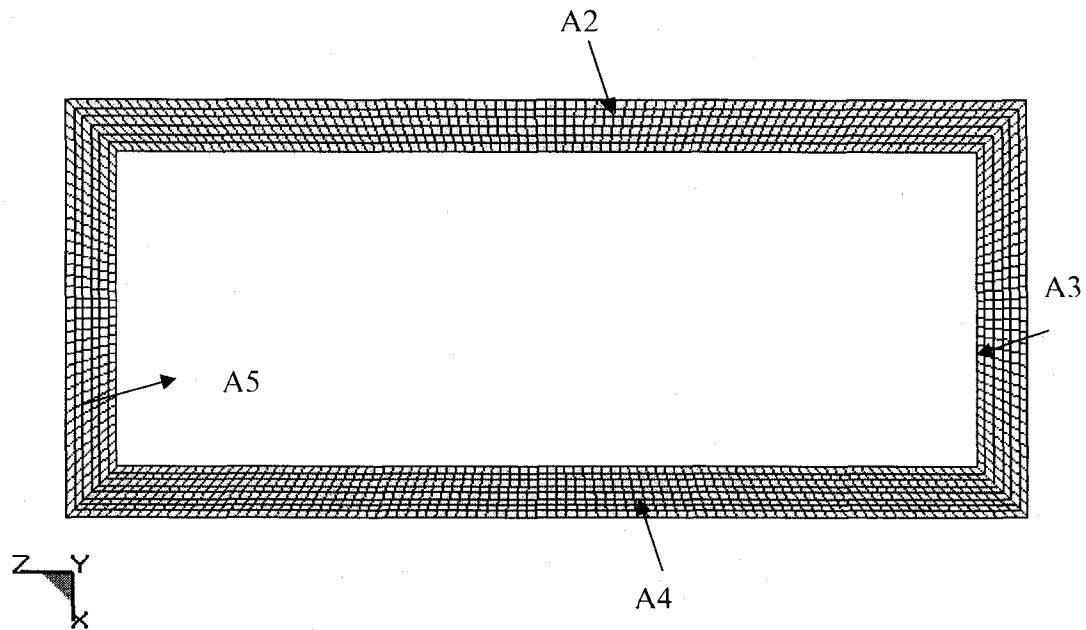


Figure 4.12 Meshed Joint - Areas A2, A3, A4, and A5

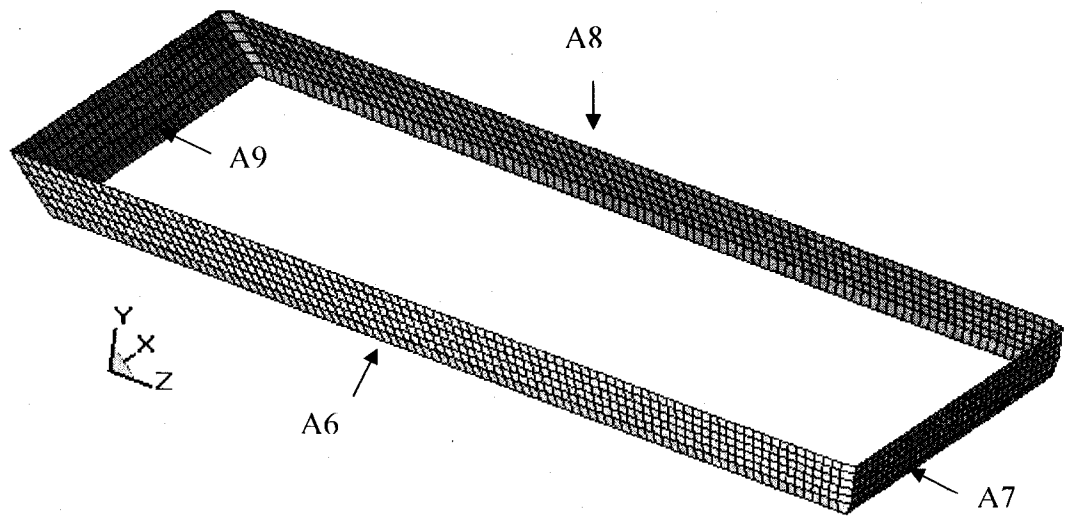


Figure 4.13 Meshed Joint - Areas A6, A7, A8, and A9

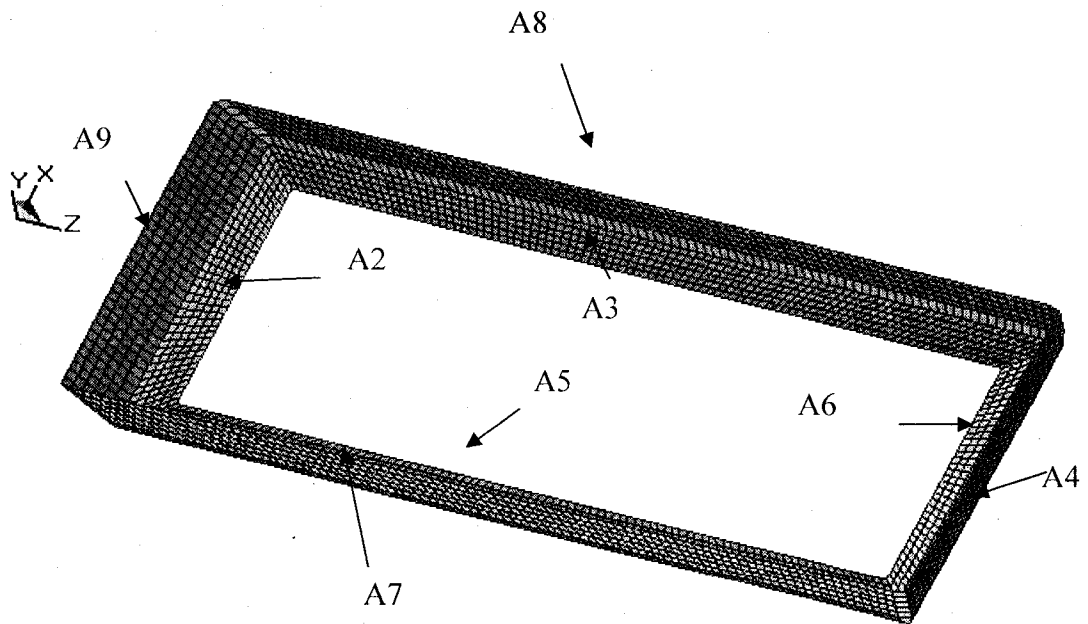


Figure 4.14 Complete Meshed Joint - Areas A2-A9

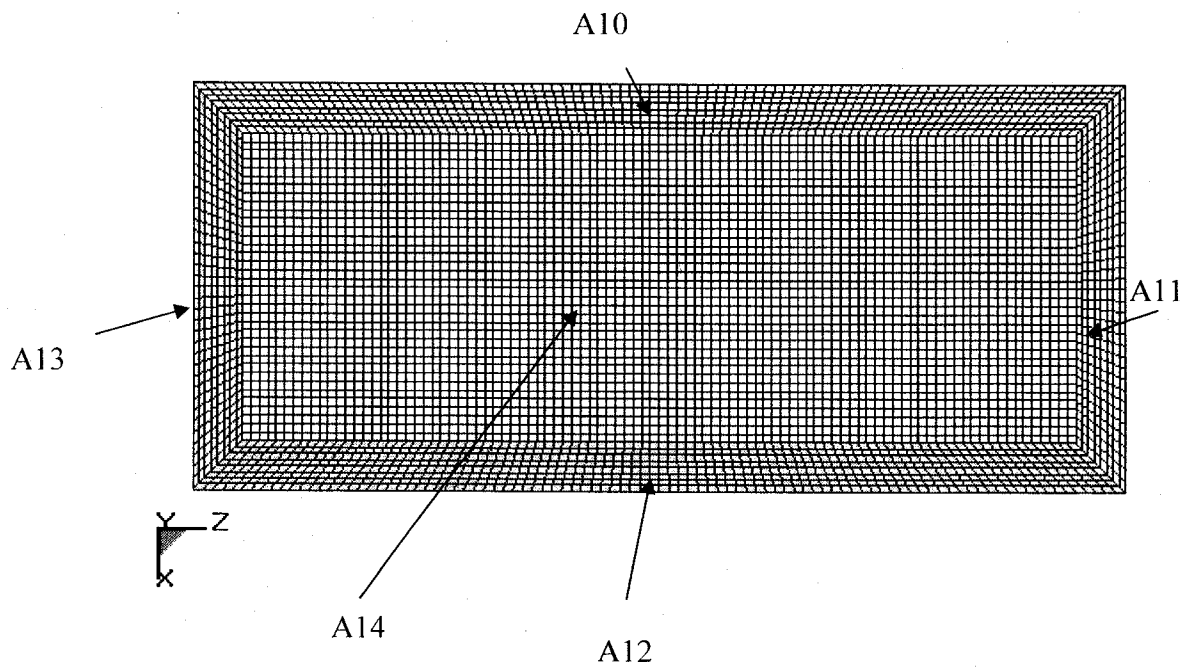


Figure 4.15 Meshed Vertical Plate - Areas A10-A14

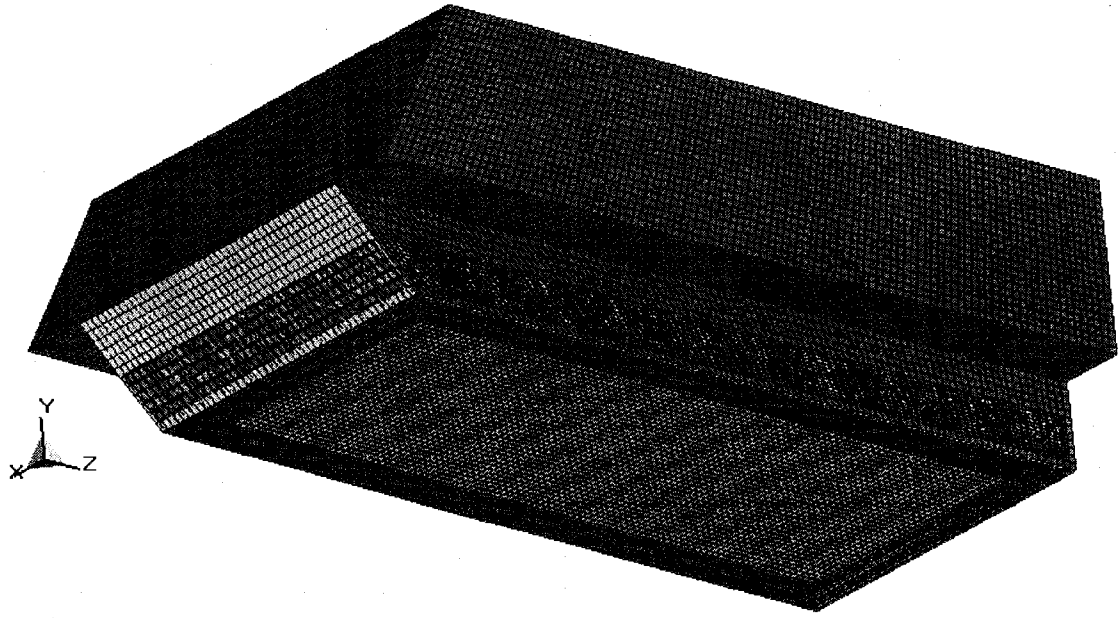


Figure 4.16 Meshed Complete Vehicle Joint Model

4.2.3 Parameters for LS-DYNA Analysis

4.2.3.1 Contact Surfaces

The complete vehicle-joint model is analyzed using the explicit code, LS-DYNA. The structural interaction between the joint and the vehicle is given using pre-defined contact cards available in the code. The bonded contact between the joint and the vehicle is simulated the card CONTACT_TIED_SURFACE_TO_SURFACE card. For this contact card, a master surface (on the vehicle wall) and a slave surface (on the joint surface) are selected. As the name implies, the slave surface always follows the master surface to ensure that the joint surfaces deformation follows those of the corresponding ones at the bottom panel. A sample contact card is shown below. This contact definition requires input of three mandatory cards. The first card gives details of the surfaces in contact. The second card is used to give the values of friction between the interacting surfaces while

the final card is given to variety of scale factors on for the surfaces. The detail of the cards is explained below.

```
*CONTACT_TIED_SURFACE_TO_SURFACE
$      ID
      1
$      SSID      MSID      SSTYP      MSTYP
      2          10          3          3
$      FS        FD        DC        VC        VDC        PENCHK        BT        DT
      0.0        0.0        0.0        0.0        0.0          0          0.0 1000000.0
$      SFS        SFM        SST        MST        SFST        SFMT        FSF        VSF
      1.0        1.0        0.0        0.0        1.0        1.0        1.0        1.0
```

- SSID, MSID defines the slave set ID and master set ID respectively.
- SSTYP set to a value of three indicates that the slave set type is by part ID.
- MSTYP set to a value of three indicates that the master set type is by part ID indicating that the values under SSID and MSID are the part numbers of the corresponding surfaces. In this case, part 2 is the slave surface and part 10 is the master surface. Parts are numbered in the same way as the areas have been numbered in Figures 4.9 and 4.10. Hence part 2 corresponds to area A2, part 3 corresponds to area A3, and so on.
- Other parameters such as FS, FD, DC, and VC which correspond to the various friction coefficients and scale factors are left unchanged as the default values

In this model, there exist eight different areas of the joint that needs to interact with eight different surfaces of the vehicle. This contact definition is given to each pair of surfaces. Each contact pair consists of one slave surface (on the joint) and one master surface (on the vehicle). For the areas A10, A11, A12, and A13, shown in Figure 4.10, of the bottom panel (excluding the central trapezoidal area), designated as the master surfaces, the corresponding areas A2, A3, A4, and A5, shown in Figure 4.9, of the joint are designated as the slave surfaces. Similar contact cards are defined between each of

the rest of the vertical joint areas (A6, A7, A8, and A9) and the main vehicle structure (area A1 or part 1). There are eight pairs of areas which need interaction and hence there are eight contact definitions. The systematic way of defining these contact cards ensures that there is smooth shock wave propagation through out the vehicle-joint model. The details of various contact pair definitions are shown in Table 4.4.

Table 4.4 Contact Pair Definitions

Contact Pair #	Master Surface (Part Id)	Slave Surface (Part Id)
1	10	2
2	11	3
3	12	4
4	13	5
5	1	6
6	1	7
7	1	8
8	1	9

4.2.3.2 Blast Load Definition

The blast load is simulated using the ConWep blast function. A blast load due to a charge of 0.5 Kg of TNT is used to simulate the structural response on the vehicle-joint model. The location where the load is positioned is similar to the one described for the no-joint vehicle case i.e., at (1.343, -0.430, 2.654) m.

4.2.3.3 Effect of Gravity

The effect of acceleration due to gravity on the dynamic response of the vehicle is considered in the model. An acceleration value of 9.81 m/s^2 is defined to consider this effect.

4.2.3.4 LS-DYNA Input Cards

A rigid wall card is used to simulate the vehicle resting on the ground as discussed in section 3.2.6.5. Aluminum 7039-T64 is used as the material for the vehicle structure and the joint. A single material card, similar to the one discussed in section 2.3.5.4., is used to define the material properties for all the parts in the complete vehicle-joint model. Other LS-DYNA input cards such as the control cards, database cards, and Nodout card are similar to those discussed in section 3.2.6. The termination time is set at 0.025 s as in the case discussed in Section 3.2. The accelerations at the three critical locations are computed at every $1\text{e-}5$ s.

4.3 Joint Design Optimization

4.3.1 Design Variables

The objective of this optimization study is to reduce the shock and vibration measures at the critical locations of the vehicle by the introduction of a joint of suitable size. The lengths L_3 and L_4 and thicknesses t_1 and t_2 of the joint, shown in Figure 3.9, are selected as design variables. In order to reduce accelerations at the critical locations, different combinations of these design parameters are tried until an optimal set of dimensions are obtained.

4.3.2 Objective Function

The average of the means of the accelerations at the commander, driver, and panel locations is selected as the objective function to be minimized. The optimization problem can be stated as

$$f = (avg_c + avg_d + avg_p) / 3 \quad (4.1)$$

This objective function needs to be minimized by varying the design variables within the constraint set.

4.3.3 Problem Statement with Constraint Set

The optimization problem can be stated as:

$$\text{Minimize, } f(t_3, t_4, L_3, L_4) = \frac{a_{m_c} + a_{m_d} + a_{m_p}}{3} \quad (4.2)$$

$$\frac{T}{4} \leq t_3 \leq 2T$$

$$\frac{T}{4} \leq t_4 \leq 2T$$

$$\text{Subjected to the constraints: } \frac{x_{P_{16}} - x_{P_{11}}}{16} \leq L_3 \leq \frac{x_{P_{16}} - x_{P_{11}}}{8} \quad (4.3)$$

$$\frac{y_{P_{10}} - y_{P_{12}}}{4} \leq L_4 \leq \frac{y_{P_{10}} - y_{P_{12}}}{2}$$

where, avg_c, avg_d and avg_p are the means of the accelerations at the commander, driver, and panel locations.

T = mean vehicle hull thickness = 0.03175 m

y_{pi} = y coordinate of the 'ith' point as indicated in Figure 4.17

x_{pi} = x coordinate of the 'ith' point as indicated in Figure 4.17

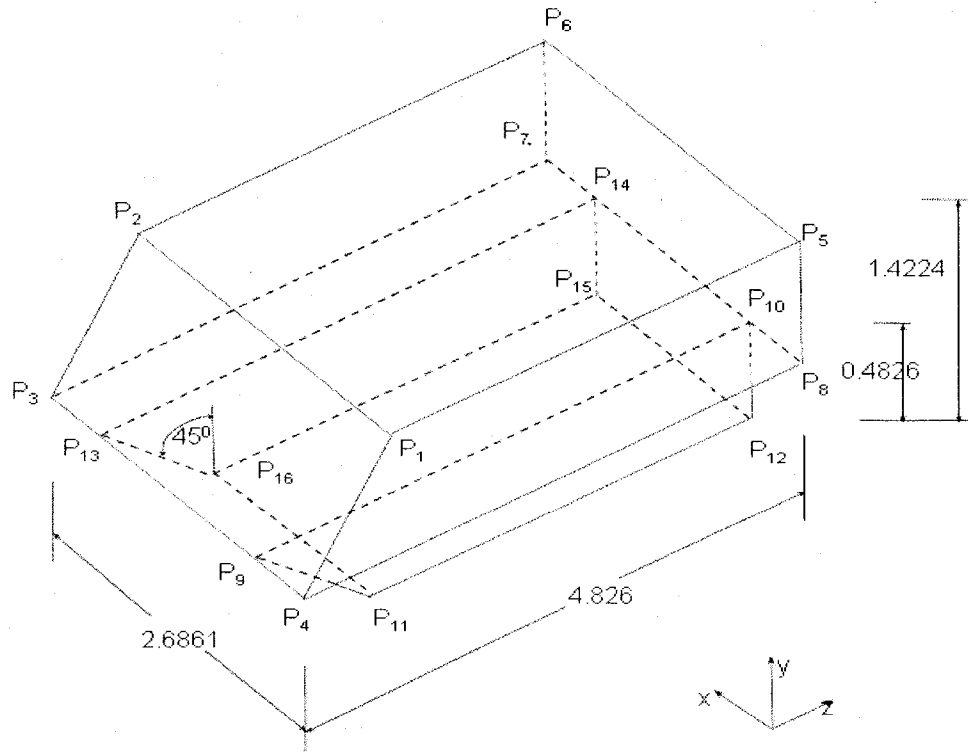


Figure 4.17 APC M113 Hull Model with Keypoints that Define it

It can be seen that the constraints are imposed in such a way that the final joint parameters are within the practical limit of application. The constraints are included in the objective function using penalty terms. Penalty terms are introduced for the limits of the design parameters such that if any of the constraints are violated, then the objective function is not evaluated. The modified objective function after including the penalty terms is given by:

$$\text{Minimize, } F = Af + \sum_{i=1}^m \Omega_i \quad (4.4)$$

If $g_i \leq 0$, then $A = 1$, $\Omega_i = Rg_i^2 + B$.

If $g_i > 0$, then $A = 0$, $\Omega_i = 0$.

R and B are penalty parameters, whose value is 10^{12} and 600,000 respectively. The variable A is introduced in the formulation to avoid calculating objective function when a constraint is violated as the problem is computationally demanding. $g_i(x)$ is equation of constraint i.

4.3.4 Optimization Technique

Figure 4.18 shows the flow of the overall optimization process. The process is described in the steps below:

- Step 1: Once the optimization program is run, generate the values for the design variables according to the Simplex algorithm.
- Step 2: Create the LS-DYNA FE input file using the values of the design variables obtained in Step 1.
- Step 3: Run the input file created in Step 2 using LS-DYNA explicit code solver within the MATLAB environment.
- Step 4: Calculate the objective function
- Step 5: Record the various values of accelerations from the LS-DYNA data output files. Check for the termination criteria. If YES, STOP and terminate. If NO, Go to Step 1 where new values for the design variables are generated according to Simplex algorithm.

The optimization process uses Fuzzy Simplex algorithm developed by Trabia and Lee [27]. This algorithm is used in this study since it can usually reach the minimum point faster than regular simplex algorithm. Also it provides with greater flexibility to vary the search direction which helps immensely in a highly non-linear problem like a blast. The

initial simplex is created according to Spendley, et al. [28] by generating 'n+1' equally-spaced points according to the equation,

$$X_i = X_0 + \delta_1 U_i + \sum_{j=1, j \neq i}^n \delta_2 U_j, \quad (4.5)$$

where, $\delta_1 = \frac{\sqrt{n+1+n-1}}{n\sqrt{2}} \alpha$

$$\delta_2 = \frac{\sqrt{n+1-1}}{n\sqrt{2}} \alpha$$

Here α is the simplex size factor. Since the two thickness variables are of smaller order than the two length variables, the initial simplex is scaled by introducing a scaling vector such that, $X_{i,j} = X_{i,j} s_j$.

Based on extensive testing of the problem, it is decided to have the value of $\alpha = 0.005$, and $s = (1, 1, 2, 2)^T$. The termination criterion is set based on a difference in the consecutive objective function values. This is known as the error parameter and its value is set at 0.1.

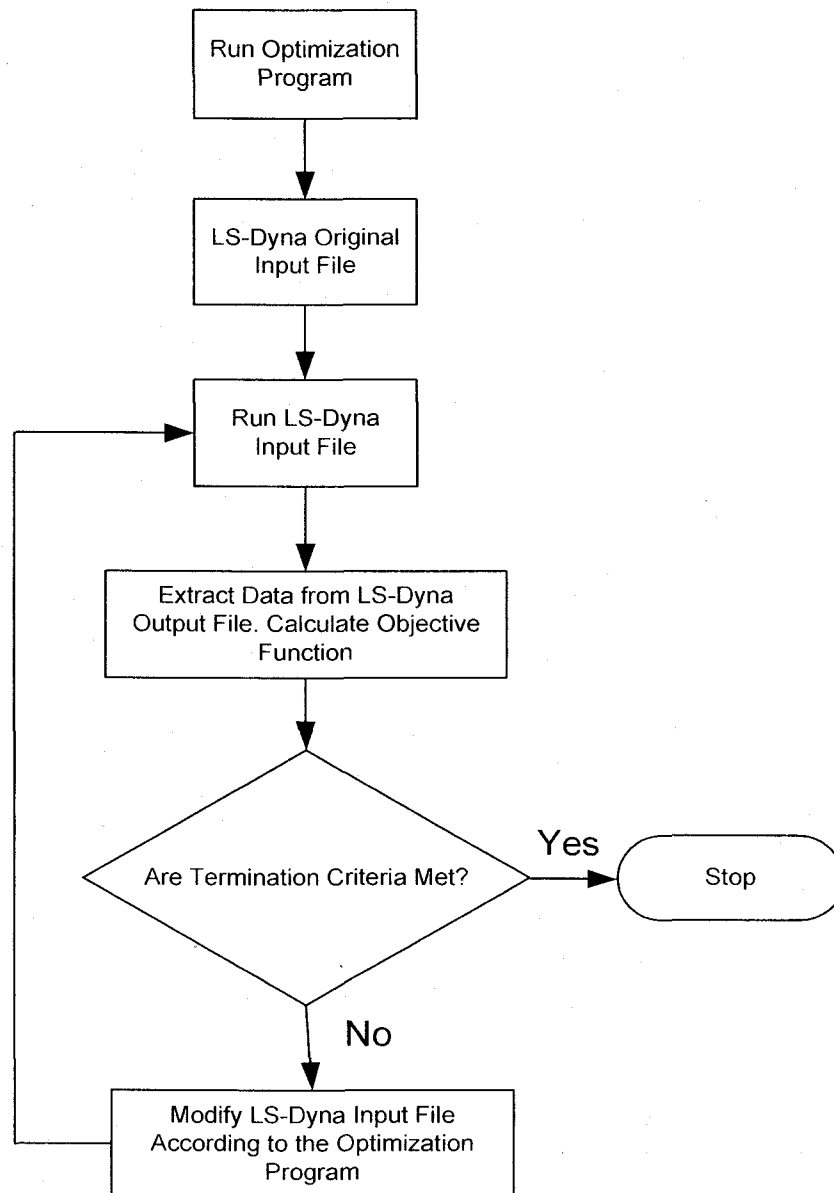


Figure 4.18 Flow Chart Showing the Procedure of the Optimization Program

4.4 Results

The vehicle joint model is run with the loading conditions and different analysis parameters as described in the Section 3.2.3. To better survey the search space, three initial guesses, Table 4.5, are tried. These initial guesses correspond to the lower, mid-range, and upper limits of the four variables respectively. Values of the objective function at the three initial guesses correspond are better than the no-joint case, Table 4.6, which indicates that introducing a joint generally interrupts the flow of the shock. Table 4.6 also shows that the Case 1 (lower limits of the four variables) is the most effective in reducing transmitted shock.

Table 4.5 Various Initial Guesses used for Optimization Searches

	t_3 (m)	t_4 (m)	L_3 (m)	L_4 (m)	f	Joint Mass(Kg)
Case 1	0.0080	0.0080	0.1220	0.1220	1392	67
Case 2	0.0357	0.0357	0.1762	0.1429	1421	378
Case 3	0.0633	0.0633	0.2350	0.2350	1577	983

Table 4.6 Final Results of Optimization Searches

	t_3 (m)	t_4 (m)	L_3 (m)	L_4 (m)	Joint Mass(Kg)
Case 1	0.0103	0.0098	0.2292	0.2412	159
Case 2	0.0285	0.0404	0.2372	0.2029	500
Case 3	0.0620	0.0632	0.2383	0.2401	989

Table 4.7 Accelerations for the Results of Case #1

Maximum acceleration (m/s ²)	commander	3076
	driver	16102
	instrumentation panel	9409
Average acceleration (m/s ²)	commander	773
	driver	2000
	instrumentation panel	774
Maximum acceleration (m/s ²)	commander	3076

Table 4.8 Accelerations for the Results of Case #2

Maximum acceleration (m/s ²)	commander	3523
	driver	18398
	instrumentation panel	8161
Average acceleration (m/s ²)	commander	930
	driver	1890
	instrumentation panel	931
Maximum acceleration (m/s ²)	commander	3523

Table 4.9 Accelerations for the Results of Case #3

Maximum acceleration (m/s ²)	commander	4682
	driver	13083
	instrumentation panel	19762
Average acceleration (m/s ²)	commander	1268
	driver	1991
	instrumentation panel	1268
Maximum acceleration (m/s ²)	commander	4682

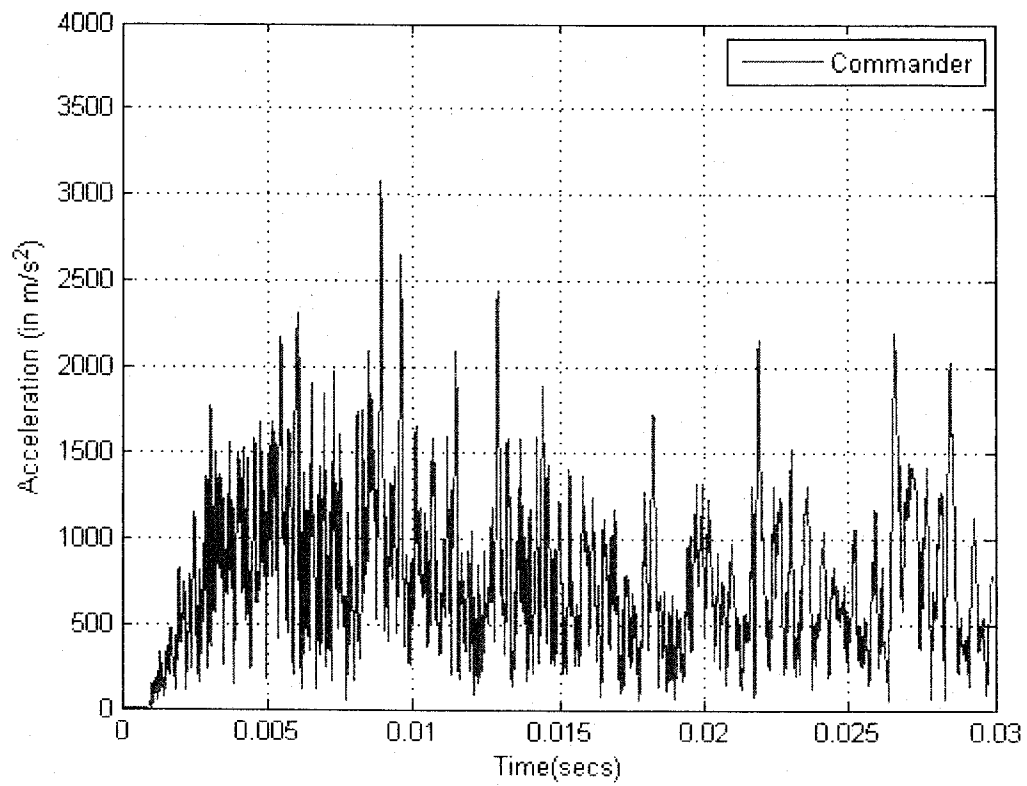


Figure 4.19 Acceleration Curves of Commander Location for Results of Case #1

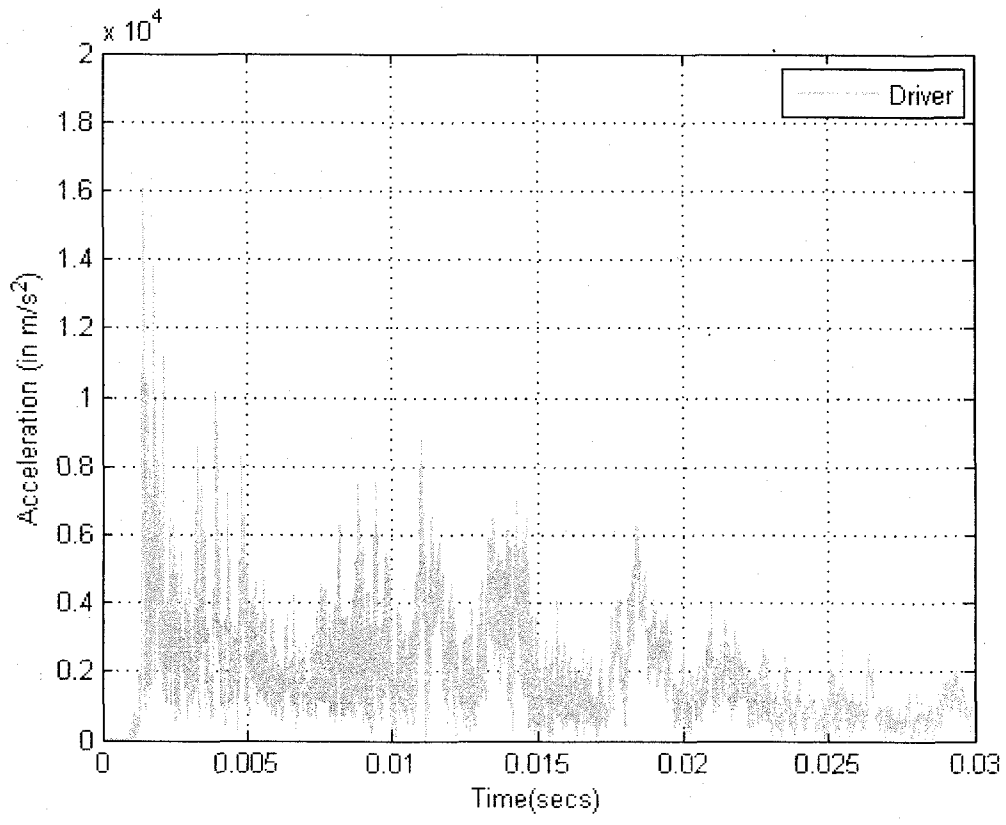


Figure 4.20 Acceleration Curves of Driver Location for Results of Case #1

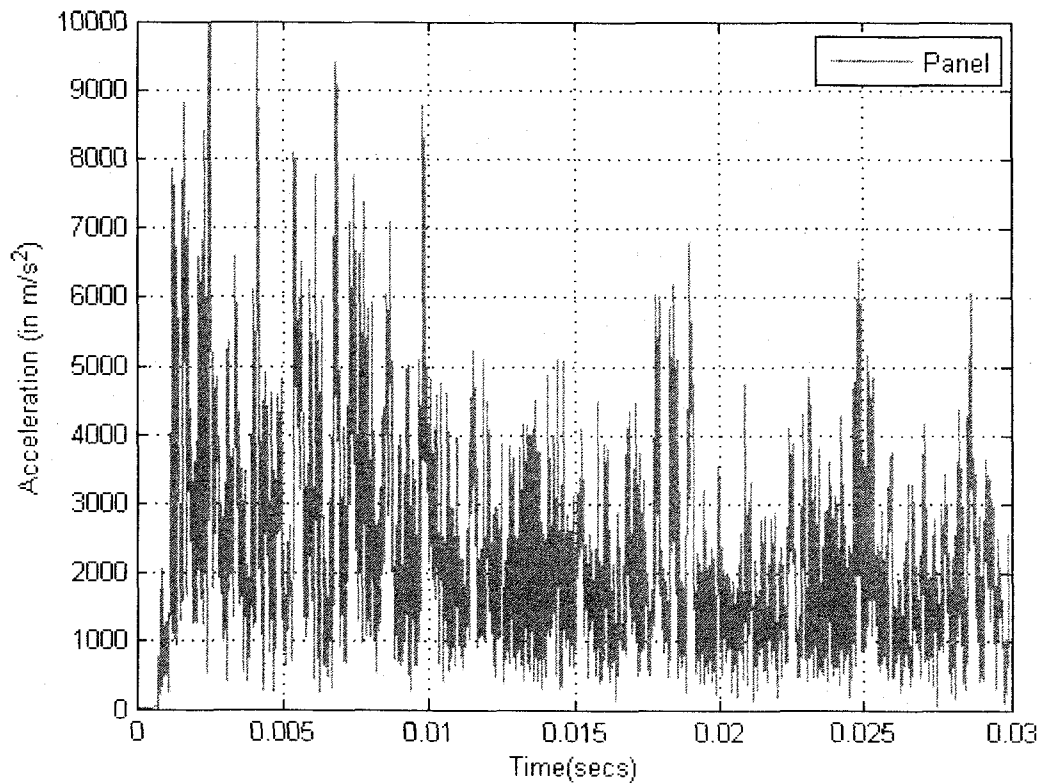


Figure 4.21 Acceleration Curves of Panel Location for Results of Case #1

Optimization results for these three guesses are shown in Table 4.6. Studying the results of this table shows the following:

- Regardless of the initial guess, the search leads L_3 and L_4 toward their upper limits.
- The values of t_3 and t_4 barely change in Case 1.
- While the results of the search in Case 2 are close to those of Case 1, the values of t_3 and t_4 are significantly different, which indicate that a fairly large area with values close to minimum exists within the search space.
- The search of Case 3 (upper limits of the four variables) is the least successful. It starts and ends with the highest objective function values of the three cases.

The acceleration results for each individual case are presented in Table 4.7, 4.8, and 4.9, respectively. The acceleration vs. time curve for the vehicle with the optimized joint of Case 1 is shown in Figure 4.19. Studying these results shows reduction of averages of acceleration waves is not necessarily associated with reduction of the maximum values of accelerations. However reducing averages of accelerations indicates reducing energy transferred into the points of interest. In Case 1 and 2, a reduction of the maximum values of acceleration is observed for the commander and instrumentation panel. The maximum vonmises stress contour for the case#1 is shown in the Figure 4.20. It can be seen that the maximum stress just reaches the yield stress value.

LS-DYNA user input
 Time = 0.030001
 Contours of Effective Stress (v-m)
 max ipt. value
 min=458362, at elem# 20065
 max=3.80137e+008, at elem# 229861

Fringe Levels
 3.801e+008
 3.422e+008
 3.042e+008
 2.662e+008
 2.283e+008
 1.903e+008
 1.523e+008
 1.144e+008
 7.639e+007
 3.843e+007
 4.584e+005



Figure 4.20 Von Mises Stress Contour Plot – Case #1 at 30 ms

CHAPTER 5

OPTIMIZATION- MODEL 2

5.1 Joint Design Characteristics

This chapter deals with optimizing structural design of components and joints of the space frame structure of the AX-1 model under projectile impact loading. The space frame consists of several joints that connect individual beam members to form the whole structure. Monolithic design of such a complex structure is not considered a realistic option due to cost-effectiveness of manufacturing processes.

Usually, the conceptual stage of product development entails identifying components and their joining methods by decomposing the entire product geometry. However, decomposing schemes depend mainly on the designers' experience. This may cause certain problems related to structural stiffness and manufacturability of the final design. In the present design of space frame, manufacturability of the joints has already been dealt with. However, it is important to ensure that the overall structural stiffness is sufficient to cope with highly transient loads.

A major design consideration is reducing the overall weight of the structure as low mass of the vehicle is proportional to fuel consumption. Usually in commercial automobiles, body accounts for approximately one third of the vehicle weight. Considerable mass decrease can be achieved by using aluminum without compromising the performance, which is a reflection of increased adaptation of aluminum for vehicle

body building in many commercial mass-produced vehicles. The entire AX-1 model is made of aluminum. Any further reduction in the mass of the space frame will improve its performance.

The results of Chapter 3 suggest that varying the length of the branches of the joints within the frame can have significant effect on the overall behavior of the space frame under impact loads at various locations. It is not confirmed yet that the current joint locations c are sufficient to provide optimal performance under impact loading. The objective of this chapter is to minimize the mass of the structure by varying the frame design while considering stress and deformation effects.

5.2 Parametric Finite Element Analysis

Parametric finite element analysis is created to evaluate the joint design parameters:

- The length of the branches of the joints and
- The position of the joint locations.

In this study, joints at eight locations are identified for variation. The first four correspond to the numbers shown in Figure 5.1. The other four joints are the symmetric joints of the first four joints. A numbering scheme is used for identifying each branch of a particular joint. The numbers used for identifying branches of joints at locations 1 and 3 are shown in Figure 5.2. As can be seen from the figure, branches are numbered in an counter-clockwise fashion starting from the left most joint branch. Each branch of joint is identified using the variable $B_{i,j}$, where i stands for location number and j stands for branch number. For example, $B_{1,1}$ indicates the first joint branch of joint location 1. Since

most of the joints in the AX-1 model are associated in some way or the other with the rest of the IS-ATD vehicle, only Joint # 3 and its corresponding symmetric joint are chosen for identifying appropriate location by variation. However, appropriate values for the lengths of joint branches and joint locations for mitigating shock transmission are to be determined from optimization studies. For creating the parametric model, the entire model is divided into fixed and variable codes.

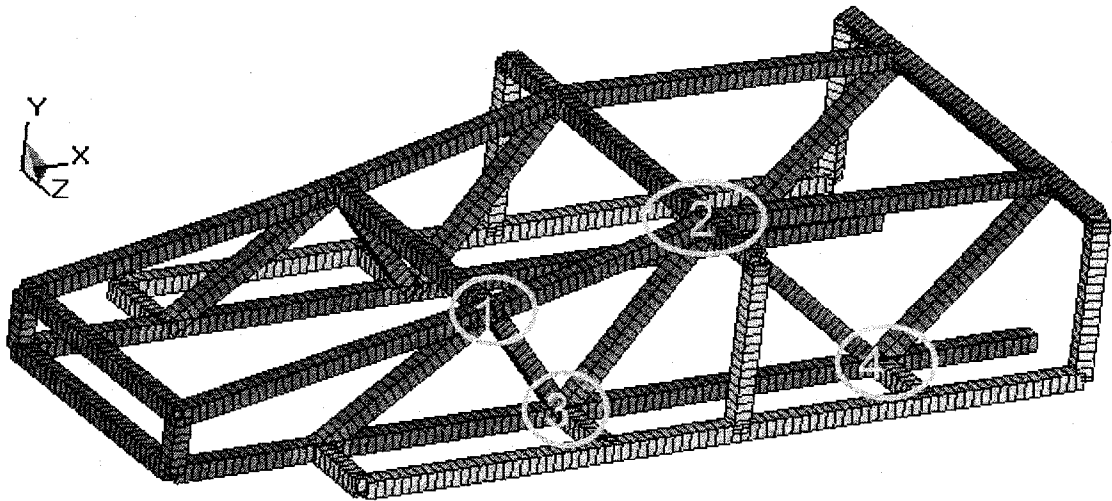


Figure 5.1: Nodal Locations for Parametric Study

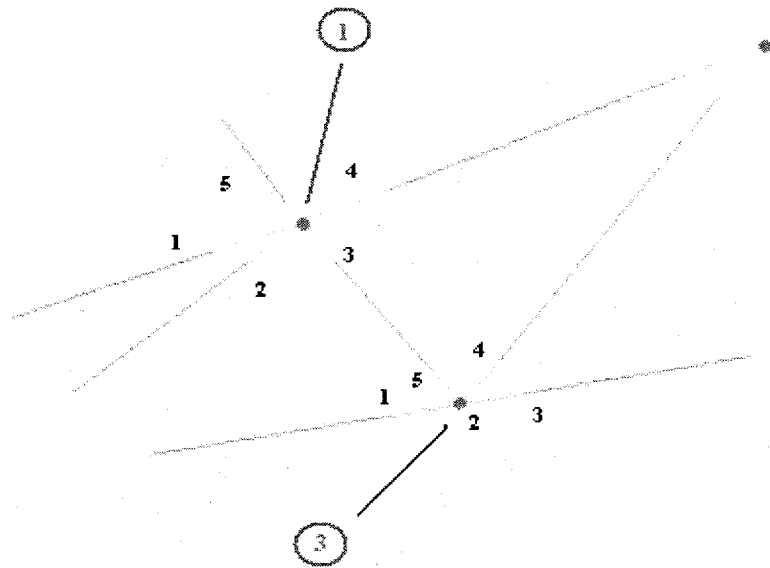


Figure 5.2: Numbering Scheme for Joint Branches

5.2.1 Fixed Code

The fixed code represents the portion of the finite element model where no variations are performed. The fixed region is modeled and meshed using HyperMesh pre-processor. All the details of Model 2 discussed in Chapter 3 remain pertinent for this code too. The fixed code of the FE model is shown in the Figure 5.2, which shows that the fixed code represents the part of the vehicle without the eight joint locations. An LS-DYNA input file is created using the HyperMesh model and the other necessary cards like boundary conditions, material properties, control, and database cards etc, are added to form the fixed portion of the LS-DYNA input file. These cards are exactly similar to those described in Chapter 3.

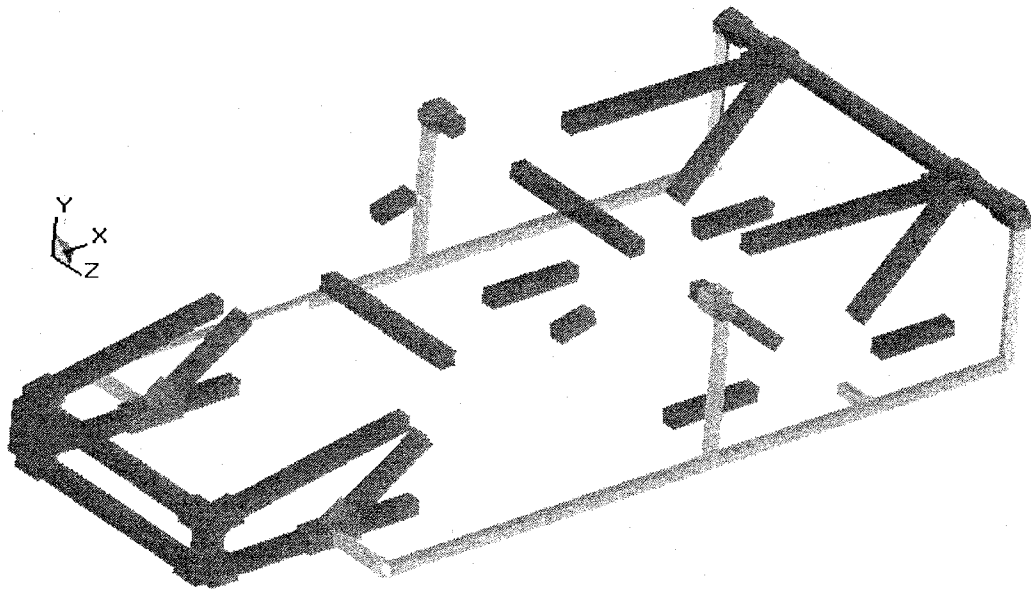


Figure 5.2: Fixed Portion of the Code

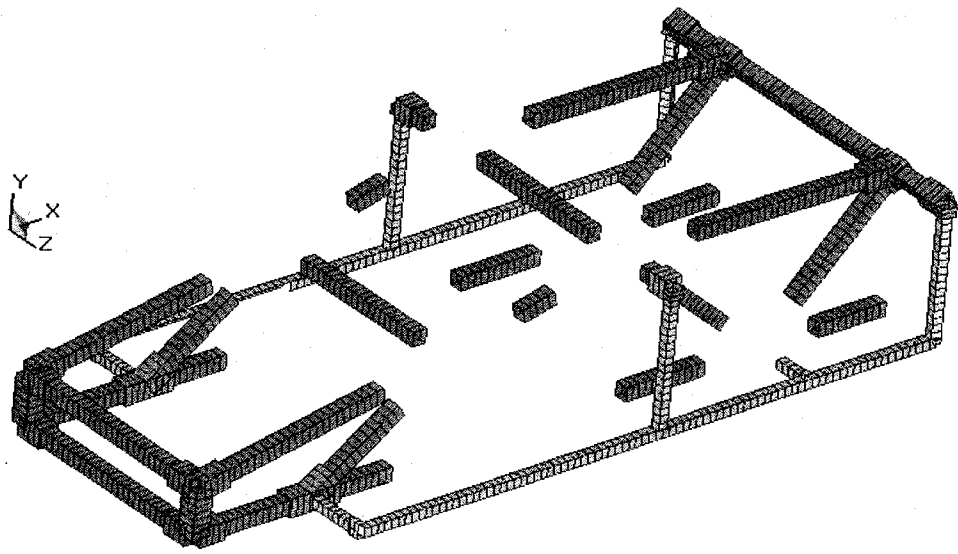


Figure 5.3: Mesh of Fixed Portion of the Code

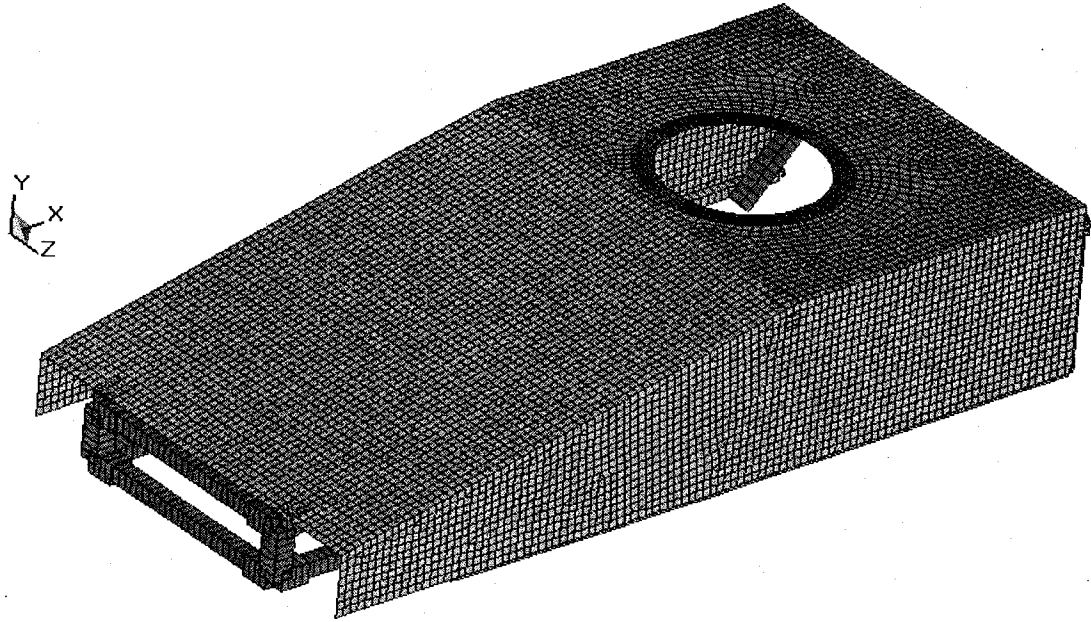


Figure 5.3: Mesh of Fixed Portion of the Code (Complete)

5.2.2 Variable Code

Modeling of the variable code is done for two different cases. The first case is concentrated on modeling the space frame to obtain a parametric relation for the joints and their branches at the eight described locations. This parametric relation is used in conjunction with the optimization algorithm to obtain optimal values of lengths of the branches at the eight joint locations.

The second case derives the parametric relationship to vary both the length of branches of the joints and the location of the joints. The varying part of Model 2 consists of the joints at the eight nodal locations and the associated branches of beams emerging out of them. These elements constitute all the branches that are missing in the static part of the AX-1 model. The elements at these locations are generated so that the total numbers of elements always remain the same when compared with the base model

(Model 2) described in Chapter 3. The variable part of the model is generated by using a program written in Matlab. The details of the modeling are discussed below.

5.2.3 Modeling Case 1

In this section, discussion is concentrated on modeling joint 4 and its associated branches. The joint 4 and its associated branches are shown in the Figure 5.4. As shown in the Figure 5.4, the variable $Q_{i,j}$ describes the number of elements of the one of the joints at joint location 4. Variable $B_{i,j}$ represents certain number of elements along the same branch. The number of elements at this branch are chosen in such a way that the total number is at least half of the total number of elements used along the branch. $S_{i,j}$ represents the number of elements obtained by the sum of $B_{i,j}$ and $Q_{i,j}$ as given in equation 5.1, which is always constant. The value of $S_{i,j}$ remains the same even though there is a change in any of the variables. In this case, the independent variable is $Q_{i,j}$ i.e. for changing the length of the joint branch by varying the number of elements. The variable $B_{i,j}$ is calculated according to equation 5.2.

$$B_{i,j} + Q_{i,j} = S_{i,j} \quad (5.1)$$

$$B_{i,j} = S_{i,j} - Q_{i,j} \quad (5.2)$$

Similar procedure is used for obtaining parametric relations for all the other branches of this joint location and all the other remaining seven locations.

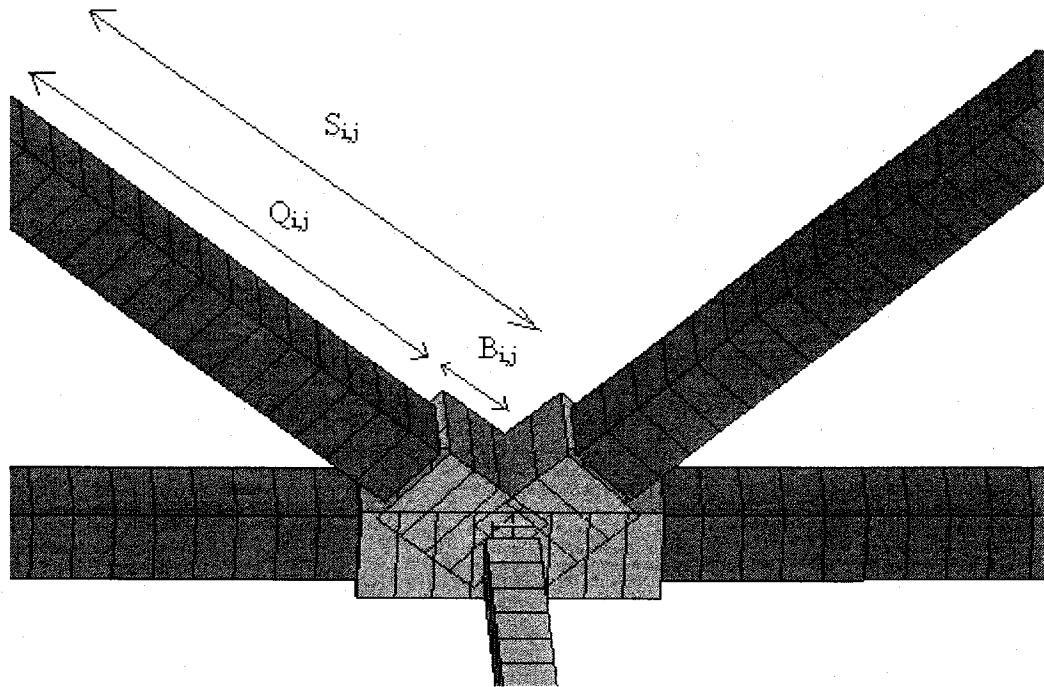


Figure 5.4: Variables for Case 1 Parametric Modeling

5.2.4 Modeling Case 2

Modeling of the variable part in this case is divided in to two parts.

Part 1 consists of modeling to obtain a parametric relationship so that movement of joint locations is possible. In this work, movement of just a single joint location and its corresponding opposite location is considered. The joint location 3 is chosen to perform this movement.

Part 2 consists of modeling all the branches for obtaining a parametric relationship between joints and their associated branches.

5.2.4.1 Modeling and Meshing of part 1

Initially, the model without the joint location at 3 is as shown in the Figure 5.5. As can be seen from the figure, the joint at location 3, its associated branches, and some part

of the frame elements along joint 3 are missing. The objective of this part is to model joint 3 and its associated branches so that the joint location is free to move along the described points 5 and 6. The initial location of this joint 3 and its associated branches is given as shown in Figure 5.6. The location of joint 3 is dependent on the variable y . The various steps in modeling this part are described below.

Step 1: In this stage, coordinate information is recorded for the locations 1, 2, 5, 6, 7, and 3 (Figure 5.6) using the base model described in Chapter 3. Table 5.1 gives the recorded coordinate details.

Table 5.1 Coordinates for Locations Associated with Joint 3

Location	Coordinate
1	(a_1, b_1, c_1)
2	(a_2, b_2, c_2)
3	(l, m, n)
5	(a_5, b_5, c_5)
6	(a_6, b_6, c_6)
7	(a_7, b_7, c_7)

Step 2: In this step, the number of elements used for creating each branch is evaluated and recorded. Since a constant approximate mesh size of 0.04 m is used throughout

modeling, the number of elements used at each branch can be evaluated using the equation 5.3.

$$N_{3,i} = \frac{len_{3,i}}{0.04} \quad (5.3)$$

$$\text{where } len_{3,i} = \sqrt{(a_i - l)^2 + (b_i - m)^2 + (c_i - n)^2}; \quad \forall i=1,2,5,6,7$$

Step 3: In this step, the movement of joint location 3 is performed. Equation 5.4 is used to evaluate the new coordinates of the joint location using the movement variable y . For example, if the value of y is negative, then the new location of 3, given by 3' is generated as shown in the Figure 5.7 using 5.4

$$(l, m, n) + (y, 0, 0) = (l', m', n') \quad (5.4)$$

The range of variable y is described by the equation 5.5 given below

$$\begin{aligned} y > 0, & \text{ (Location3, Location6)} \\ y < 0, & \text{ (Location3, Location5)} \\ y = 0, & \text{ Location3} \end{aligned} \quad (5.5)$$

The range of variable y can be identified from the Figure 5.6. Step 4: At this point of code, element size is evaluated along each branch depending on the number of elements calculated in step 2. The following equation 5.6 is used to calculate the element size along each branch.

$$Size_{3,i} = \frac{len'_{3,i}}{N_{3,i}} \quad (5.6)$$

$$\text{where } len'_{3,i} = \sqrt{(a_i - l')^2 + (b_i - m')^2 + (c_i - n')^2}; \quad \forall i=1,2,5,6,7$$

Step 5: Depending on the element size calculated in step 4, nodes are generated along each branch. The nodes along the branches $B_{3,5}$, $B_{3,6}$ and $B_{3,7}$ are calculated using the following equations.

$$\begin{aligned}
 B_{3,5}: \quad & a = [a_3 - (a_3 * Size_{3,5} * n)], \forall n = 1 \text{ to } (N_{3,1} - 1) \\
 & b = b_5, \forall n = 1 \text{ to } (N_{3,1} - 1) \\
 & c = c_5, \forall n = 1 \text{ to } (N_{3,1} - 1)
 \end{aligned} \tag{5.7}$$

$$\begin{aligned}
 B_{3,6}: \quad & a = [a_3 + (a_3 * Size_{3,6} * n)], \forall n = 1 \text{ to } (N_{3,6} - 1) \\
 & b = b_6, \forall n = 1 \text{ to } (N_{3,6} - 1) \\
 & c = c_6, \forall n = 1 \text{ to } (N_{3,6} - 1)
 \end{aligned} \tag{5.8}$$

$$\begin{aligned}
 B_{3,7}: \quad & a = a_7, \forall n = 1 \text{ to } (N_{3,7} - 1); \\
 & b = [b_7 - (b_7 * Size_{3,7} * n)], \forall n = 1 \text{ to } (N_{3,7} - 1); \\
 & c = c_7, \forall n = 1 \text{ to } (N_{3,7} - 1);
 \end{aligned} \tag{5.9}$$

In order to generate nodes along branches $B_{3,2}$ and $B_{3,1}$, slopes of them need to be calculated. The slopes (m_1 & m_2) are calculated according to the following equations.

$$m_1 = \frac{(b_1 - a_1)}{(b_3 - a_3)} \tag{5.10}$$

$$m_2 = \frac{(b_2 - a_2)}{(b_3 - a_3)} \tag{5.11}$$

The inclinations (ϕ_1 & ϕ_2) are calculated using the equations stated as follows

$$\begin{aligned}
 \phi_1 &= Tan^{-1}(m_1) \\
 \phi_2 &= Tan^{-1}(m_2)
 \end{aligned} \tag{5.12}$$

The equations used to generate nodes along $B_{3,2}$ and $B_{3,1}$ are given below. An example for the pattern of nodes that are generated for the joint movement along the negative X-axis is shown in the Figure 5.8.

$$\begin{aligned}
 B_{3,2}: \quad & a = [a_3 + (a_3 * Size_{3,2} * \cos(\phi_2) * n)], \forall n = 1 \text{ to } (N_{3,2} - 1) \\
 & b = [b_3 + (b_3 * Size_{3,2} * \sin(\phi_2) * n)], \forall n = 1 \text{ to } (N_{3,2} - 1) \\
 & c = c_2, \forall n = 1 \text{ to } (N_{3,2} - 1)
 \end{aligned} \tag{5.13}$$

$$\begin{aligned}
 B_{3,1}: \quad & a = [a_3 - (a_3 * Size_{3,2} * \cos(\phi_1) * n)], \forall n = 1 \text{ to } (N_{3,1} - 1) \\
 & b = [b_3 + (b_3 * Size_{3,2} * \sin(\phi_1) * n)], \forall n = 1 \text{ to } (N_{3,1} - 1) \\
 & c = c_1, \forall n = 1 \text{ to } (N_{3,1} - 1)
 \end{aligned} \tag{5.14}$$

Step 6: Using the nodes generated in step 5, elements are generated along successive nodes. A meshed model for the joint movement along the positive X-direction is shown in the Figure 5.9.

Step 7: The database of all the branches associated with the joints at 3', 1, 2, 4 and their corresponding opposite locations are created at the final step.

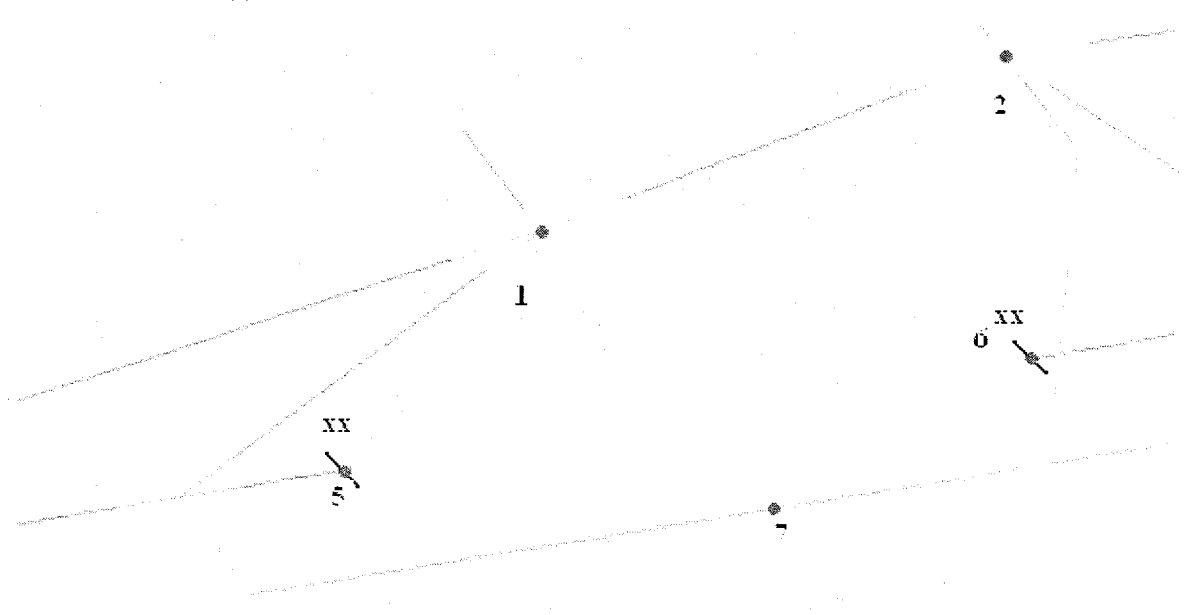


Figure 5.5: Details of Joint 3 before Modeling

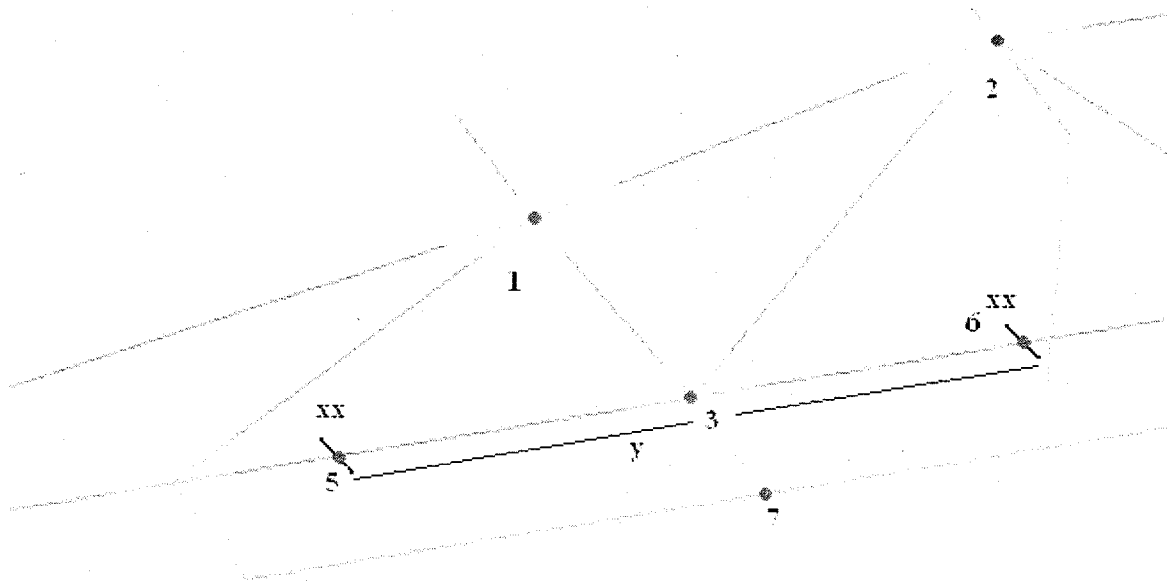


Figure 5.6: Range of Variable y

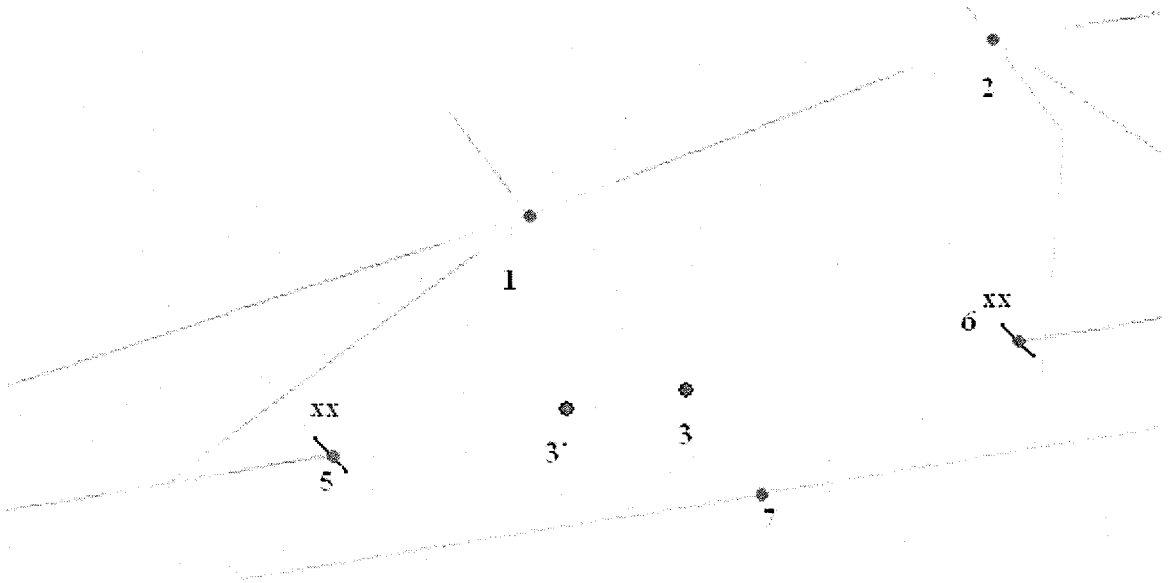


Figure 5.7: New Coordinates of Joint Location 3

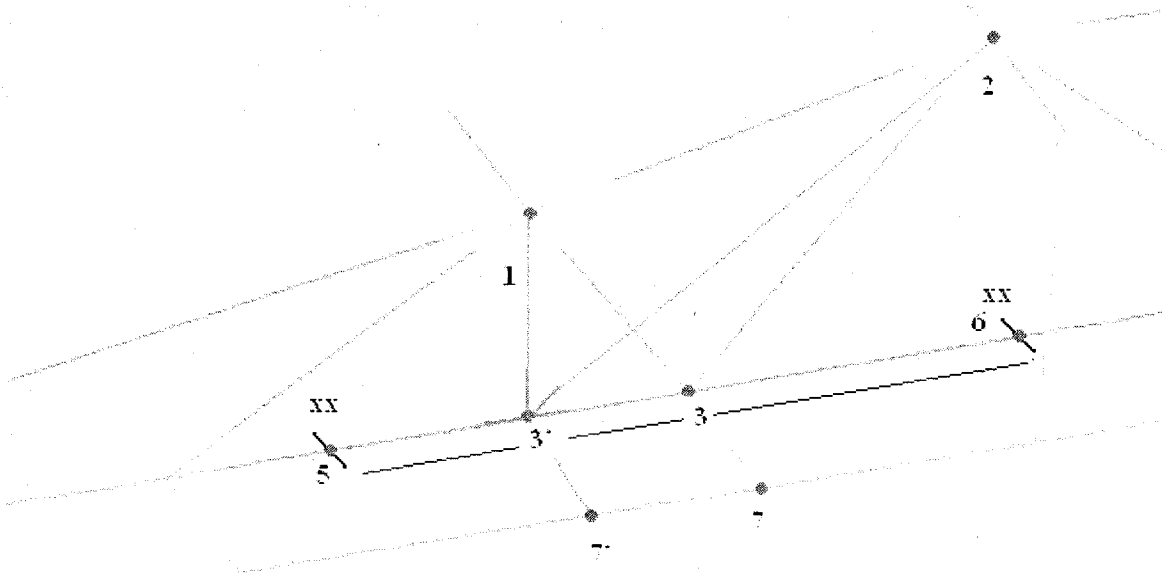


Figure 5.8: Case 2 Modeling Example for Left Movement of Joint

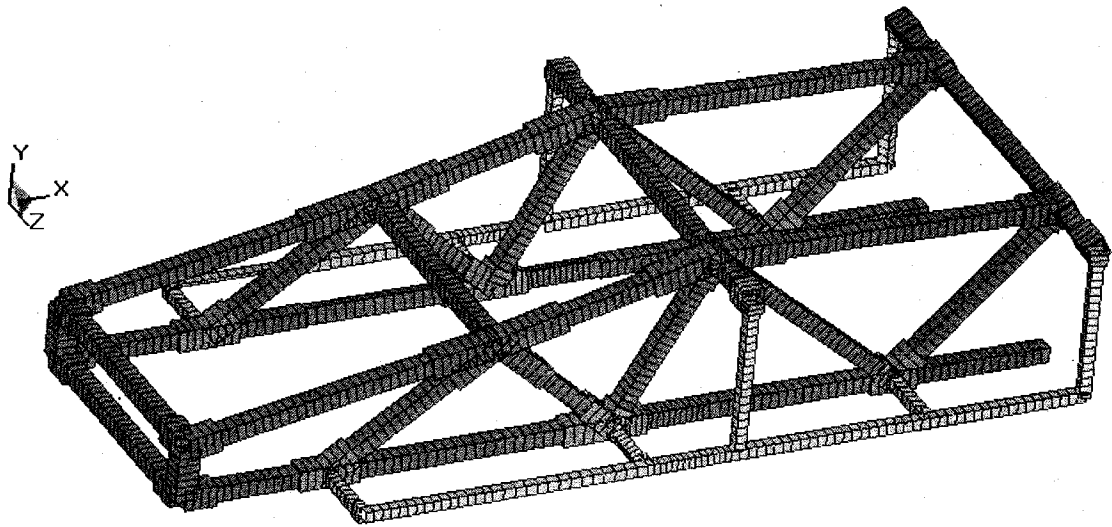


Figure 5.9: Mesh Details for the Joint Movement towards the Positive X-axis

5.2.4.2 Modeling part 2

Modeling part 2 is exactly similar to the one discussed in section 5.2.3. Using this procedure change in length of joint branches can be performed in conjunction with change in the location of joint 3.

5.3 Parameters for LS-DYNA Analysis

All contact surfaces, boundary conditions and other control cards described for Model 2 in Chapter 3 remain relevant during parametric study too.

5.4 Objective Function and Constraint Set

The mass of the eight joint locations is selected as the objective function to be minimized. The optimization problem can be stated as

$$f = \sum_{i=1}^n m_i \quad (5.15)$$

This objective function needs to be minimized by varying the design variables within the constraint set.

$$\frac{S_{i,j}}{2} \leq B_{i,j} \leq 2S_{i,j} \quad (5.16)$$

$$-n \leq y \leq n \quad (5.17)$$

where, m_i = Mass of all the joint branches at i^{th} joint location

$S_{i,j}$ = initial length of the joint branch

$B_{i,j}$ = Variable defining length of a joint branch at i^{th} joint location and j^{th} branch

y = distance movement of joint at 3

n = Limit for distance movement = 0.45 m

5.5 Optimization Technique

As we can see from the above description, it is evident that the present optimization problem is highly non-linear. Usually, successive quadratic programming is used to solve non-linear problems. A Successive quadratic programming iteratively solves a nonlinear programming problem by using a quadratic approximation to the optimization problem and a linear approximation to the constraint equations. As the series of quadratic programming problems are solved, these intermediate solutions generate a sequence of points that must remain in the feasible region or sufficiently close to this region to converge to the optimum. The logic used with this method is to search along the line between the new and previous point to maintain a feasible or near feasible solution.

A new method called Successive Heuristic Quadrature Approximation Technique, SHQA was developed by Trabia and Ceylan [28]. This method is successfully implemented to solve a nonlinear problem in stress corroded cylindrical containers. This method combines successive quadratic approximation with a controlled random search. If the problem is quadratic, then the quadratic approximation will help improve the search quickly. The controlled random search will be more effective if the problem is highly nonlinear as in this case.

The procedure for optimization process in this problem remains exactly the same as that of Model 1 described in Chapter 4. However, the AX-1 Model joint optimization problem is solved using Successive Heuristic Quadrature Approximation Technique, SHQA.

5.5.1 SHQA Algorithm:

The following steps describe the details of this algorithm for 2 two variable problem. The whole optimization problem is solved using the MATLAB environment. The detail of the whole procedure is given in the flow chart shown in Figure 6 and is described below.

- a) Input the upper bound and lower bound values of the variables.
- b) Calculate the range of each variable from the information in (a) and divide this range to create p equally spaced data points.
- c) Generate q number of points for all the design variables using the equation 5.7.

$$q = p^2 \quad (5.18)$$

- d) Calculate the objective function for all the points generated in (c)

- e) Obtain a minimal point of the surface obtained by fitting a quadratic polynomial to the data points generated in (c). Add this point to the q number of points already generated in (c).
- f) Evaluate the range of the function values for the $q+1$ points generated.
- g) Identify z number of points lying in the lower half of the function range value and generate the lower and upper bounds of the design variables within these z points.
- h) Generate additional random points $(q+1-z)$ within the range of the design variables from (g).
- i) Provide termination criteria.
- j) Go to step (a) again for the next iteration and repeat the process.

An example of the controlled random search process for a two variable problem is shown in the Figure 5.10. The process begins by generating q initial points within the domain described by A. the next domain, B is generated based on z points with lower lower function values. The complementary area i.e. $q-z$ is generated next. In this manner, controlled random search proceeds in coordination with successive quadratic approximation that uses current q points to find the minimum of the surface. This process is repeated till the termination criteria is met.

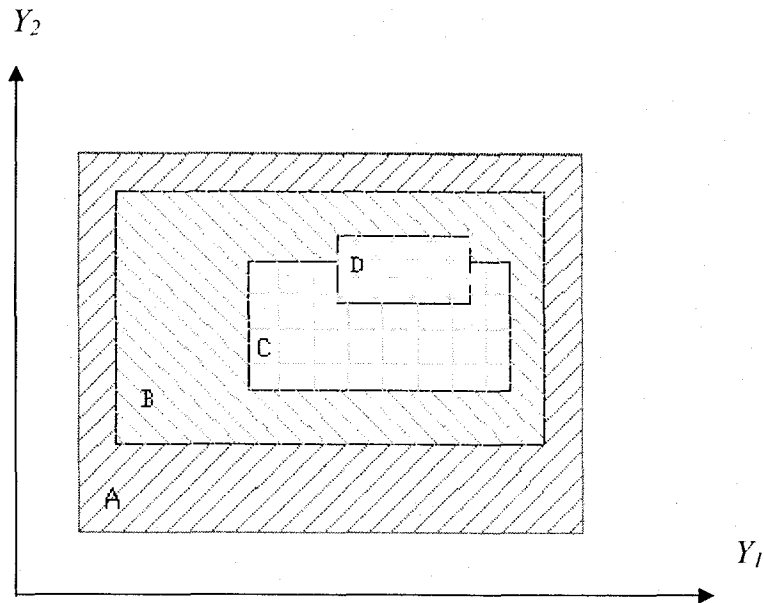


Figure 5.10: SHQA for a Two-Dimensional Problem

5.6 Results

5.6.1 Case 1

The optimization results for the case 1 are concerned with finding the optimized values of length of joint branches at the four joint locations as discussed before. The results for the side and front impact cases are summarized in Tables 5.1 and 5.2. Each color in the table indicates branches at a particular joint. For example, the five design variables in the green color indicate joint branches at the joint location 1. Since structural stiffness of the assembled structure under a given loading condition is evaluated as the magnitude of total displacements, maximum displacement in the space frame structure is evaluated for each function evaluation. The details of various parameters used in the Tables 5.1 and 5.2 are given below.

Jt – Joint Location Number

Br – Joint Branch Number

I.G. - Initial Guess

F.R.- Final Results

V- Maximum VonMises Stress in MPa

D- Maximum Displacement in m

f – Objective Function

Table 5.2 Side Impact Results

Design Variables (B_{ij})																				V (MPa)	D (m)	f (Kg)		
Jt#	1					2						3					4							
Br#	1	2	3	4	5	1	2	3	4	5	6	1	2	3	4	5	1	2	3	4	5			
I.G	2	5	4	4	5	5	4	2	4	5	2	4	2	4	4	3	4	2	4	3	4	398	0.0448	94
F.R	1	3	2	2	3	3	2	1	2	3	1	2	1	2	2	2	2	1	2	2	2	410	0.0454	68

Table 5.3 Front Impact Results

Design Variables (B_{ij})																				V (MPa)	D (m)	f (Kg)		
Jt#	1					2						3					4							
Br#	1	2	3	4	5	1	2	3	4	5	6	1	2	3	4	5	1	2	3	4	5			
I.G	2	5	4	4	5	5	4	2	4	5	2	4	2	4	4	3	4	2	4	3	4	398	0.0448	94
F.R	1	3	2	2	3	3	2	1	2	3	1	2	1	2	2	2	2	1	2	2	2	402	0.0458	68

We see that for both the side and front impact results, a 28 % reduction in mass is obtained. But this is accompanied by an increase in stress and maximum displacement. Figure 5.10 and Figure 5.11 shows plastic strain contours for the optimized final design values in case of side and front impacts respectively. We observe that maximum plastic strain value is 6.6 % in the front impact case and 7.8 % in the side impact case, both of which are less than the failure strain value of 13%. We can say that though the final optimal design gives an increase in stress values there is no failure in the material. Also, the maximum displacement value approximately lies close to the initial value. Hence the final design can be accepted due to the fact that this design gives enhanced reduction in mass with out causing any failure in the material of the space frame.

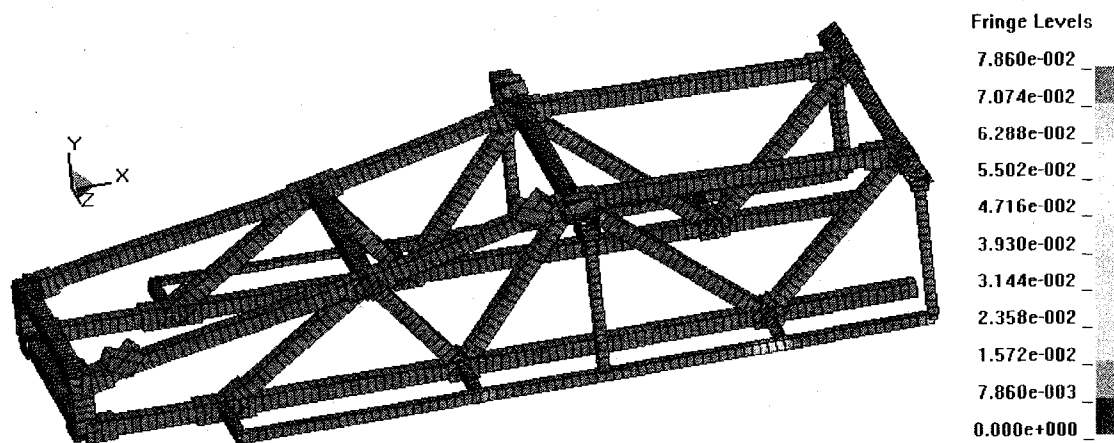


Figure 5.11: Maximum Plastic Strain Contours for Optimized Case at 25ms (Side Impact)

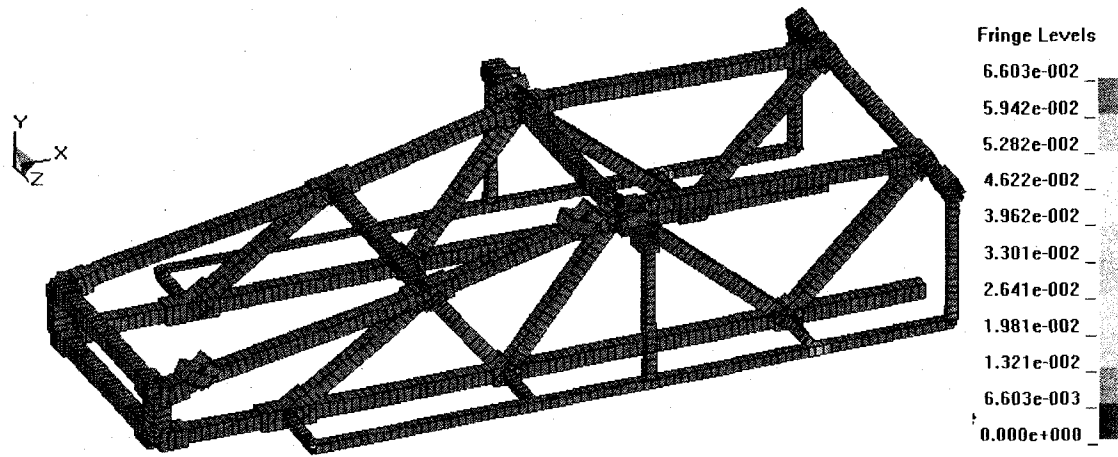


Figure 5.12: Maximum Plastic Strain Contours for Optimized Case at 25ms (Front Impact)

5.6.2 Case 2

The results from case 1 suggested that significant reduction in mass can be attained using the least possible length of the joint branches. However, this result does not evaluate whether the locations used for joints are optimum. Hence, an optimization is conducted by adding the variable y in this case. The final results obtained are shown in the Table 5.4. It can be seen that the joint location is shifted 0.35 m towards the front portion of the frame. Results indicate that there is a decrease in maximum stress and displacement in the optimized case when compared to the initial guess case. However, the decrease in the objective function is only 15 % which is considerably less than 28 % obtained in case 1.

Table 5.4 Side Impact Results for Case 2

		Design Variables ($B_{i,j}$)																				V (MPa)	D (m)	f (Kg)	
Jt#		1					2						3					4							
Br#		1	2	3	4	5	1	2	3	4	5	6	1	2	3	4	5	1	2	3	4	5	y=-0.35		
I.G		2	5	4	4	5	5	4	2	4	5	2	4	2	4	4	3	4	2	4	3	4	398	0.0449	94
F.R		1	3	2	2	3	3	2	1	2	3	1	2	1	2	2	2	2	1	2	2	2	395	0.0417	80

5.6.3 Single Variable Optimization

In this case, the only variable is y i.e. movement of joint 3. The lengths of the joint branches are kept at a constant value i.e. these correspond to the optimized values obtained in case 1. In addition to the constraint described in equation 5.17, another constraint is imposed which is stated as follows

$$s_{\max} \leq (s_f + s_y) / 2 \tag{5.19}$$

where s_{\max} = maximum von Mises stress; s_f = failure stress; s_y = yield stress

Optimization results are shown in Table 5.5 suggest that moving the joint location towards the negative x direction i.e. front portion of the frame gives an increase in the maximum displacement while decreasing the maximum stress value. And moving the joint location towards the positive x -direction i.e. towards the back portion of the space frame suggest that a decrease in maximum displacement can be obtained while contributing to the increase in the stress values. The zero value of the y variable indicates no movement of the joint location. These results are the same as seen from the results in Table 5.4. The small variation in the value of f is due to the fact that moving the joint

location varies the length of the branches associated with it. This variation contributes to the change in mass. Multiple conclusions can be drawn from these results.

- If the final objective of the design is to decrease mass with minimum possible increase in stress it is advisable to move the joint location towards front portion of the space frame.
- If the objective is to have a more stiff structure with little increase in stress value, it is recommended to move the joint location towards the back portion of the space frame.
- If a significantly more stiff structure is desired with out concentrating on increase in the stress values it is advised to keep the joint location at the same position with out moving it.

Table 5.5 Results for Movement of Joint at 3

y (in m)	V	D	f
-0.350	398	0.054	68.0
-0.260	398	0.053	67.5
-0.250	403	0.052	67.4
-0.150	399	0.051	67.0
-0.084	400	0.051	66.9
-0.061	400	0.051	66.9
-0.050	400	0.051	66.9
0.033	401	0.050	66.9
0.050	402	0.050	66.9
0.150	403	0.049	67.0
0.152	403	0.049	67.0
0.154	403	0.049	67.0
0.250	405	0.048	67.3
0.255	405	0.048	67.3
0.301	407	0.048	67.5
0	410	0.045	68.0

CHAPTER 6

CONCLUSION

To get a coherent picture of the entire work, a brief summary is provided in this chapter. The objective of this thesis is stated as follows

- Create simplified finite element models of the military vehicles to study shock transmission due to impact and blast loads.
- Study the effect of joint design by creating parametric finite element models of the military vehicles.
- Conduct optimization studies to evaluate effective joint design parameters which can mitigate shock transmission to a considerable extent.

6.1 Results for Model 1

Model 1 (APC M113 A2) is taken as the main model for studying the shock transmission due to a mine blast load. The acceleration results at the critical locations in the vehicle without a joint at the bottom panel are shown in the Figure 6.1, Figure 6.2 and Figure 6.3. Table 5.1 shows the peak and the average values of the acceleration curves at the three critical locations. To reduce the accelerations at these locations a joint at the bottom panel is proposed. The initial guess and the final design parameters for the model with joint are shown in Table 6.2. The average and maximum accelerations at the critical

locations for the final design is shown in Table 6.3. Comparing the results for the vehicle, we can say that significant reduction in accelerations are obtained by using a joint at the bottom panel. The acceleration results at the critical locations in the vehicle with a joint at the bottom panel are shown in the Figure 6.4, Figure 6.5 and Figure 6.6.

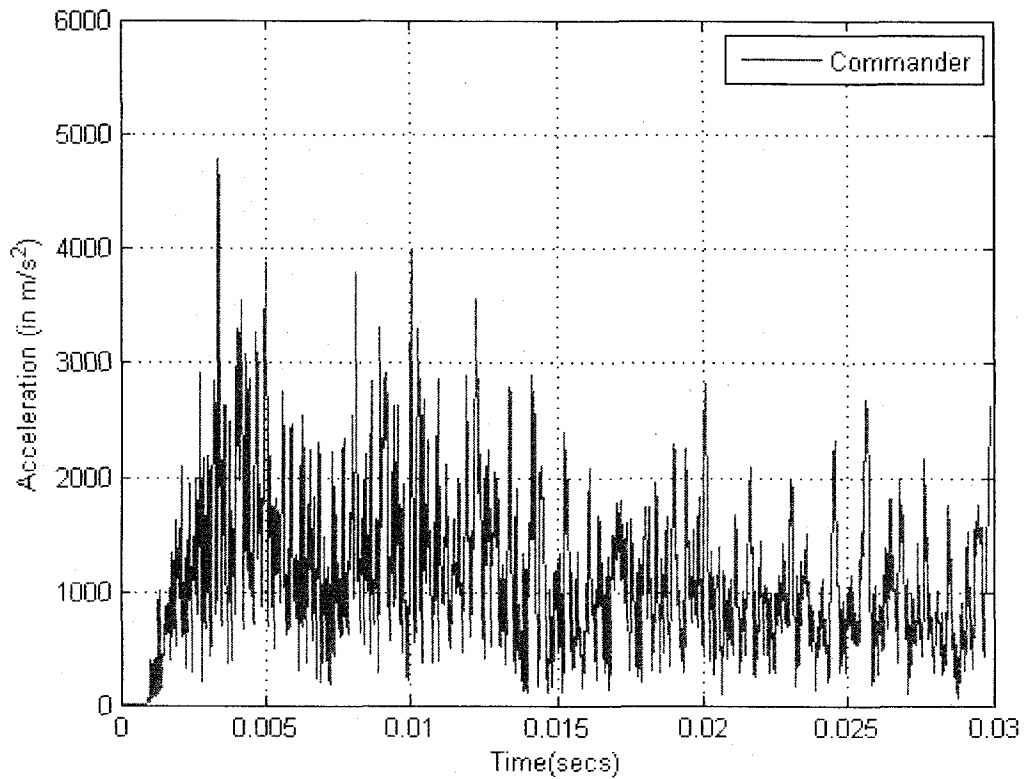


Figure 6.1 Acceleration Curves for Commander Location (No Joint)

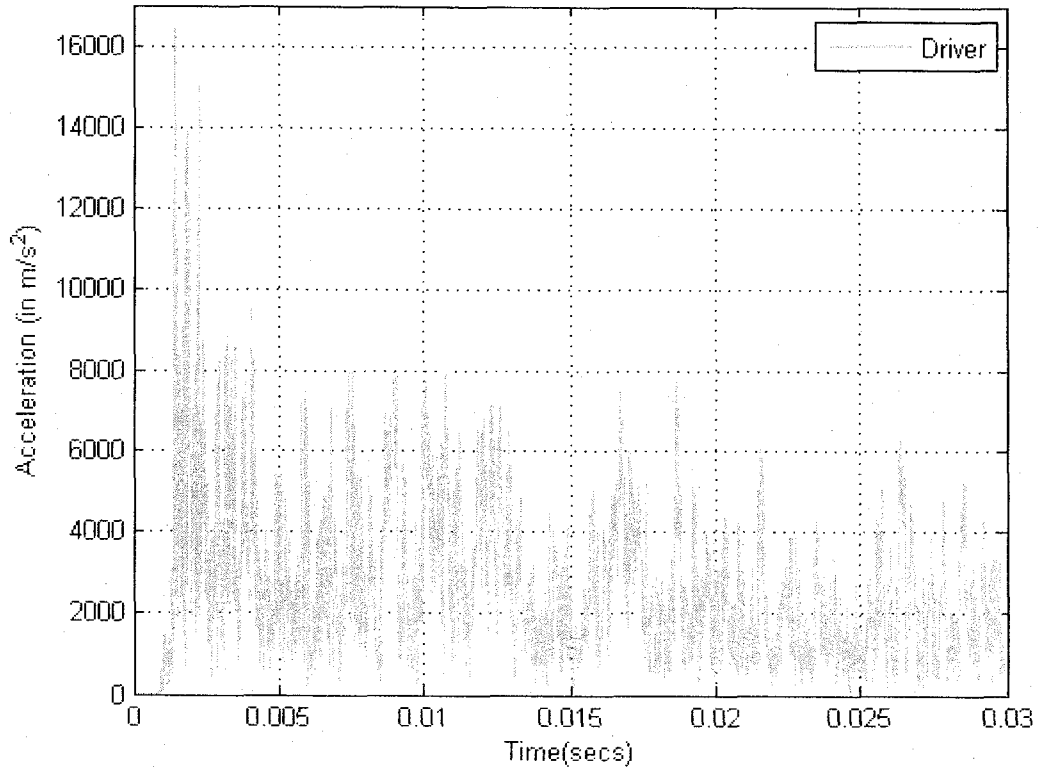


Figure 6.2 Acceleration Curves for Driver Location (No Joint)

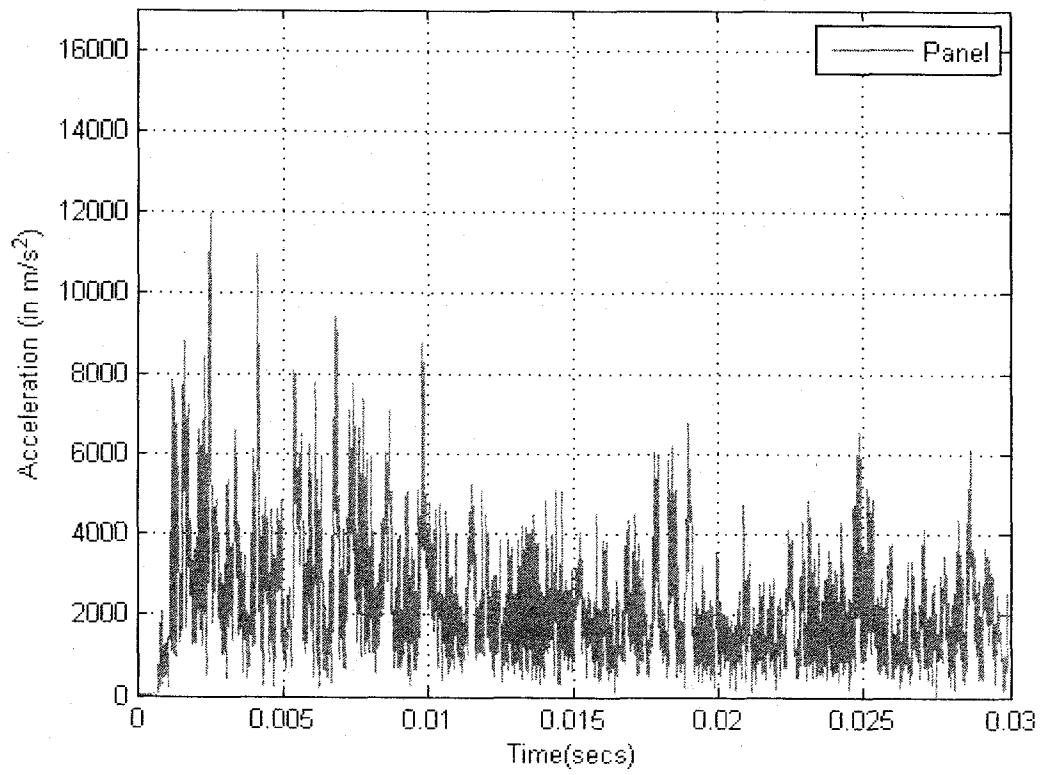


Figure 6.3 Acceleration Curves for Panel Location (No Joint)

Table 6.1: Acceleration results for the no-joint vehicle

Maximum acceleration (m/s^2)	commander	4789
	driver	16480
	instrumentation panel	11965
Average acceleration (m/s^2)	commander	1148
	driver	2650
	instrumentation panel	1149
Objective function value f	1649	

Table 6.2: Initial guess and Final Design Parameters

	t_3 (m)	t_4 (m)	L_3 (m)	L_4 (m)	f
Initial Guess	0.0080	0.0080	0.1220	0.1220	1392
Final	0.0103	0.0098	0.2292	0.2412	1182

Table 6.3: Optimized acceleration results for Final Design

Maximum acceleration (m/s^2)	commander	3076
	driver	16102
	instrumentation panel	9409
Average acceleration (m/s^2)	commander	773
	driver	2000
	instrumentation panel	774

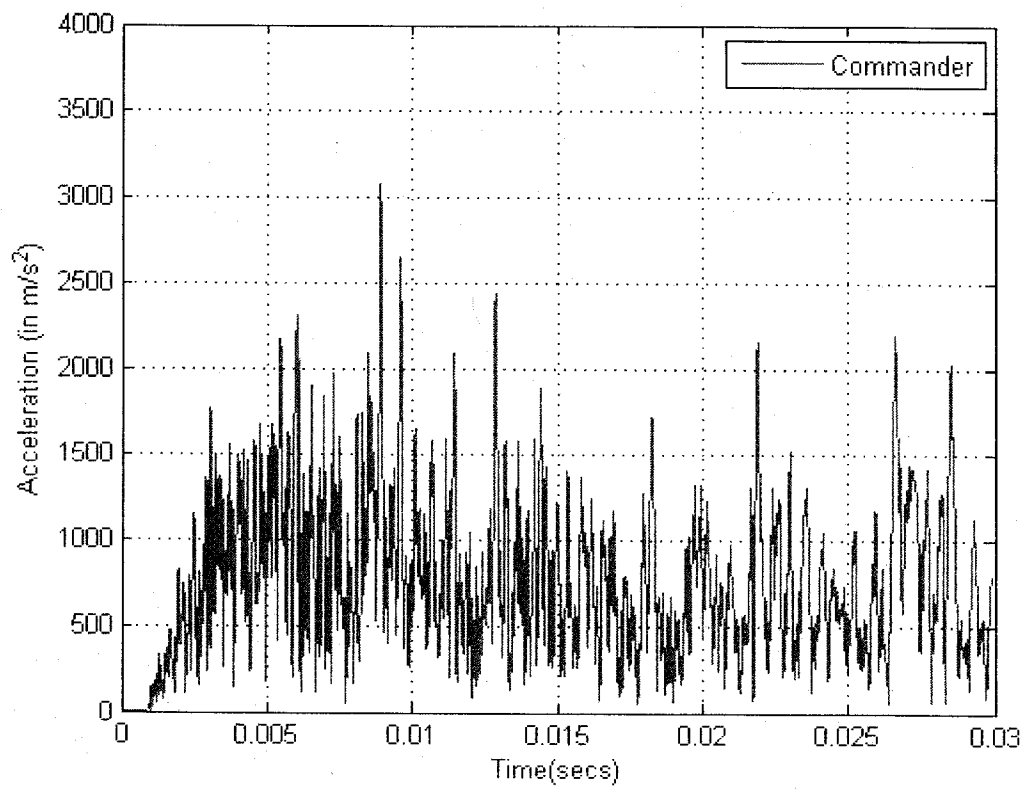


Figure 6.4 Acceleration Curves of Commander Location for Results of Case #1 (with Joint)

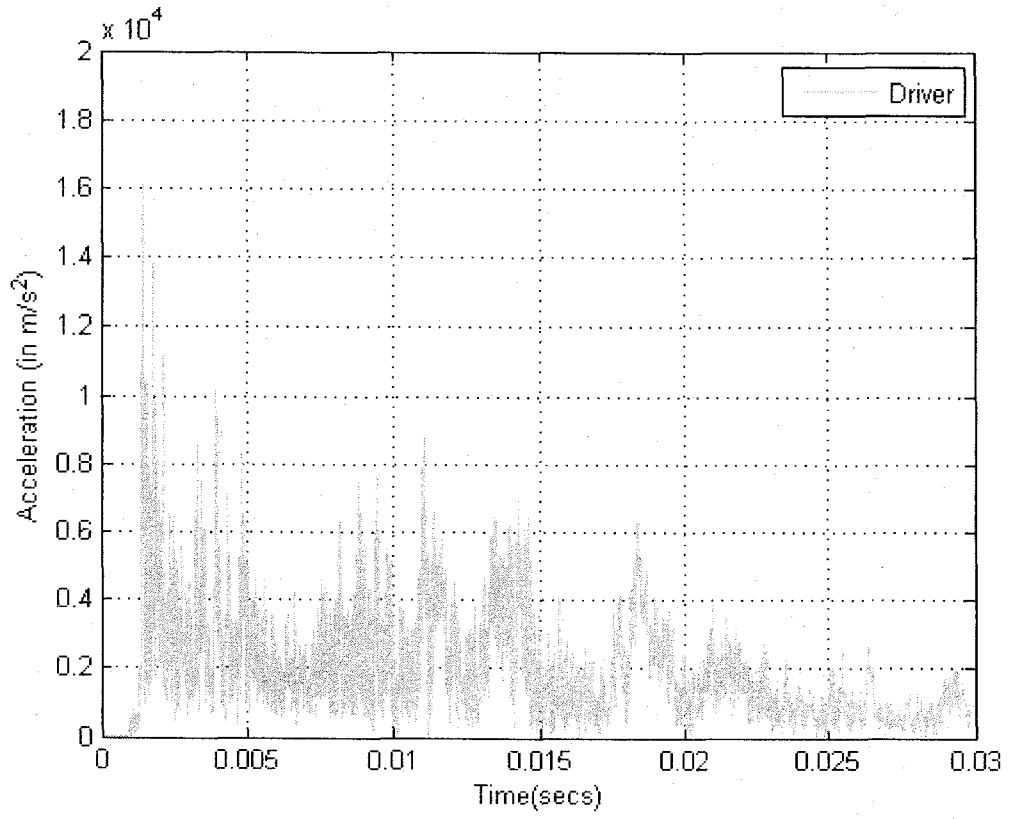


Figure 6.5 Acceleration Curves of Driver Location for Results of Case #1 (with Joint)

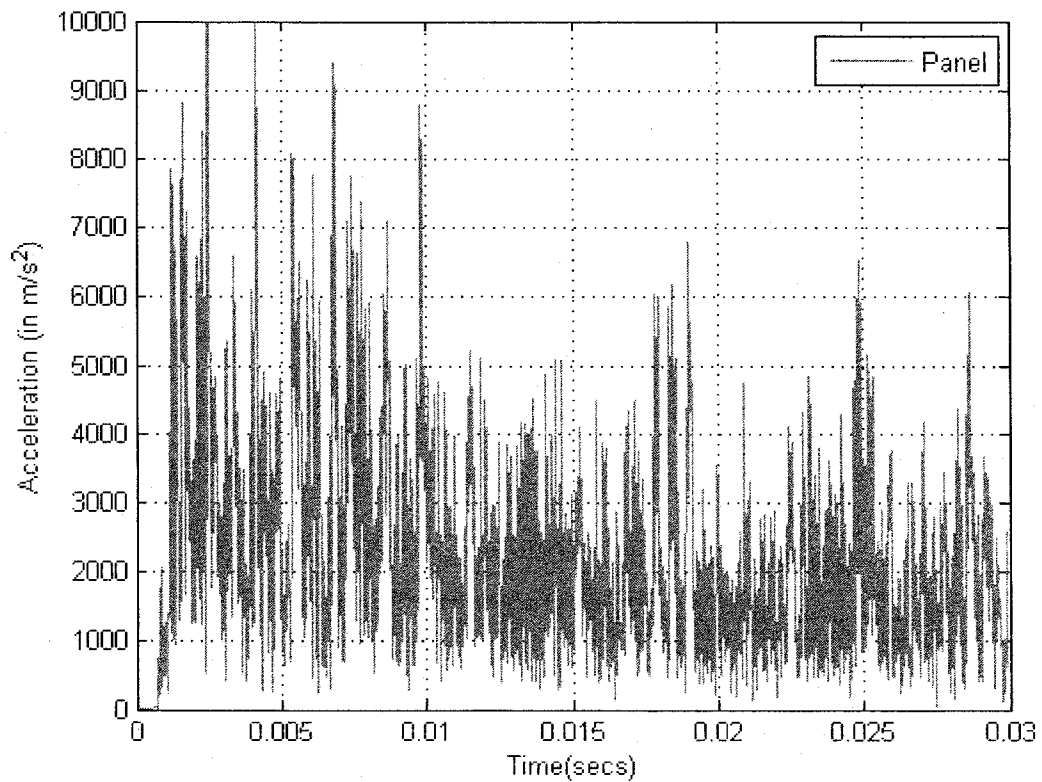


Figure 6.6 Acceleration Curves of Panel Location for Results of Case #1 (with Joint)

6.2 Results for Model 2

Model 2 (IS-ATD) is taken as the main model for studying the shock transmission due to a projectile impact. The optimization results for this model are concerned with finding the optimized values of length of joint branches at the four joint locations as discussed in section 5.7. The results for the initial guess and final results in terms of number of elements for the joints are shown in Table 6.4 and Table 6.5. Table 6.4 gives details for the side impact case while Table 6.5 provides results for front impact case. As can be observed from these results 28% reduction in mass is achieved without causing any failure in the material. The details of various parameters used in the Tables 5.1 and 5.2 are given below.

Jt – Joint Location Number

Br – Joint Branch Number

I.G. - Initial Guess

F.R.- Final Results

V- Maximum VonMises Stress in MPa

D- Maximum Displacement in m

f – Objective Function

Table 6.4 Side Impact Results

Design Variables ($B_{i,j}$)																				V (MPa)	D (m)	f (Kg)		
Jt#	1					2						3					4							
Br#	1	2	3	4	5	1	2	3	4	5	6	1	2	3	4	5	1	2	3	4	5			
I.G	2	5	4	4	5	5	4	2	4	5	2	4	2	4	4	3	4	2	4	3	4	398	0.0448	94
F.R	1	3	2	2	3	3	2	1	2	3	1	2	1	2	2	2	2	1	2	2	2	410	0.0454	68

Table 6.5 Front Impact Results

Design Variables ($B_{i,j}$)																				V (MPa)	D (m)	f (Kg)		
Jt#	1					2						3					4							
Br#	1	2	3	4	5	1	2	3	4	5	6	1	2	3	4	5	1	2	3	4	5			
I.G	2	5	4	4	5	5	4	2	4	5	2	4	2	4	4	3	4	2	4	3	4	398	0.0448	94
F.R	1	3	2	2	3	3	2	1	2	3	1	2	1	2	2	2	2	1	2	2	2	402	0.0458	68

6.3 Conclusions

6.3.1 Model 1

- Use of a suitable designed L-shaped joint at the bottom panel of a military vehicle helps in significant reduction in the accelerations at critical locations due to a mine blast.
- Parametric finite element modeling, meshing and dynamic analysis of the vehicle-joint structure and joint design optimization is carried out with the help of commercial FEA codes and MATLAB.
- Optimization results show that the objective function value is reduced considerably by reducing the thickness of the joint and extending it.

6.3.2 Model 2

- Significant reduction in mass is achieved by properly designing joints of a vehicle space frame.
- An optimal stiffness of the structure is achieved which helps in minimizing the mass without greatly increasing the stress values in the structure subjected to impact loads at various locations.

- Parametric finite element modeling, meshing and dynamic analysis of the space frame structure and its joint design optimization can be carried out with the help of commercial FEA codes and MATLAB.

6.4 Scope for Future work

6.4.1 Model 1

- Experimental validation needs to be conducted for the results obtained in this model.
- Study should be extended to a joint design using bolts to get a more realistic evaluation.
- Study should be conducted by changing blast load location to properly analyze the joint capabilities,
- Study should be extended for higher blast loads to analyze the plastic deformation capabilities of the joint in mitigating shock propagation.
- Present study is conducted using a simplified armored vehicle model; explicitly modeling all the remaining components and their interactions can provide with more realistic results.
- The robustness of the joint needs to be tested for other types of loads, such as projectile impacts.

6.4.2 Model 2

- Experimental validation needs to be conducted for the results obtained in this model.

- This study is conducted only on the space frame of the armored vehicle and its armor; explicitly modeling all the remaining components and their interactions can provide with more realistic results.
- In the optimization study, only one geometric parameter is considered for the joints; other cross-sectional parameters should be added to the optimization problem to get more significant results.
- Study should be extended for higher impact loads to analyze the effective stiffness value for the entire structure.
- The robustness of the final design needs to be tested for other types of loads, such as blast loads.

REFERENCES

1. Gupta A. D., Santiago A.M., and Meyer C., "Comparison of computational and experimental modal analysis of an armored vehicle hull with multiple access Openings", *Computers and Structures*, Vol. 56, No.2/3, pp. 411-414, 1995.
2. Gupta, A. D., Santiago, J. M., and Wisniewski, H. L., "Shock damage to sensitive components in an armored vehicle", *Computers in Engineering, Proceedings of the International Computers in Engineering Conference and Exhibit*, Vol. 2, pp. 153-161, 1992.
3. Joosef Martti L, "Concrete structures subjected to fragment impacts: Dynamic behavior and material modeling", *Chalmers tekniska Hogskola (Sweden), Dissertation*, 2004.
4. Micheal Neff, *A visual Model for Blast Waves and Fracture*, Masters Thesis, University of Toronto, 1998.
5. William E Baker, *Explosion in Air*, University of Texas Press, Austin, 1973.
6. Randers-Pehrson, Bannister "Airblast Loading Model for DYNA2D and DYNA 3D", ARL-TR-1310, 1997.
7. K. Mahmadi, N. Aquelet, M. Souli, *Emerging Technology in Fluids, Structures and Fluid- Structure Interactions*, PVP-Vol. 460, 2003.
8. Wang, J, "Simulation of Landmine Explosion Using LS-DYNA3D Software: Benchmark Work of Simulation of Explosion in Soil and Air (DSTO-TR-1168)",

9. Fishermans Bend, Victoria, Australia: DSTO Aeronautical and Maritime Research Laboratory, 2001.
10. Andre Haufe et al, "Advanced Airbags simulation using Fluid-Structure-Interaction and the Eulerian Method in LS-DYNA", LS-DYNA Anwenderforum, Bamberg 2004.
11. Micheal D. Letherwood, David D. Gunter, "Ground vehicle modeling and simulation of military vehicles using high performance computing", Parallel Computing, 27 pp 109-140, 2001.
12. Gupta, A. D., "Evaluation of a fully assembled armored vehicle hull – turret model using computational and experimental modal analyses", Computers & Structures 72, pp 177-183, 1999.
13. Unruh. James F, "Evaluation of shock response in combat vehicles", 56th Symposium on Shock and Vibration, Monterey, CA, USA.
14. Norman, R.M., "Deformation in flat plates exposed to HE Mine Blast." AMSAA-TM-74, U.S. Army Material Systems Analysis Agency, Aberdeen Proving Ground, MD, 1970.
15. Hoskin, N.E., Allan, J.W., Bailey, W.A., Lethaby, J.W., and Skidmore, I., "The motion of plates and cylinders driven at tangential incidence." Fourth International Symposium on detonation, ACR-126, Office of Naval Research, Pasadena, CA, 1965.
16. Gupta, A.D., "Modeling and analysis of a blast deflector for a tactical vehicle due to detonation of a mine buried in dry vs. saturated sand", Technical Report, U.S. Army Research Laboratory, Aberdeen Proving Ground, MD 21005-5066.

17. Laine, L., Ranestad, Ø., Sandvik, A., and Snekkkevik, A., “Numerical Simulation of anti-tank mine detonations”, 12th APS Tropical group Conference on Shock Compression of Condensed Matter, Atlanta, USA, 2001.
18. Lafrance, L.P., “ Mine blast protection system for army vehicles”, Proceedings of the 1998 ASME/JSME Joint Pressure Vessels and Piping Conference, San Diego, CA, USA, Jul 26-30 1998.
19. Gaul L, and J.Lenz, “Nonlinear Dynamics of Structures Assembled by Bolted Joints”, Acta Mechanica 125, 169-181, 1997.
20. Nobutoshi Masuda, Takeo Nishiwaki, Masaru Minagawa, “Nonlinear dynamic analysis of frame structures”, Computers & Structures 27, pp 103-110, 1987.
21. Karpurapu, R., Yogendrakumar M., “A kinematic model for dynamic analysis of space frames”, Computers & Structures 47, pp. 945-955, 1993.
22. Goman Wai, Sui-Lai Chan, “An accurate and efficient method for large deflection inelastic analysis of frames with semi rigid connections”, J. Construct. Steel Research 26, pp 171-191, 1993.
23. Siu Lai Chan, Large deflection dynamic analysis of space frames, Computers & Structures 58, Vol. No.2, 381-386, 1996.
24. Naesung Lyu, Kazuhiro Saitou, “ Decomposition-based assembly synthesis of space frame structures using joint library”, Proceedings of DETC’04, ASME 2004 Design Engineering Technical Conferences and Computers and Information in Engineering Conference, September 28- Oct 2, Salt Lake City, USA, 2004.

25. Azhari Sastranegara, Tadaharu Adachi, Akihiko Yamaji, "Improvement of energy absorption of impacted column due to transverse impact", *International Journal of Impact Engineering* 32, 483-496, 2005.
26. Sergeyev O., Mroz Z., "Sensitivity analysis and optimal design of 3D frame structures for stress and frequency constraints", *Computers & Structures* 75, 167-185, 2000.
27. Qui X., Deshpande V. S., Fleck N.A., "Finite element analysis of the dynamic response of clamped sandwich beams subject to shock loading", *European Journal of Computational Mechanics* 22, 801-814, 2003.
28. Trabia, M., and Liu, X., "A fuzzy adaptive simplex search optimization algorithm", *Journal of Mechanical Design*, Vol. 123, pp. 216-225, 2000.
29. Trabia, M., and Zekai, C., "Optimization of the Closure-Weld Region of Cylindrical Containers for Long-Term Corrosion Resistance using the Successive Heuristic Quadratic Approximation Technique", *Journal of Mechanical Design*, Vol. 125, 2003.
30. Ralph. W. Pike, *Optimization for engineering systems* (on-line course material), Professor of Chemical Engineering and Systems Science, Louisiana State University, 2001.
31. Naraparaju, J, "Joint Design for Shock Mitigation". Master's Thesis, Department of Mechanical Engineering, University of Nevada, Las Vegas, 2005.
32. ARL Conference Calls, Power Point Presentation, 02-02-2005
33. LS-DYNA 970 Keyword Users Manual, Livermore Software Technology Corporation.

34. Micheal J Mullin, " Finite Element Modeling of Energy Absorbing Materials in Blast Loaded Structures", MS Thesis, University of Nevada, Las Vegas, 2004.
34. <http://www.inetres.com/gp/military/cv/effects.html>
35. Federation of American Scientists, Military Analysis Network, US Land Warfare Systems, M113 <http://www.fas.org/man/dod-101/sys/land/m113.htm>
36. [www.globalsecurity.org/military/ library/budget/fy2006/army-peds/0603005A.pdf](http://www.globalsecurity.org/military/library/budget/fy2006/army-peds/0603005A.pdf)

VITA
Graduate College
University of Nevada, Las Vegas

Umakanth Sakaray

Local Address:
935 E Cottage Grove Ave, Apt#35
Las Vegas NV 89119

Permanent Address:
H.No: 8-103, Gowthamnagar, Dilsukhnagar,
Hyderabad, Andhra Pradesh, INDIA 500060

Degrees:
Bachelor of Engineering, Mechanical Engineering, 2004
Osmania University,
Andhra Pradesh, INDIA

Affiliations:
Member of Phi Kappa Phi, National Honor Society
Member of Tau Beta Pi Engineering Honor Society (TBP)
Member of American Society of Mechanical Engineers (ASME)

Publications:
Umakanth Sakaray, "Joint Design for the Bottom Panel of the Parachute Dropped Light Armored Vehicle", AIAA 2006 Student Conference, Irvine, California, USA, April 6-8.
David Lee, Umakanth Sakaray, "Energy Absorbing Sandwich Structures under Blast Loading", AIAA 2005 Student Conference, San Louis Obispo, CA, April 2005.

Thesis Title: Design and Optimization of Joints to Mitigate Shock in Military Vehicles under Blast and Impact Loading.

Thesis Examination Committee:
Chairperson, Dr. Mohamed B Trabia, Ph. D.
Chairperson, Dr. Brendan J. O'Toole, Ph. D.
Committee Member, Dr. Ajit K. Roy, Ph. D.
Committee Member, Dr. William Wells, Ph. D.
Graduate College Faculty Representative, Dr. Satish Bhatnagar, Ph. D.